

**Detection and measurement of land deformations
caused by seismic events
using InSAR, Sub-pixel correlation, and Inversion
techniques**

Mohammad Ali Goudarzi

January 2010

Course Title: Geo-Information Science and Earth Observation for Environmental modelling and Management

Level: Master of Science (MSc)

Course Duration: April 2008 – January 2010

Consortium partners: University of Southampton (UK)
Lund University (Sweden)
University of Warsaw (Poland)
International Institute for Geo-Information Science and Earth Observation (ITC) (The Netherlands)

GEM- Thesis number: 2010 – 02

**Detection and measurement of land deformations
caused by seismic events
using InSAR, Sub-pixel Correlation and Inversion techniques**

by:
Mohammad Ali Goudarzi

This thesis submitted to the International Institute for Geo-Information Science and Earth Observation in partial fulfilment of the requirement for the degree of Master of Science in Geo-Information Science and Earth Observation for Environmental modelling and Management.

Thesis Assessment Board:

Chairman: Prof. Dr. Freek van der Meer
External Examiner: Prof. Terence P. Dawson
Primary Supervisor: Dr. Tsehaie Woldai
Secondary Supervisor: Dr. Valentyn Tolpekin



International Institute for Geo-Information Science and Earth Observation (ITC)
Enschede, The Netherlands

Disclaimer

This document describes work undertaken as part of a program of study at the International Institute for Geo-Information Science and Earth Observation. All views and opinions expressed therein remain the sole responsibility of the author, and do not necessarily represent those of the institute.



بِسْمِ اللَّهِ الرَّحْمَنِ الرَّحِيمِ

Table of contents

List of figures.....	I
List of tables.....	IV
Abstract.....	VI
Abstract (Persian).....	VII
Acknowledgements.....	IX
Abbreviations.....	XI
1 Introduction.....	1
1.1 Research problems statement.....	2
1.2 Research objectives.....	2
1.2.1 General objective.....	2
1.2.2 Specific objectives.....	2
1.3 Research questions.....	3
1.4 Research hypotheses.....	3
2 Literature review and background.....	5
2.1 SAR interferometry.....	6
2.1.1 Applications of InSAR in earth sciences.....	6
2.1.2 Interferometry equations.....	7
2.1.3 Characteristics of interferometric phase.....	10
2.1.4 SAR satellites.....	11
2.1.4.1 ERS.....	11
2.1.4.2 ERS-2 gyroscope problem.....	12
2.1.4.3 Effect of the gyroscope failure on InSAR performance.....	12
2.1.4.4 ENVISAT.....	13
2.1.4.5 ALOS.....	14
2.1.5 SAR images.....	15
2.1.5.1 The SAR amplitude image.....	15
2.1.5.2 The SAR phase image.....	15
2.1.5.3 Speckle.....	16
2.2 Sub-pixel correlation technique.....	16
2.2.1 Applications of SCT in earth sciences.....	17
2.2.2 Comparing SCT with InSAR.....	17
2.2.3 SCT algorithms.....	18
2.3 Inversion problem.....	19
2.3.1 Neighbourhood algorithm.....	20
2.3.2 Linear least square inversion.....	21
3 The study area.....	23
3.1 Geological and tectonic settings.....	24
3.1.1 Geodynamic evolution.....	24
3.1.2 Geological settings.....	25
3.1.3 Tectonic setting.....	27
3.2 Seismological aspects.....	28
3.2.1 The main shock.....	28
3.2.2 Seismic sequence.....	28
3.2.3 Recent and historical seismicity.....	29
4 Methods and materials.....	33
4.1 InSAR.....	33
4.1.1 Radar image data sets for interferometry.....	34
4.1.1.1 ERS-1/2.....	34
4.1.1.2 ENVISAT.....	35
4.1.1.3 ALOS.....	36

4.1.2	Auxiliary data sets.....	36
4.1.2.1	DEM.....	36
4.1.2.2	Orbital parameters.....	39
4.1.2.3	Instrumental files.....	39
4.1.2.4	Geological map.....	39
4.1.2.5	Faults map.....	40
4.1.2.6	NDVI map.....	40
4.1.2.7	Slope and aspect maps.....	41
4.1.3	InSAR software.....	42
4.1.3.1	Unwrapping software.....	44
4.2	SCT.....	45
4.2.1	SCT using SAR image data sets.....	45
4.2.1.1	Radar image data sets for SCT.....	45
4.2.1.2	Sub-pixel correlator software for SAR data sets.....	46
4.2.2	SCT using optical image data sets.....	46
4.2.2.1	Optical image data sets.....	46
4.2.2.1.1	ASTER.....	47
4.2.2.2	Sub-pixel correlator software for optical image data sets.....	48
4.3	Inversion problem.....	49
4.3.1	NA algorithm.....	50
4.3.2	Linear least square inversion.....	51
5	Results and interpretation.....	53
5.1	SAR interferometry.....	53
5.1.1	ENVISAT ASAR data set.....	53
5.1.2	ALOS PALSAR data set.....	60
5.2	Sub-pixel correlation technique.....	66
5.2.1	ENVISAT ASAR data set.....	66
5.2.2	ASTER data set.....	70
5.3	Inversion problem.....	74
5.3.1	NA algorithm.....	74
5.3.2	Linear least square inversion.....	80
6	Discussion.....	85
6.1	SAR interferometry.....	85
6.2	Sub-pixel correlation technique.....	86
6.3	Inversion problem.....	87
7	Conclusions and recommendations.....	91
7.1	Overall results.....	91
7.1.1	Results from SAR interferometry.....	92
7.1.2	Results from sub-pixel correlation technique.....	92
7.1.3	Results from Inversion problem.....	92
7.2	Answer to research questions.....	93
7.3	Limitations.....	94
7.3.1	Limitations on InSAR technique and data sets.....	95
7.3.2	Limitations on SCT and data sets.....	95
7.3.3	Limitations on Inversion problem.....	95
7.4	Recommendations.....	96
7.4.1	Recommendations on InSAR.....	96
7.4.2	Recommendations on SCT.....	97
7.4.3	Recommendations on Inversion problem.....	97
7.5	Future directions.....	97
8	Appendices.....	99

8.1 Appendix A- Figures.....	99
8.2 Appendix B- Tables.....	113
8.3 Appendix C- Websites.....	117
9 References.....	119

List of figures

Figure 1: Interferometric geometry (Rosen et al., 1996).....	8
Figure 2: Configuration of the ERS-2 piloting modes and corresponding orbit dead-band evolution (Miranda et al., 2004).....	12
Figure 3: Emitted and backscattered sinusoidal signal.....	16
Figure 4: The study area.....	23
Figure 5: Geodynamic model for central Mediterranean (Devoti et al, 2008).....	25
Figure 6: South-west to north-east geological cross-section, passing the L'Aquila basin (geologic map of Italy at scale 1:50,000).....	27
Figure 7: Seismic history of L'Aquila area (DBMI04, 2009).....	30
Figure 8: Results of macro seismic survey conducted by the QUEST (QUEST, 2009).....	30
Figure 9: Overall methods and procedures.....	33
Figure 10: Comparison of DC frequency between two images of an ERS-2 inter- ferometric pair.....	35
Figure 11: Sketch map of the prepared ASTER GDEM.....	38
Figure 12: ENVISAT heading angle in ascending pass.....	41
Figure 13: ENVISAT heading angle in descending pass.....	41
Figure 14: ALOS heading angle in ascending pass.....	41
Figure 15: ALOS heading angle in descending pass.....	41
Figure 16: ROI_PAC work flow (modified from Fielding, 2008a).....	43
Figure 17: COSI-Corr work flow.....	49
Figure 18: ASAR interferogram for the ascending pair (09/04/15-09/03/11).....	54
Figure 19: ASAR interferogram for the descending pair (09/04/12-09/02/01).....	54
Figure 20: COSMO-SkyMed interferogram (09/02/19-09/04/09) modified from Salvi et al., 2009.....	55
Figure 21: coherence map of the ascending ASAR interferogram.....	56
Figure 22: coherence map of the descending ASAR interferogram.....	56
Figure 23: NDVI map.....	57
Figure 24: Slope map for ASAR.....	57
Figure 25: ASAR interferogram for the third pair(09/04/12-08/04/27).....	58
Figure 26: coherence map of the third ASAR interferogram (09/04/12-08/04/27)	58
Figure 27: Unwrapped ENVISAT ASAR ascending interferogram.....	59
Figure 28: Unwrapped ENVISAT ASAR descending interferogram.....	59
Figure 29: PALSAR interferogram for the first pair (09/05/21-08/07/03).....	61
Figure 30: PALSAR interferogram for the second pair (09/04/22-08/07/20).....	61
Figure 31: coherence map of the first ALOS PALSAR interferogram.....	62
Figure 32: coherence map of the second ALOS PALSAR interferogram.....	62
Figure 33: NDVI map.....	63
Figure 34: Slope map for PALSAR.....	63
Figure 35: Unwrapped interferogram of the first ALOS PALSAR pair.....	63
Figure 36: Unwrapped interferogram of the second ALOS PALSAR pair.....	63
Figure 37: Comparison between profiles from filtered and unfiltered unwrapped interferograms for the first ALOS PALSAR pair.....	65
Figure 38: Comparison between profiles from filtered and unfiltered unwrapped interferograms for the second ALOS PALSAR pair.....	65
Figure 39: Coseismic horizontal displacement of permanent GPS stations in L'A-	

quila (modified from Anzidei et al., 2009).....	67
Figure 40: Azimuth offset of the ENVISAT ASAR ascending pair.....	69
Figure 41: Range offset of the ENVISAT ASAR ascending pair.....	69
Figure 42: Azimuth offset of the ENVISAT ASAR descending pair.....	69
Figure 43: Range offset of the ENVISAT ASAR descending pair.....	69
Figure 44: Coherence map for the ascending pair.....	70
Figure 45: Coherence map for the descending pair.....	70
Figure 46: West-east offset of the first ASTER pair.....	72
Figure 47: South-north offset of the first ASTER pair.....	72
Figure 48: Displacement vectors of the first ASTER pair.....	72
Figure 49: SNR channel of the first ASTER pair.....	72
Figure 50: West- east offset of the second ASTER pair.....	73
Figure 51: South-north offset of the second ASTER pair.....	73
Figure 52: Displacement vectors of the second ASTER pair.....	73
Figure 53: SNR channel of the second ASTER pair.....	73
Figure 54: Observed and optimised-modelled interferograms for the ascending pair from the NA inversion.....	75
Figure 55: Observed and optimised-modelled interferograms for the descending pair from the NA inversion.....	75
Figure 56: Projection of satellite LOS on the ground surface (side view).....	77
Figure 57: Projection of satellite LOS on the ground surface (top view).....	77
Figure 58: Residual interferogram for the ascending model from NA inversion..	77
Figure 59: Residual interferogram for the descending model from NA inversion	77
Figure 60: Focal mechanisms and geomorphology of the Paganica fault and the surrounding area.....	79
Figure 61: Observed, optimised-modelled and residual interferograms for the as- cending pair from the LS inversion.....	81
Figure 62: Observed, optimised-modelled and residual interferograms for the des- cending pair from the LS inversion.....	81
Figure 63: Residual interferogram for the ascending model from LS inversion..	82
Figure 64: Residual interferogram for the descending model from LS inversion.	82
Figure 65: Distribution of dip slip along the fault plan resulted from the ascending pair.....	83
Figure 66: Distribution of dip slip along the fault plan resulted from the descend- ing pair.....	83
Figure 67: Distribution of dip slip projected on the horizontal plane.....	84
Figure 68: Azimuth offset from the ENVISAT ASAR ascending pair for Bam area	87
Figure 69: Azimuth offset from the ENVISAT ASAR descending pair for Bam area.....	87
Figure 70: The Onna graben.....	88
Figure 71: Geological-structural map of the central Apennines (Blumetti et al., 2009).....	99
Figure 72: Active faults of the L'Aquila area (INGV website).....	100
Figure 73: Seismic sequence in L'Aquila area (INGV website).....	100
Figure 74: Historical seismicity of the central Apennines near L'Aquila (Rovida et al., 2009).....	101
Figure 75: The NDVI map for the centre of Italy.....	101
Figure 76: Azimuth spectrum overlap for the ENVISAT ASAR ascending pair	

	(2009/04/15-2009/03/11).....	102
Figure 77:	Azimuth spectrum overlap for the ENVISAT ASAR descending pair (2009/04/12-2009/02/01).....	102
Figure 78:	Range and azimuth offsets versus range and azimuth samples for the ENVISAT ASAR ascending pair (2009/04/15-2009/03/11)....	103
Figure 79:	Range and azimuth offsets versus range and azimuth samples for the ENVISAT ASAR descending pair (2009/04/12-2009/02/01) .	103
Figure 80:	Displacement in the satellite LOS direction along profiles from EN- VISAT ASAR ascending pair.....	104
Figure 81:	Displacement in the satellite LOS direction along cross sections from ENVISAT ASAR ascending pair.....	104
Figure 82:	Displacement in the satellite LOS direction along profiles from EN- VISAT ASAR descending pair.....	105
Figure 83:	Displacement in the satellite LOS direction along cross sections from ENVISAT ASAR descending pair.....	105
Figure 84:	Azimuth spectrum overlap for the first ALOS PALSAR interferometric pair (2009/05/21-2008/07/03).....	106
Figure 85:	Azimuth spectrum overlap for the second ALOS PALSAR interfero- metric pair (2009/04/22-2008/07/20).....	106
Figure 86:	Range and azimuth offsets versus range and azimuth samples for the first ALOS PALSAR interferometric pair (2009/05/21- 2008/07/03).....	107
Figure 87:	Range and azimuth offsets versus range and azimuth samples for the second ALOS PALSAR interferometric pair (2009/04/22- 2008/07/20).....	107
Figure 88:	Displacement in the satellite LOS direction along profiles for the first ALOS PALSAR pair (2009/05/21-2008/07/03).....	108
Figure 89:	Displacement in the satellite LOS direction along cross sections for the first ALOS PALSAR pair (2009/05/21-2008/07/03).....	108
Figure 90:	Displacement in the satellite LOS direction along profiles for the second ALOS PALSAR pair (2009/04/22-2008/07/20).....	109
Figure 91:	Displacement in the satellite LOS direction along cross sections for the second ALOS PALSAR pair (2009/04/22-2008/07/20).....	109
Figure 92:	Histograms of the displacements in azimuth direction for the EN- VISAT ASAR pairs.....	110
Figure 93:	Histograms of the displacements in range direction for the ENVISAT ASAR pairs.....	110
Figure 94:	Histogram of the west-east offset for the second ASTER pair.....	111
Figure 95:	Histogram of the south-north offset for the second ASTER pair.....	111

List of tables

Table 1: ERS-2 and AMI specifications (ERS, 2009).....	11
Table 2: ENVISAT and ASAR specifications (ENVISAT, 2009).....	13
Table 3: Sensitivity vector components for ENVISAT and ERS-1/2 in ascending and descending passes.....	14
Table 4: ALOS and PALSAR specifications (ALOS, 1997).....	14
Table 5: Sensitivity vector components for ALOS in ascending and descending passes.....	15
Table 6: The main shock parameters (INGV-S4 project website).....	28
Table 7: QRCMT for the main shock (INGV-S4 project website).....	28
Table 8: QRCMT for the after-shock of April 7th (INGV-S4 project website).....	29
Table 9: QRCMT for the after-shock of April 9th (INGV-S4 project website).....	29
Table 10: Parameters of the two significant after-shocks (INGV-S4 project website).....	29
Table 11: Basic characteristics of the ASTER GDEM (ASTER G-DEM, 2007).....	37
Table 12: Comparison ASTER GDEM with SRTM DEM (ASTER G-DEM, 2007).....	38
Table 13: LANDSAT-7 scenes used for making NDVI map.....	40
Table 14: Minimum detectable displacements by AMPCOR for some supported data sets.....	46
Table 15: Minimum detectable displacement by COSI-Corr for supported data sets.....	47
Table 16: Terra and ASTER specifications (ASTER, 2004).....	47
Table 17: ENVISAT ASAR image pairs for interferometry.....	53
Table 18: ENVISAT ASAR image pair for interferometry.....	57
Table 19: ALOS PALSAR image pairs for interferometry.....	60
Table 20: ENVISAT ASAR image pairs for SCT.....	66
Table 21: ASTER image pairs for SCT.....	70
Table 22: RMSE for initial and standard deviation for optimized GCPs.....	71
Table 23: Correlation parameters for applying SCT on the ASTER images.....	71
Table 24: Source parameters for the Paganica fault from InSAR inversion and seismological methods.....	78
Table 25: Source parameters for the Paganica fault (Walters et al., 2009).....	79
Table 26: LS inversion model parameters for the Paganica fault.....	82
Table 27: ENVISAT image pairs for applying SCT on the Bam earthquake, Iran.....	86
Table 28: Summary of measured subsidence and uplift along the satellite LOS direction.....	93
Table 29: Geometrical parameters of the causative fault derived from the NA approach.....	93
Table 30: Source parameters of the causative fault derived from the LS inversion.....	94
Table 31: Earthquake sequence for L'Aquila area since April 5th, 2009 till April 20th, 2009 with magnitude greater than 4.0 (EMSC, 2009).....	113
Table 32: List of applications and codes used in this research.....	114
Table 33: ERS-1/2 interferometric image pairs.....	114
Table 34: ASTER GDEM quality assessment.....	115
Table 35: ASTER spectral bands and spatial resolutions (ASTER, 2004).....	115
Table 36: Number of fringes in different directions for ENVISAT ASAR interfer-	

ometric pairs.....	115
Table 37: Coseismic horizontal displacements at L'Aquila near filed GPS stations (Anzidei et al., 2009).....	116

Abstract

On Monday April 6th, 2009, the city of L'Aquila in centre of Italy, and the surrounding area, was shocked by an earthquake of M_w 6.3. The main shock inflicted serious damage to the city and other surrounding towns and villages, and killed several hundred people.

Deformation of the ground surface caused by this earthquake, and source parameters of the causative fault, were studied in this research using three different techniques: Synthetic Aperture Radar Interferometry (InSAR), Sub-pixel Correlation Technique (SCT) and Geophysical Inversion problem, and different image data sets of optical and Radar sensors. None of these techniques offer a complete study of a seismic event, and hence, these three techniques were employed here to study the earthquake from different perspectives. Results, from both optical and radar sensors, have been compared in each section. The results were also compared with results from other similar studies.

InSAR was applied to ENVISAT ASAR and ALOS PALSAR image data sets, in ascending and descending passes, to reveal deformation along the satellite line of sight direction. The Enhanced Lee filter was applied to ALOS PALSAR interferograms to remove temporal noises. The earthquake affected an ellipse-shaped area 25 km long and 15 km wide, roughly equal to 300 km². The initial coseismic surface deformation started from the north of the main event epicentre. Most of the post-seismic relaxation occurred after April 7th, toward the south and south-east of the main shock epicentre and became more homogeneous around the main event. While the results from both the ENVISAT and the ALOS data sets are strongly supportive, the former data set shows more subsidence in the satellite line of sight direction. Maximum 28.1 cm subsidence along the satellite line of sight was observed on the descending interferogram from the ENVISAT ASAR data set, to the north-west of Onna village.

SCT was applied to both the ASTER and the ENVISAT ASAR data sets to discover horizontal displacements of the affected area. Even though the exact amount and pattern of horizontal displacement could not be determined using these data sets, it was shown that the horizontal displacement was not significant (not more than a few centimetres). This result was confirmed by GPS observations. It was also observed that both the optical and SAR data sets are highly sensitive to temporal variations; however, the SAR data set shows higher coherency values.

A geophysical Inversion problem was applied using a two-step procedure (neighbourhood algorithm and linear least square) to two deformation models which were obtained from InSAR, to find the source parameters of the causative fault, and dislocation model at depth. Neighbourhood algorithm showed that almost a pure normal faulting system, with approximately 11.5 km length and 8.0 km depth, strikes 144° from north-west to south-east and dips 54° toward south-west. The linear least square inversion showed a maximum 1.2 m dip slip on the fault plane and predicted a fracture of 2~3 km long, on the ground surface.

در پگاه دوشنبه ششم آوریل ۲۰۰۹ برابر هفدهم فروردین ۱۳۸۸، زمین‌لرزه‌ای به بزرگی ۶.۳ درجه در مقیاس ریشتر، منطقه لاکوئیل^۱ در استان آبروزی^۲ واقع در مرکز ایتالیا را لرزاند و علاوه بر وارد کردن خسارهای جانی و مالی فراوان، آثار تاریخی شهر لاکوئیل را ویران ساخت.

در این پژوهش، تغییرات ایجادشده در سطح پوسته زمین در اثر این زمین‌لرزه و هندسه و پارامترهای گسل مسبب، با سه روش تداخل‌سنجی راداری^۳، جابجایی‌سنجی^۴ و اینورژن ژئوفیزیکی^۵، با استفاده از داده‌های ماهواره‌های مختلف بررسی شده‌است. هیچ‌یک از این سه روش، به‌تنهایی برای بررسی کامل پدیده‌های زلزله‌شناختی کامل نیستند و از این رو در این تحقیق به‌صورت مکمل و توأمان، برای بررسی هرچه کاملتر این زمین‌لرزه بکارگرفته شده‌اند. در هر بخش، افزون بر برابری نتایج حاصل از داده‌های مختلف، نتایج بدست‌آمده با سایر تحقیقات مشابه نیز مقایسه و نقاط ضعف و قوت هر یک بیان شده‌است.

تداخل‌سنجی راداری، دانشی است که با استفاده از مولفه‌ی فاز دو تصویر راداری که یکی قبل و یکی بعد از زمین‌لرزه از مکانهای به‌نسبت نزدیک‌به‌هم گرفته شده‌اند، استفاده کرده الگوی تغییرات بین دو تصویر را که در این مورد بیشتر ناشی از جابجایی‌های پوسته زمین است، بدست می‌دهد. چون این فن به‌لحاظ هندسه تصویربرداری راداری، بیشتر به مولفه قائم جابجایی حساس است، در این پژوهش برای بررسی جابجایی‌های سطح زمین در راستای محور دید ماهواره، بکارگرفته شده است. در این بخش، از تصاویر راداری دو ماهواره ENVISAT و ALOS استفاده و نتایج بدست‌آمده با هم مقایسه شده‌اند. نتایج در این بخش نشان می‌دهند که در اثر این زمین‌لرزه، منطقه‌ای بیضی‌شکل به‌طول ۲۵ و به‌عرض ۱۵ کیلومتر حداکثر به‌میزان ۲۸.۱ سانتیمتر در راستای دید ماهواره، نشست کرده است. دگرذیسی اولیه در سطح زمین، از شمال کانون زمین‌لرزه اصلی آغاز شده، اما بویژه پس از ۹ آوریل، به سمت جنوب و جنوب شرقی گسترش یافته و الگوی به‌نسبت متقارنی را پیرامون این کانون ساخته است.

جابجایی‌سنجی، دانشی است که با استفاده از دو تصویربرداری نوری و یا مولفه دامنه و گاهی فاز دو تصویر راداری، جابجایی‌های افقی پوسته زمین را، در بازه زمانی بین دو تصویر، با دقتی بسیار بهتر از ابعاد پیکسل تصویری محاسبه می‌کند. این فن مکمل تداخل‌سنجی راداری است و به‌خوبی ضعف آن را در بررسی حرکات افقی پوسته زمین پوشش می‌دهد و از این رو در این پژوهش برای بررسی حرکات افقی پوسته زمین، بکارگرفته شده است. در این قسمت از تصاویری نوری سنجنده ASTER و تصاویر راداری ماهواره ENVISAT استفاده شده است. این روش به‌همراه تداخل‌سنجی راداری، ابزارهای موثری برای ارزیابی اولیه خسارهای ناشی از زمین‌لرزه هستند. نتایج این بخش نشان می‌دهند که حرکت‌های افقی پوسته زمین در اثر این زمین‌لرزه، از چندین سانتیمتر تجاوز نمی‌کند. این نتیجه با مشاهدات GPS تایید شده است. همچنین مشاهده شد که تصاویر نوری و راداری هر دو به تغییرات زمانی سطح زمین حساس هستند؛ اما سطح حساسیت تصاویر راداری بالاتر است.

در مساله اینورژن، از نتایج واقعی اندازه‌گیری‌ها استفاده شده، مقادیر پارامترهای مشخص‌کننده سیستم بدست می‌آیند. انتقال از فضای داده‌ها به فضای پارامترهای مدل، نتیجه‌ای از تعامل سامانه‌ای فیزیکی مانند زمین، جو و یا میدان جاذبه است. با بکارگیری مساله اینورژن در ژئوفیزیک، پرسشهایی همچون استنتاج هندسه گسل و یا چگونگی توزیع جابجایی روی صفحه گسل، پاسخ داده می‌شود و به‌همین منظور نیز در این پژوهش بکارگرفته شده‌است. نتایج این قسمت اهمیت بسیاری در شناخت رفتار مکانیکی گسل‌های فعال دارد. در این قسمت از مدل‌های جابجایی بدست‌آمده از تصاویر راداری ماهواره ENVISAT در بخش اول، استفاده شده است. نتایج این بخش نشان می‌دهند که گسل مسبب این زمین‌لرزه با ساختار نرمال و به‌طول تقریبی ۱۱.۵

- 1 L'Aquila
- 2 Abruzzi
- 3 Interferometric Synthetic Aperture Radar
- 4 Sub-pixel Correction Technique
- 5 Geophysical Inversion problem

کیلومتر، در امتداد ۱۴۴ درجه از شمال غربی به جنوب شرقی امتداد و ۵۴ درجه به سمت جنوب غربی شیب دارد و در اثر این زمین لرزه در بازه‌ای به طول ۲ تا ۳ کیلومتر گسیخته شده است.

هرچند در این پژوهش، زمین لرزه ششم آوریل در ناحیه لاکوئیلای ایتالیا از جنبه‌های گوناگون، با استفاده از داده‌ها و روشهای مختلف بررسی و تفسیر شده، این تحقیق همچنان باز و قابل تکمیل و گسترش است و به همین منظور نیز در بخش پایانی پیشنهادهایی برای تکمیل و ادامه کار، داده شده است.

در پایان خاطر نشان می‌شود انجام چنین پژوهشهایی در مورد کشور به راحتی امکان پذیر است و در صورت اجراء تکمیل و تعمیم آن در سایر موارد جابجاییهای سطح زمین مانند مطالعه زمین لغزشها، زمین رانشها، فرونشستها (در اثر استخراج معادن، آبهای زیرزمینی یا سفره‌های نفتی و گازی)، رسوب گذاری ساحلی، تپه‌های شنی روان و فعالیتهای آتشفشانی، می‌تواند در خدمت حفظ جان و مال انسانها قرار گیرد.

Acknowledgements

All my praises and worship for the Almighty, who gave me the ability to overcome difficulties and complete my study, as well as this great experience. I have met so many fantastic people, encountered a wealth of culture and learned great a deal and so much more than just about Geoinformation. I hope God gave this opportunity to me to apply my knowledge for decreasing the impact of natural disasters and bringing peace, welfare and comfort for human societies. Also, I would like to sincerely thank the following people who helped me during my study time:

My teacher in BSc course, Dr. Ali Abkar, for recommending GEM course to me.

My father, my brother and my father-in-law for their encouragement and financial support, despite very tough circumstances back in my country. My father has always encouraged me to continue my educations in a higher degree and did his best to pave the way.

My wife, Bahareh, who endured difficulties during our travel and stay in Europe and always did her best to take care of our daughter and home. And also my daughter, Parmida, who deserves my attention and presence in her childhood. They suffered a lot during my thesis due to my absence, and did not always receive the attention they deserve.

My friend and senior brother, Mozafar Goudarzipour, for his kindness, consideration and assistance during my stay in UK.

My supervisors, Dr. Tsehaie Woldai and Dr. Valentyn Tolpekin for their friendly support, encouragements and comments to improve the quality of my thesis. Their scientific ideas and suggestions were a constant source of guidance during my research.

My colleague and my friend, Michel Peyret, from University of Montpellier II, France, for his scientific support. Not only he was the first one who taught me this technique, but I also learnt to have a scientific attitude and patience from him. He patiently endured my endless questions and always had confidence in me. He reviewed and constructively commented on my thesis. Also, the Inversion codes were kindly provided by him. My research should have been impossible without his support.

My friend, Dr. Abbas Farshad, for reading my thesis and his comments from a geology point of view.

Andrew Newman, from School of Earth and Atmospheric Sciences, the Georgia Institute of Technology, Atlanta, for providing codes for converting ROI_PAC outputs to GMT grid format.

Eric Fielding, from JPL, NASA, for providing snaphu.pl code, before public distribution.

My friend and classmate, Alexis McIntyre, for reviewing some parts of my thesis and her comments from an English language point of view.

My friend, Valentina Spanu, for translation of geology terms from Italian to English.

Gerard Reinink, from the IT department of ITC, for his kind assistance in ordering and providing satellite image data sets.

ESA, for providing a complete SAR data set for the earthquake of April 6th, 2009, Italy.

USGS EROS data centre, for providing a privileged account to have access to ASTER and LANDSAT image data sets.

And finally, the EU, for funding such a great program and offering the scholarship to students, all the GEM course coordinators, all of my teachers and all of people behind the organization of such a this great course.

Mohammad Ali Goudarzi
January 2010
Enschede, The Netherlands

Abbreviations

The following list, shows most important abbreviations used in this dissertation. General and common abbreviations such as m (stands for meter) or geographical directions are not mentioned here.

- 1GP: Mono-Gyroscope Piloting
- 3GP: Three-Gyroscope Piloting
- ACM: the Association for Computing Machinery
- ALOS: Advanced Land Observation Satellite
- ambig.: Ambiguity
- AMI: Active Microwave Instrument
- AP: Supersintema di Aielli-Pescina (Aielli-Pescina's super-sintema¹)
- ASAR: Advanced Synthetic Aperture Radar
- Asc.: Ascending
- ASPRS: American Society for Photogrammetry and Remote Sensing
- ASTER: Advanced Spaceborne Thermal Emission and Reflection Radiometer
- atm.: Atmosphere
- AVM: Sintema di Valle Majelama (Valle Majelama's sintema¹)
- B/H: Baseline to Height ratio
- BIS: Bisciaro
- BW: Body Wave
- BWM: Body Wave Magnitude (denoted as m_b)
- Caltech: California Institute of Technology
- CBZ: Calcare a Briozoi e Litotamni (Limestones with bryozoa and lithothamnium)
- CERES: Clouds and the Earth's Radiant Energy System
- CGIAR: Consultative Group on International Agricultural Resource
- CGIAR-CSI: CGIAR Consortium for Spatial Information
- CIR: Calcare Ciclotemici Requiemie (Cyclotomic limestones)
- CISP: Congress on Image and Signal Processing
- CMT: Centroid Moment Tensor
- CNMCA: Centro Nazionale di Meteorologia e Climatologia Aeronautica
- CNT: Centro Nazionale Terremoti
- COSI-Corr: Co-registration of Optically Sensed Images and Correlation
- COSMO-SkyMed: CONstellation of small Satellites for the Mediterranean basin Observation
- CPTI: Catalogo Parametrico dei Terremoti Italian
- CROSS: Online satellite image search and order system
- CSUR: ACM Computing Surveys
- DBMI: Data Base Macrosismico Italiano
- DC: Doppler Centroid
- DEM: Digital Elevation Model
- DEOS: Department of Earth Observation and Space Systems (of Delft University of Technology)
- Des.: Descending
- DFCB: Data Format Control Book
- DIC: Digital Image Correlation

1 Sintema: fundamental structural unit of stratigraphy and the main recognized type of the unit with non-conformal limits.

DInSAR: Differential Interferometric Synthetic Aperture Radar
disp.: Displacement
DN: Digital Number
DORIS: Doppler Orbitography and Radiopositioning Integrated by Satellite
EBM: Extra-Backup Mode
EGM96: Earth Gravity Model 1996
EMS: Electromagnetic Spectrum
EMSC: European-Mediterranean Seismological Centre
ENVISAT: Environmental Satellite
EOLi: Earth Observation Link
EROS: Earth Resources Observation and Science
ERS: European Remote Sensing satellite
ERSDAC: Earth Remote Sensing Data Analysis Centre
ESA: European Space Agency
ETM+: Enhanced Thematic Mapper Plus
FBD: Fine Beam Dual-polarization
FBS: Fine Beam Single-polarization
FORMOSAT: FORMOSA Satellite
FS: Fine Scan
FST: Fourier Shift Theorem
G: Giga
GCMT: Global Centroid Moment Tensor
GCP: Ground Control Point
GDEM: Global DEM
GEER: Geo-engineering Extreme Events Reconnaissance
GeoTIFF: Geostationary earth orbit Tagged Image File Format
GIS: Geographic/ Geographical Information System
GLCF: Global Land Cover Facility
GLOVIZ: USGS Global Visualization Viewer
GMT: Generic Mapping Tools
GNSS: Global Navigation Satellite Systems
GP: Gyroscope Piloting
GPS: Global Positioning System
GRASS: Geographic Resources Analysis Support System
HDF: Hierarchical Data Format
hgt: Height
HH: Horizontal/ Horizontal
HV: Horizontal/ Vertical
Hz: Hertz
IDL: Interactive Data Language
IEEE: Institute of Electrical and Electronics Engineers
IGARSS: International Geoscience And Remote Sensing Symposium
Imageodesy: Image Geodesy
INGV: Istituto Nazionale di Geofisica e Vulcanologia
InSAR: Interferometric Synthetic Aperture Radar
IS: Image Swath
ISPRA: Istituto Superiore per la Protezione e la Ricerca Ambientale
JAXA: Japan Aerospace Exploration Agency
JERS: Japanese Earth Resources Satellite

JPL: Jet Propulsion Laboratory
 LMS: Local Magnitude Scale (denoted as M_L)
 LOS: Line Of Sight
 LP DAAC: Land Processes Distributed Active Archive Centre
 LS: Least Square
 M: Mega
 M_0 : Seismic Moment
 m_b : Body-wave Magnitude
 M_L : Local Magnitude
 M_w : Moment Magnitude
 MAP: Maximum A-posteriori Probability
 Max.: Maximum
 MCS: Mercalli-Cancani-Sieberg
 METI: Ministry of Economy, Trade, and Industry
 min: minute
 Min.: Minimum
 MISR: Multi-angle Imaging SpectroRadiometer
 mm: millimetre
 MMS: Moment Magnitude Scale (denoted as M_w)
 MODIS: Moderate Resolution Imaging Spectroradiometer
 MOPITT: Measurements of Pollution in the Troposphere
 MYBP: Million Years Before Present
 NA: Neighbourhood Algorithm
 NASA: National Aeronautics and Space Administration
 NCC: Normalized Cross Correlation
 NDVI: Normalized Difference Vegetation Index
 NIR: Near Infra-Red
 NP: Nodal Plane
 OPTIM: Optimization of Electrical and Electronic Equipments
 PALSAR: Phased Array type L-band Synthetic Aperture Radar
 Pixel: Picture Element
 PRF: Pulse Repetition Frequency
 QA: Quality Assessment
 QRCMT: Quick Regional Centroid Moment Tensor
 QUEST: Quick Earthquake Survey Team
 Radar: Radio Detection And Ranging
 RDO: Calcari a Rudiste e Orbitoline (Limestones with rudists and orbitolina)
 ROI_PAC: Repeat Orbit Interferometry PACKage
 RSNC: Rete Sismometrica Nazionale Centralizzata
 SAR: Synthetic Aperture Radar
 SCC: Scaglia Cinerea¹
 SCT: Sub-pixel Correlation Technique
 SCZ: Scaglia Detritica²
 sec: second
 SIAM: Society of Industrial and Applied Mathematics
 Sinc: Sinus cardinal

-
- 1 A kind of limestone and marl with *Poseidonia oceanica* (algae).
 - 2 Same as SCC, but it is detritic.

SIR: Shuttle Imaging Radar
SLC: Scan Line Corrector (in optical imagery concept)
SLC: Single Look Complex (in Radar imagery concept)
SLR: Satellite Laser Ranging
SNAPHU: Statistical-cost Network-flow Algorithm for PHase Unwrapping
SNR: Signal to Noise Ration
SPOT: Satellite Pour l'Observation de la Terre
SRFT: Satellite Radar Feature Tracking
SRTM: Shuttle Radar Topography Mission
stdev.: standard deviation
SWIR: Short Wave Infra Red
TIR: Thermal Infra-Red
TM: Thematic Mapper
topo.: Topography
UAP: Unità Arenaceo-Pelitica (Arenaceus pelitic unit)
UAM: Unità Argilloso-Marmosa (Argillaceous clay unit)
USGS: United States Geological Survey
UTC: Coordinated Universal Time
UTM: Universal Transverse Mercator
VH: Vertical/ Horizontal
VLBI: Very Long Baseline Interferometry
VNIR: Visible and Near Infra Red
VV: Vertical/ Vertical
WGS84: World Geodetic System 1984
WIST: Warehouse Inventory Search Tool
WRS: Worldwide Reference System
YCM: Yaw Control Monitoring
YCM-R: Yaw Control Monitoring-Regional
yr: year
ZGM: Zero-Gyroscope Mode

Chapter 1

The Moving Finger writes; and, having writ,
Moves on:

Omar Khayyam, Rubaiyat (translated by Edward Fitzgerald)

1 Introduction

Earth is a dynamic and changing system. Outer surface of the earth is divided to several rigid blocks, so-called 'tectonic plates', that are gradually moving across the surface. Earthquakes, volcanic activity, mountain-building, and oceanic trench formation can occur along tectonic plate boundaries. Earthquakes happen when the displacement jerks suddenly in response to an endogenous force being applied to crustal rocks (stress).

The deformations associated with these seismic events, can be measured and evaluated using several different methods, such as seismology, Radar and optical remote sensing, terrestrial geodesy and geodetic field surveying (Peyret et al., 2007). Despite the advantages of each method, none of them is complete enough to explore all aspects of a seismic process. For instance, teleseismic waves have been used to deduce first order characteristics of a seismic event since late 1970s, while deformation velocity and spatial distribution of slip can be inferred using near-field strong ground motion recorders in a well-instrumented area (Archuleta, 1984). However, such a well-instrumented condition is rare, and consequently other methods for measuring surface deformation such as Global Navigation Satellite Systems (GNSS), Synthetic Aperture Radar Interferometry (InSAR) and Sub-pixel Correlation Technique (SCT) can complete seismological methods efficiently.

Geophysical applications of Radar interferometry using remotely sensed Synthetic Aperture Radar (SAR) images for measuring earth surface changes started in the 1990s and applied for studying major earthquakes since the last decade (Massonnet and Feigl, 1998). InSAR has been widely used as a power-proved technique to reveal centimetre-scale deformation of earth surface resulting from earthquakes and volcanic events, as well as sand dunes migration, glaciers flows, land slides creeping movements and subsiding areas (Bamler and Hartl, 1998).

Measuring horizontal surface displacement, on the other hand, is possible from SAR images, either in amplitude (Jonsson et al., 2002) or complex space (Sarti et al., 2006), and optical remotely sensed data using sub-pixel correlation technique (SCT) (Berthier et al., 2005).

Geodetic data for a deformed area can be processed further, using concept of Inversion problem for estimating the characteristics of fault parameters and dislocation (Peyret et al., 2007). Such a information has high level of importance for understanding and interpreting coseismic crustal deformation and exploring the mechanical behaviour of a seismic fault.

In this research, InSAR, SCT and Inversion techniques will be used respectively for detecting and measuring earth surface deformation and finding geometry and source parameters of the

causative fault and distribution of slip along the fault plane, induced by the M_w 6.3 earthquake of April 6th, 2009, in L'Aquila, Italy.

1.1 Research problems statement

On April 6th, 2009, L'Aquila area in centre of Italy was shocked by an M_w 6.3 earthquake. The last previous major earthquake in this area happened in 1980 in Popoli, about 39 km to the south-east of L'Aquila (Gruppo di lavoro CPTI, 2004; see §3.2.3), and consequently the area has never been studied using space geodesy techniques. In spite of a huge damage to the city of L'Aquila, the earthquake has provided a good opportunity for researchers to study the geology and structure of the active faults, in the area.

Several studies have been done before, to measure surface displacements and crustal deformation with high level of precision using different available methods (e.g. Larson et al., 2003; Segall and Davis, 1997; van Dam and Wahr, 1987). Among them, InSAR has been proved effectively with millimetre level of accuracy in many earthquake prone areas (e.g. Wright et al., 2001; Fialko et al., 2001; Pathier et al., 2003; Peyret et al., 2007).

Most of studies which have been done up to now, have been limited to the use of one or two Radar sensor data sets with same imaging geometry and characteristics (e.g. ERS-1/2 and ENVISAT), in either ascending or descending pass, or same imaging mode. Very few studies, which were available for the author, have paid attention to applications of different data sets, e.g. Radar and optical images and other geodetic data sets (e.g. spirit levelling) for revealing surface displacements and crustal deformation (e.g. Peyret et al., 2008a; Peyret et al., 2008b). Same condition holds also true for showing synergy among the different techniques, such as InSAR, SCT, GPS or spirit levelling.

On the contrary, a newly developed procedure by Leprince et al., 2007a, not only allows for accurate estimation of sub-pixel accuracy displacement between pre- and post-seismic remotely sensed optical images, but can also be used to test, complement and validate the results obtained from other methods.

This research intends to study the April 6th, 2009, earthquake in L'Aquila area and in the meanwhile, will address these technical issues, as much as possible in the limited research period. Validation of results will be done quantitatively using similar data sets and results of other methods and studies.

1.2 Research objectives

The following objectives have been considered for this research which are divided into general and specific categories.

1.2.1 General objective

To study surface deformations resulted from M_w 6.3 L'Aquila earthquake of April 9th, 2009, using Synthetic Aperture Radar Interferometry (InSAR), Sub-pixel Correlation Techniques (SCT) and Inversion problem.

1.2.2 Specific objectives

More results are expected to be addressed by this research, as following:

1. To determine geometrical parameters of the causative fault.

2. To map dislocation model and distribution of slip for the causative fault at depth.
3. To compare displacements derived from different data sets in order to find the most appropriate data sets applicable for other similar case studies.
4. To reveal horizontal surface displacements using optical and Radar image data sets.

1.3 Research questions

To comply with the objectives, the following questions are expected to be answered:

1. How much is the maximum displacement in the satellite line of sight (LOS) direction? and how is the the distribution and pattern of the deformation?
2. What are the the geometrical parameters (length, depth, strike, dip and slip) of the causative fault?
3. How is the slip distribution pattern and dislocation model of the causative fault at depth?
4. How much are the results from different interferometric data sets, in agreement? Which aspect of a seismic event can be addressed better by a specific data set?
5. How strong is the SCT procedure to reveal horizontal surface displacements (specially for normal faults)?

1.4 Research hypotheses

Regarding the objectives and research question, the following null hypotheses are anticipated:

1. H_0 : Deformation in the satellite LOS direction would be detectable and significant.
2. H_0 : The causative fault is normal (USGS, 2009a).
3. H_0 : Slip is distributed on the fault plane in depth and is depreciated to the surface.
4. H_0 : Results from different SAR data sets with same passes are consistent, except in low coherence area.
5. H_0 : Strength of the SCT procedure depends on the resolution of input images and stability of the sensor and the platform.

Chapter 2

Soothsayer: In Nature's infinite book of secrecy,
A little I can read.

Shakespeare, Antony and Cleopatra

2 Literature review and background

The earth surface is shaped by the interaction of constructional and erosional processes over geologic time-scales. To study of these processes, specially seismic events, either on the terrain surface or in depth, has high level of importance for preventing human life, and infrastructures, and bring vital information for planning future activities and development.

Knowledge of coseismic ground deformations and geometry of the ruptured fault is necessary for investigation of a seismic rupture mechanics. However, the revolutionary coseismic deformation is not a simple process, and consequently can not be studied by a single method or a solution.

Before the advent of space geodesy, measurements of surface motions relied on terrestrial methods of which, triangulation, trilateration, and spirit levelling were the most commonly used techniques. Despite the high level of accuracy and precision, terrestrial techniques are faced with limitations, some of them have been discussed in Burgmann et al., 2000.

Space geodetic methods, which rely on measurements of signals from earth-orbiting satellites or extraterrestrial objects, such as GPS, VLBI, SLR, InSAR and so on, can provide a reliable tool for study of crustal deformation. While GPS has been the most current and dominant tool for study of deformation along active plate boundaries, plate tectonic motions and deformation on volcanoes (e.g. Segall and Davis, 1997), InSAR brings special unique features and capabilities in this context such as study of active processes which are inaccessible with the traditional methods. Moreover, InSAR measures total deformation between two SAR acquisitions in the satellite LOS direction with high spatial resolution over a wide area, while other techniques such as GPS, have much lower spatial resolution (Samsonov and Tiampo, 2006).

Although, InSAR is a power-proved tool to study surface deformations, it has its own limitations, that could be compensated with other methods, such as image correlation technique and inversion problem for estimation of horizontal displacement (specially along ruptures) and characteristics of a fault dislocation at depth, respectively.

This research is done in three major parts: InSAR, SCT and Inversion problem, in accordance with this introduction and get benefit from these complementary techniques. There are numerous literature about physical principles and mathematical background of each part. However, those concepts and formulae which have key importance for carrying out the research and for interpreting the results, are presented here as a reference for the next chapters.

2.1 SAR interferometry

Synthetic Aperture Radar Interferometry (InSAR), is a technique which is applied to phase component of two SAR images acquired from relatively close positions to distinguish and study the interference patterns between the two images. InSAR can provide spatially continuous measurement of deformed fields (Massonnet and Feigl, 1998).

During the two past decades, InSAR evolutionarily developed from a theoretical concept to a technique, and it has revolutionized a wide range of earth science fields. InSAR was first published by Goldstein et al., 1988. Goldstein and colleagues used SEASAT L-band SAR data and combined complex data from two scenes of three days apart over the same region in Cotton ball Basin of Death Valley, California.

There are a large number of reviews about theory and applications of InSAR (e.g. Griffiths, 1995; Massonnet and Feigl, 1998; Madsen and Zebker, 1998, and Rosen et al., 2000), all emphasize that in recent years, InSAR has proved its abilities for detecting, measuring and monitoring centimetre-scale changes of the earth's surface.

2.1.1 Applications of InSAR in earth sciences

Applications of InSAR for measuring changes in the earth's surface have emerged in the early 1990s (Massonnet and Feigl, 1998). InSAR provides a new tool to map global topography and deformation of the earth surface. Commencing geophysical applications of InSAR, in the late 1980s and early 1990s, were included topography extraction (Graham, 1974; Zebker and Goldstein, 1986), measurement of ice stream motion (Goldstein et al., 1993) and seismic strain (Massonnet et al., 1993; Zebker and Rosen et al., 1994).

In the past decade significant improvements have been taken place in understanding of earthquakes, volcanoes, and glaciers as a direct result of this technique.

Different crustal deformation can be classified according to rate and duration. For example earthquakes can displace the crust with high rate (~ 1 m/sec) but within a short duration (10 s), while at the other extreme, post-seismic relaxation and post-glacial rebound of the lithosphere are slow in rate (~ 1 mm/sec) but long in duration ($10^1 - 10^3$ yr). Massonnet and Feigl, 1998, have divided this interval into ten orders of magnitude in rate and six in duration. They catalogued successful applications of interferograms according to these two scales, from short and fast to long and slow phenomena.

Capturing an earthquake and mapping the induced deformation, is one the most frequent applications of InSAR. If the earth surface deformed between two acquired Radar images, surface displacement map with sub-centimetre accuracy can be achieved in the absence of atmospheric signals (Sarti et al., 2006).

Conditions for applicability of InSAR for seismic events have been explained well in Massonnet and Feigl, 1998, and applied by a numerous researchers (e.g. Fialko et al., 2001; Wright et al., 2001; Funning et al., 2005; Peyret et al., 2008a) for different cases. Some of the researches have been done purely with InSAR, while others combined other geodetic techniques, e.g. spirit levelling, as well (e.g. Peyret et al., 2007).

InSAR is a well-suited technique to survey volcanism, because the typical deformation rate of several centimetres per month is easy to measure with monthly passes of SAR satellites (Massonnet and Feigl, 1998). Rosen et al., 1996, have used SIR-C/X-SAR and L-band data sets

to survey Kilauea Volcano, Hawaii, and revealed apparent surface displacement. Zhong et al., 2002, have studied several volcanoes in Alaska including Okmok, Akutan, Kiska, Augustine, Westdahl, and Peulik volcanoes using InSAR.

Glaciers and ice flows are another instances of earth surface changes have been studied by InSAR. Because of the ice movement speed, which can be quite rapid and sometimes reaching velocities of the order of 1 m/yr, it can create spectacular fringe patterns in interferograms (Massonnet and Feigl, 1998). This phenomenon, has been studied by number of researchers. Gray et al., 1998, used this method to derive ice motion from RADARSAT data set in Antarctic, whilst Quincey et al., 2007, have studied dynamics and structure of glaciers in Tibet (China) and Nepal as an early recognition of glacial lake hazards.

Geomorphology and hydrology can also benefit from InSAR. A growing amount of works show that it is possible to obtain centimetre-scale motions associated with geomorphological and hydrological phenomena by InSAR. Smith, 2002, enumerates seven different applications of InSAR in this field: 1- slope motion; 2- land subsidence; 3- sediment erosion/ deposition; 4- soil moisture; 5- river inundation; 6- snow cover, and 7- river ice. As an another example, Peyret et al., 2008a, have combined InSAR and GPS observations to quantify and analysis the spatial and temporal evolution of the surface displacement of a large landslide in central Alborz mountain range (Iran).

DEM generation is another application of InSAR. Radar images taken from close viewing directions allow to construct DEM of the area with accuracy of a few meters (Massonnet and Feigl, 1998). The near-global DEM of the world generated by Shuttle Radar Topography Mission (SRTM), is a good example for applicability of InSAR to make a digital topographic database of the earth (SRTM, 2009).

InSAR is not limited to solid parts of earth surface and has been used in many other disciplines. For example, Goldstein and Zebker, 1987, proposed a method for measuring ocean surface movement using two interferometric Radar measurement.

2.1.2 Interferometry equations

Mathematical theory of InSAR has been elaborated in a number of references in details (e.g. Franceschetti and Lanari, 1999) and one can refer to them for more details. Certain equations, however, have key importance for the current research and are therefore referenced from the work of Rosen et al., 1996, to support interpretation of the measurements and results.

The phase difference between the two scenes of an interferometric pair, contains the variations of the satellite-ground distance during the acquisition time interval which is mainly projection of coseismic displacement vector on the satellite LOS direction (Peyret et al., 2007).

The measured phase difference between two corresponding pixels is expressed by interferometry equation after precise co-registration of the two images (Reigber et al., 2007), as follows:

$$\Delta \phi = \phi_{topo} + \phi_{flat} + \phi_{disp.} + \phi_{orbit} + \phi_{atm.} + \phi_{noise} \quad (1)$$

where ϕ_{topo} is topography phase signature, ϕ_{flat} is flat earth phase caused by the imaging geometry, $\phi_{disp.}$ is differential displacement pattern, ϕ_{orbit} is phase error caused by inaccurate orbit parameters, $\phi_{atm.}$ is atmospheric artefacts and ϕ_{noise} refers to noise contribution.

Figure 1A shows interferometric geometry of two imaging Radar systems separated by baseline vector \vec{B} which are in trajectories perpendicular to the page plane. Position 1 and position 2 depicts the base (master image) and the nearly repeating its track imaging system (slave image), respectively.

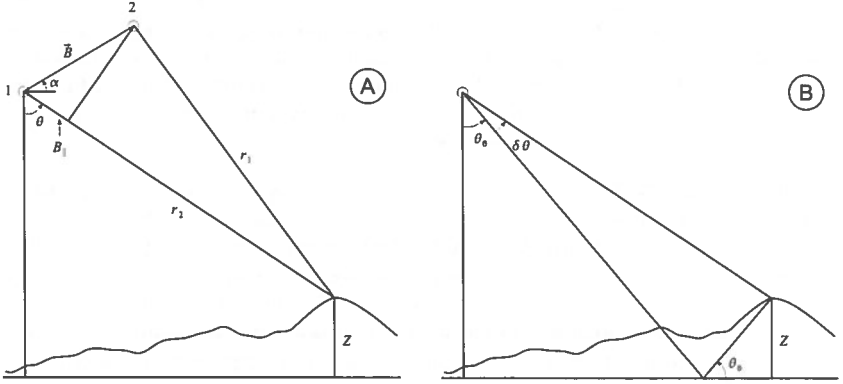


Figure 1: Interferometric geometry (Rosen et al., 1996)

The phase at each Radar image pixel is sum of the backscattered and propagated phase (ϕ_b and ϕ_p , respectively). Propagated phase is equal to $(4\pi/\lambda)r_i$ (§ 2.1.5.2) where, r_i is the range from antenna i to the imaged point. The backscattered phase is nearly equal for two Radars imaging the the same scene with same frequency and similar imaging geometry ($\phi_b = \phi_{b_i}$). By assuming this conditions, the phase difference between the two Radar images at a given point can be calculated by the following formula:

$$\Delta\phi = \phi_1 - \phi_2 = \frac{-4\pi}{\lambda}(r_1 - r_2) \quad (2)$$

In the case of satellite imaging geometry, where $|B| \ll r$, Equation 2 can be written as:

$$\Delta\phi = \frac{-4\pi}{\lambda} \mathbf{B} \cdot \mathbf{l} = \frac{-4\pi}{\lambda} B \sin(\theta - \alpha) \quad (3)$$

where \mathbf{l} is unit vector in the look direction. Because:

$$B_{\parallel} = B \sin(\theta - \alpha) \quad (4)$$

Equation 3 implies that the phase difference is directly proportional to the component of \vec{B} in the look direction. Equation 4 is the so-called 'parallel ray approximation' which has been used by Zebker and Goldstein, 1986.

In order to relate this phase to topography, a terrain surface without local topographic variations is considered. So,

$$\Delta\phi_0 = \frac{-4\pi}{\lambda} B \sin(\theta_0 - \alpha) \quad (5)$$

where θ_0 is the look (or incidence) angle to a given point. When the topography is present, the look angle for a given range is altered by $\delta\theta$ as shown in Figure 1B. In this new condition, Equation 5 will change to:

$$\Delta\phi = \frac{-4\pi}{\lambda} B \sin(\theta_0 + \delta\theta + \alpha) \quad (6)$$

If flat earth phase component is removed from Equation 6, the 'flattened' phase difference is remained:

$$\begin{aligned} \Delta\phi_{flat} &= \Delta\phi - \Delta\phi_0 \\ &\simeq \frac{-4\pi}{\lambda} B \cos(\theta_0 - \alpha) \delta\theta \end{aligned} \quad (7)$$

and because

$$B_{\perp 0} = B \cos(\theta_0 - \alpha) \quad (8)$$

Equation 7 implies that flat earth phase component is directly proportional to the first order of perpendicular component of the baseline referenced to the flat earth and to the small angle $\delta\theta$, which is in turn proportional to topographic height z :

$$\delta\theta \simeq \frac{z}{r_0 \sin \theta_0} \quad (9)$$

The term 'height ambiguity' is equal to the change in elevation required to alter the phase difference by one cycle (2π radian) and is given by:

$$h_a = \frac{\lambda r_0 \sin \theta_0}{2 B_{\perp 0}} \quad (10)$$

The phase difference in repeat-pass interferometry measures all ground displacement between two passes, as well as topography. In the second image, the change in range due to displacement (Δr), enters into the phase difference equation directly:

$$\Delta\phi_{flat} = \frac{-4\pi}{\lambda} B \cos(\theta_0 - \alpha) \frac{z}{r_0 \sin \theta_0} + \frac{4\pi}{\lambda} \Delta r \quad (11)$$

Equation 11 implies that in far range, phase difference is more sensitive to surface displacement than to topography itself. In this equation, $\Delta r = \lambda/2$ gives one cycle of phase difference, while z should change by h_a to make the same change.

The InSAR technique measures earth surface deformations along the satellite LOS direction (slant range) and is partially sensitive to variations perpendicular to this direction (azimuth). The range change observed with InSAR is projection of the displacement vector (\mathbf{d}) on the sensitivity vector (\mathbf{v}) as follows:

$$r = -\mathbf{v}^T \cdot \mathbf{d} \quad (12)$$

Where, $\mathbf{d} = (d_x, d_y, d_z)^T$ is vector of east, north and vertical displacement of a point at the earth surface, and $\mathbf{v} = (v_x, v_y, v_z)^T$ is the unit LOS vector (sensitivity vector) expressed in the same local reference system, pointing from ground to the satellite.

2.1.3 Characteristics of interferometric phase

When two interferometric SAR images are not acquired simultaneously, several fundamental problems interfere in detection and isolation of deformation signature in the processed interferograms (Equation 1).

The principles of different physical interferences have been well explained in other resources (e.g. Rosen et al., 1996; Massonnet and Feigl, 1998; Ferretti et al., 2007). However, a concise summary of important factors that have key roles for interpreting the results, is presented here from Rosen et al., 1996.

The first problem in isolating the motion signature is the change of backscatter phase between observations. These changes can lead to systematic biases to the phase difference measurements, and to randomization of the phase through signal decorrelation. Decorrelation can be a significant barrier to repeat-pass interferometric analysis. Correlation is measured by:

$$\gamma = \frac{\langle c_1 \cdot c_2^* \rangle}{(\langle c_1 \cdot c_1^* \rangle \langle c_2 \cdot c_2^* \rangle)^{1/2}} \quad (13)$$

where c_1 and c_2 are the complex pixel values of the two images that form the interferogram. The asterisk denotes complex conjugation, and angle brackets denote statistical expectation, realized in practice by spatial averaging with a rectangular filter when the interferometric phase varies slowly.

There are three major contributing factors for decorrelation, in repeat-pass interferometry: thermal noise, geometric decorrelation resulted from slightly different imaging geometries and volumetric scattering, and temporal decorrelation due to random wavelength-scale motion of scatterers within a pixel (Zebker and Villasenor, 1992).

The second major problem is the topography itself. Removing the topographic phase signature from an interferogram requires either a reference DEM of sufficient resolution and accuracy, or an independent interferogram without any motion in between. Using a DEM, an interferogram might be synthesized, if the imaging geometry is known. Subtracting the phase differences pixel by pixel, removes the topographic phase and leaves only the phase due to displacement.

The third problem is the atmospheric effects on the Radar signal. When the sensor observing the earth, Radar signals must propagate through the atmosphere, which induces additional phase shifts that are not accounted for in the geometrical model described in § 2.1.2 . There are extensive literature about this problem which are mostly related to Radar altimetry studies (e.g. Goldhirsh and Rowland, 1982).

Propagation through both the dry atmosphere and through atmospheric water vapour adds additional phase delays to the interferogram. In each case, the amount of phase delay is inversely proportional to wavelength, or in other words, the medium is non-dispersive. Since the effect is evidenced as a nearly constant time delay of the Radar signal, independent of frequency at microwave wavelengths, the contamination of the signal can not be corrected using dual-frequency measurements, such as the technique commonly used in ionospheric corrections for GPS signals. Variability in the atmospheric medium on a time scale similar to the repeat-orbit interval, introduces an unpredictable error signal which is added to the desired phase signal.

2.1.4 SAR satellites

The term of 'SAR satellites' in this text, refers to satellites which carry synthetic aperture Radar sensor. There are number of satellites of this type and among them, specifications of ERS-1/2, ENVISAT and ALOS satellites (which can be used potentially in this research) are summarized here.

2.1.4.1 ERS

ERS-1 was the first ESA's earth observation satellite launched at July 1991 and its capabilities for interferometric purposes was validated till September of the same year. It carried a comprehensive payload including its SAR sensor which is called Active Microwave Instrument (AMI). The satellite had various mission phases with 3-days, 35-days and a 336-days repeat cycle. ERS-1 failed on March 2000 (ERS, 2009).

ERS-2 which had same SAR sensor, launched in April 1995 and was a successor for ERS-1 data set. Table 1 summarizes specifications of ERS-2 and the AMI sensor.

Launch date	April 21, 1995
Orbit	Sun-synchronous
Altitude	785 km
Inclination	98° 52'
Period	100 min
Repeat cycle	35 days
Radar sensor	AMI
Frequency	C-band (5.3 GHz)
Wavelength	56.6 mm
Polarization	VV
Incidence Angle ¹	23° at mid swath
Spatial resolution ²	30 m
Swath ¹	100 km
Antenna look	Right

Table 1: ERS-2 and AMI specifications (ERS, 2009)

Shortly after launching ERS-2, ESA put these two satellites in the first ever 'tandem' mission status for nine month, since August 16, 1995, till May 15, 1996. During the tandem mission, ERS-2 was passing the same point on the ground one day later than ERS-1 (Duchossois and Martin, 1995). Because of 24 hours revisit time, which is resulted in more interferogram coherency (§ 2.1.3), this mission offered an extensive and valuable image pairs to scientific communities, specially for DEM extraction purposes (Ferretti et al., 2007).

1 For SAR Image and Wave Mode only.

2 Averaged for SAR Image Mode in multi-looked images.

2.1.4.2 ERS-2 gyroscope problem

ERS-1 and ERS-2 had been piloted with three gyroscopes since the beginning of the ERS mission and they showed high attitude of stability around the orbit (Rosich et al., 2000). However, ERS-2 encountered several gyroscopes malfunctioning since February 2000, when a new yaw-steering mode using only one gyroscope was implemented. Gyroscope problem led to six different piloting modes shown in Figure 2.



Figure 2: Configuration of the ERS-2 piloting modes and corresponding orbit dead-band evolution (Miranda et al., 2004)

Implementation of 'Mono-Gyroscope Piloting mode (1GP)' in February 2000 was intended to ensure continuity of the mission even in the case of additional gyroscopes failure. In January 2001, a new piloting mode using no gyroscopes, named 'Extra-Backup Mode (EBM)', was implemented as a first stage for a gyroscope-less piloting mode. The aim of this challenging mode was to maintain the remaining gyroscopes performance only for those activities which absolutely requiring them, such as some orbit manoeuvres. A more accurate version of this yaw-steering 'Zero-Gyroscope Mode (ZGM)' was operationally used since June 2001. Later on, the performance was even more improved with the implementation of the 'Yaw Control Monitoring mode (YCM)' implemented on March 2002 (Miranda et al., 2004).

The evolution from the nominal and extremely stable 'Three-Gyroscope Piloting mode (3GP)' to the YCM, has allowed to successfully continuing the ERS-2 operations despite the gyroscopes failures for some applications. Nevertheless, this evolution has significantly affected the stability of the satellite attitude and the SAR Doppler Centroid (DC) frequency (Miranda et al., 2004). In other words, each piloting mode has a quality degrading effect on DC frequency stability and consequently on InSAR applications. This effect is elaborated in § 2.1.4.3 .

2.1.4.3 Effect of the gyroscope failure on InSAR performance

The practical consequence of gyroscopes failure is high variation in DC from one acquisition to another. The DC is the centre frequency of the image azimuth bandwidth, which is 1378 Hz for SLC images. Since SLC images have a limited azimuth bandwidth, it is clear that when the DC difference between the two images of an InSAR pair becomes larger, their common azimuth bandwidth decreases and consequently, the InSAR performance is degraded (Rosich et al., 2000).

An indication of the expected InSAR performance for a specific pair, is given by the interferometric coherence, which is a measure of the absolute value of the correlation between the two complex images of an interferometric pair (Equation 13). The value of coherence depends on multiple factors (§ 2.1.3), including the surface characteristics, the time span between acquisitions, the spatial satellite baseline and the percentage of azimuth spectra overlap (Rosich et al., 2000). Impact of the later parameter is expressed as:

$$\text{Doppler dicorrelation} = 1 - \left| \frac{F_{DC_1} - F_{DC_2}}{1378} \right| \quad (14)$$

where F_{DC_1} and F_{DC_2} are the DC frequencies of the two images of the pair, and 1378 Hz is the original azimuth bandwidth of each of the SLC images (Bamler and Just, 1993).

The later factor has been practically constant for all ERS tandem pairs (around 250 Hz) and around 100% for ERS-2 3GP pairs. However, in the new operation mode of ERS-2, this factor varies and its analysis becomes critical (Rosich et al., 2000). As a result, interferometry is almost problematic using the new acquisitions of ERS-2.

2.1.4.4 ENVISAT

It is an earth observing satellite engineered and built by ESA, launched on March 2002. Advanced Synthetic Aperture Radar (ASAR) is the largest ENVISAT sensor, operating at C-band which despite a small central frequency shift (31 MHz), ensures continuity of data after ERS-2 for interferometry purposes (Ferretti et al., 2007). In comparison to its predecessor, it utilizes enhanced capabilities in terms of coverage, range of incidence angles, polarization and modes of operation. Table 2 summarizes specifications of ENVISAT and ASAR sensor.

Launch date	March 1, 2002
Orbit	Sun-synchronous
Altitude	790 km
Inclination	98° 52'
Period	101 min
Repeat cycle	35 days
Radar sensor	ASAR
Frequency	C-band (5.331 GHz)
Wavelength	56.6 mm
Polarization	VV or HH
Incidence Angle ¹	15° to 45.2° (swath 1 to 7; 23° at mid swath 2)
Spatial resolution ²	30 m
Swath ¹	56 km (swath 7) to 105 km (swath 1)
Antenna look	Right

Table 2: ENVISAT and ASAR specifications (ENVISAT, 2009)

Table 3 shows components of incidence vector in three perpendicular directions for ascending and descending orbit passes of ENVISAT satellite, pointing from satellite to the ground which is called 'sensitivity vector' (Sarti et al., 2006, for the term). The table was calculated for 23° incidence, and 105° and 255° heading angles for ascending and descending passes, respectively (see §4.1.2.7). ERS-1/2 satellites have also same sensitivity vector, due to same incidence and inclination angles.

1 For ASAR Stripmap Mode only.

2 Average for precision product in multi-looked images.

Pass	East	North	Up
Ascending	0.377417	0.101129	- 0.92050
Descending	- 0.377417	0.101129	- 0.92050

Table 3: Sensitivity vector components for ENVISAT and ERS-1/2 in ascending and descending passes

2.1.4.5 ALOS

It is an earth observing satellite developed and managed by JAXA, launched on January 2006 as a successor for JERS. The Phased Array type L-band Synthetic Aperture Radar (PALSAR) is the ALOS on-board active microwave sensor, operating at L-band frequency, and in comparison to its predecessor, JERS-1's SAR sensor, provides higher performance (ALOS, 1997). Table 4 summarizes specifications of ALOS and PALSAR sensor.

Launch date	January 24, 2006
Orbit	Sun-synchronous near recursive circular
Altitude	691.65 km
Inclination	98° 16'
Period	98 min
Repeat cycle	46 days
Radar sensor	PALSAR
Frequency	L-band (1.27 GHz)
Wavelength	236 mm
Polarization	Single polarisation (HH or VV) or dual polarisation (HH/HV or VV/VH)
Incidence Angle	8° to 60° (35° at mid swath)
Spatial resolution ¹	10 m
Swath ²	70 km
Antenna look	Right

Table 4: ALOS and PALSAR specifications (ALOS, 1997)

Table 5 shows components of the incidence or the sensitivity vector in three perpendicular directions for ascending and descending orbit passes of ALOS satellite, pointing from satellite to the ground. The table was calculated for 35° incidence, and 104° and 256° heading angles for ascending and descending passes, respectively (see §4.1.2.7).

1 Average for fine resolution mode only.

2 For fine resolution mode only.

Pass	East	North	Up
Ascending	0.556539	0.138761	- 0.819152
Descending	- 0.556539	0.138761	- 0.819152

Table 5: Sensitivity vector components for ALOS in ascending and descending passes

2.1.5 SAR images

A normal digital SAR image, same as other digital images, is a two-dimensional array of small picture elements (pixels). However, despite the ordinary satellite optical images, a complex number is assigned to each pixel in a SAR image that carries amplitude and phase information about the microwave field backscattered by all the scatters within the corresponding resolution cell projected on the ground (Ferretti et al., 2000). In a SAR image, columns are associated with different slant range locations, while rows indicate different azimuth locations.

2.1.5.1 The SAR amplitude image

Amplitude of a SAR image contains values of the measured amplitude of the radiation backscattered toward the Radar, by existing scatterers within a SAR resolution cell. This amplitude depends more on the roughness rather than chemical composition of the scatterers (Ferretti et al., 2000).

The SAR amplitude image is mostly used in SAR applications. However, it can be used also in Sub-pixel Correlation Technique (§ 2.2), to measure large deformation gradient, both in slant range and azimuth (Sarti et al., 2006).

2.1.5.2 The SAR phase image

The radiation transmitted from the Radar antenna should reach the scatterers on the ground and return back to the antenna (two-way travel) in order to form a SAR image. Scatterers at different distances from Radar antenna, introduce different delays between transmission and reception of the radiation (Ferretti et al., 2007).

Principal of InSAR can be illustrated if the transmitted signal is represented as a sine wave. A normal sinusoidal function, e.g. $\sin \phi$, has a period of 2π radian. For a relative narrow band SAR signal, such as ERS and ENVISAT, the transmitted signal can be simplified, of a first approximation, to a pure sinusoidal whose angle or phase ϕ has the following linear dependence on the slant range coordinate r :

$$\phi = 2\pi \frac{r}{\lambda} \quad (15)$$

where λ is the SAR wavelength. Assuming phase of transmitted signal equals to zero, the received phase at antenna which travelled $2R$ distance (from satellite to scatterers and back), can be shown by the following equation:

$$\phi = 4\pi \frac{R}{\lambda} \quad (16)$$

Since the wave travel length to the ground scatterers and back will consist of a number of whole wavelengths plus some fraction of a wavelength, this is observable as a phase difference or phase shift (θ) in the returning wave.

Figure 3 shows the concept of emitted and backscattered phase radiation as well as the phase shift. SAR amplitude is mostly used in SAR applications, while SAR phase is widely used in InSAR applications (§ 2.1.1).

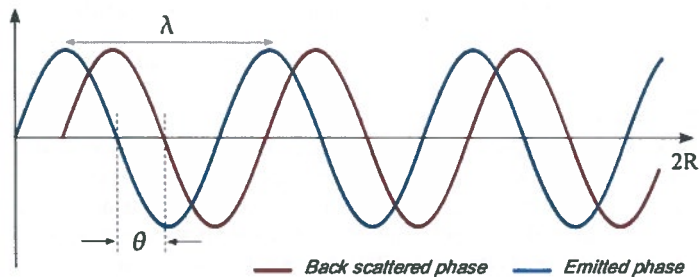


Figure 3: Emitted and backscattered sinusoidal signal

2.1.5.3 Speckle

The presence of several scatterers in a SAR resolution cell generates the so-called 'speckle effect' that is common to all coherent imaging systems (Ferretti et al., 2007). Signals reflected by many small elementary scatterers (in comparison to Radar wavelength) in a resolution cell, are superimposed and make this effect. This effect is not seen in optical imaging systems.

Speckle appears as noise, specially in SAR applications, and hinders its wider use. Some researchers have applied innovative methods to get benefit out of speckles. Lopez-Martinez and Pottier, 2005, for instance, has characterized accurately the coherence parameter, specially in the case of interferometric SAR data, by considering a new model for speckle-noise in multi-dimensional SAR data, and Yu and Fu et al., 2006, have proposed an innovative method named 'contoured correlation interferometry' to generate speckle-noise-reduced phase images.

2.2 Sub-pixel correlation technique

Knowing geometry of the ruptured fault and coseismic ground deformations, as well as seismological records, have high level of importance in the investigation of seismic rupture mechanics. Such information can be obtained from different conventional and advanced techniques such as InSAR.

As mentioned in § 2.1 , InSAR allows mapping ground displacement projected along the satellite LOS direction. But deriving complete deformation vector field, in three dimensional space, is still theoretically possible having at least three independent look directions as demonstrated by Fialko et al., 2001.

Due to the orbit inclination of current SAR satellites (§ 2.1.4), precision of InSAR is poor in north-south direction. Also, large deformation gradients (e.g. fault ruptures) is a barrier for phase identification and unwrapping, and it can not be measured directly from InSAR technique (Sarti et al., 2006).

Sub-pixel Correlation Technique (SCT) is applied in turn, on a pair of remotely sensed data set (either SAR or optical images) bracketing the seismic event and allows measuring such a gradients both in slant range and in azimuth (Leprince et al., 2007b). This technique is a complementary to the well-established InSAR technique which is sensitive to deformation in the

satellite LOS direction. By this technique, coseismic ground displacements can be retrieved from pre- and post-earthquake images.

2.2.1 Applications of SCT in earth sciences

SCT has been used by various researchers to measure earth surface changes from optical satellite images including horizontal deformations caused by earthquake (e.g. van Puymbroeck et al., 2000; Dominguez et al., 2006), surface motion of mountain glaciers (e.g. Berthier et al., 2005) and land slides (e.g. Delacourt et al., 2004, which applied SCT on aerial photographs and a pair of Quick Bird satellite images). Crippen and Blom, 1991, have addressed some other applications of the technique such as sand dune migration and coastal sediment transport.

SCT provides also displacements near the fault trace, where usually no InSAR data is available due to decorrelation (Jonsson et al., 2002), complex surface ruptures and cracks, or when the fringe rate exceeds the limit of one pixel per fringe (Avouac et al., 2006).

Distribution of deformation across a fault zone and its variation along strike, which is important to understand the seismic process and assessment of near-fault damages, might be estimated better from SCT using optical image correlation rather than InSAR (Avouac et al., 2006). Not only SCT can be applied on optical images, but also on SAR images (Crippen and Blom, 1991; Sarti et al., 2006). Michel et al., 1999, have applied this technique on ERS SAR amplitude images for the Landers test case. Although they showed less accuracy, this technique is more robust than SAR interferometry and provides complementary information, since interferograms are only sensitive to the displacement in the satellite LOS direction and then partially in range.

Sarti et al., 2006, have used SCT based on maximization of coherence for a SAR pair in interferometric condition, using complex nature of the data. They showed that in the case of high coherency, near field information obtained by this technique is useful to constrain geophysical models.

Although the main purpose of this technique in earth sciences is aimed at seismo-tectonics, the concept can be applied in any other types of change detection applications. In other words, applications of SCT are not limited to geosciences (solid earth, oceans, atmosphere, ...) and the technique has been used in other disciplines to find change pattern between two images taken before and after a changing phenomenon, e.g. medical imaging, fluid dynamics experiments, computer vision and pattern recognition.

According to different applications of this concept, it has been named with different terms in literature, such as Image Registration, Image Correlation, SAR Image Correlation, Range/ Azimuth Offsets, Imageodesy, Satellite Radar Feature Tracking (SRFT), Feature Tracking (in fluid dynamics, Moroni and Cenedese, 2005), Pixel Tracking (in web statistics), Speckle Tracking (in medicine and ultra-sound), Intensity Tracking (in spectroscopy and computer science), Offset Tracking, Coherence tracking (also known as fringe visibility in Strozzi et al., 2001), Pixel Offsets, Phase correlation method (refers to Fourier method of Schaum and McHugh, 1991), Particle Image Velocimetry (Adrian, 1991) and Digital Image Correlation (DIC) in full-field displacement and strain measurements in experimental Mechanics (Bing et al., 2006).

2.2.2 Comparing SCT with InSAR

Although SCT and InSAR have complementary roles, they have their own advantages and disadvantages. Briefly, InSAR:

1. has a lower detection threshold.
2. supports a greater horizontal spacing.
3. might work in areas where, there are not any optical features to track.
4. is more sensitive to vertical motions rather than horizontal.
5. can be affected by ionosphere/troposphere errors.

On the contrary, SCT:

1. works in areas that InSAR phase is decorrelated (because of too much deformation or change in surface scattering properties).
2. does not have unwrapping error.
3. measures deformations in two dimensional (instead of one dimensional measurements of InSAR projected in the satellite LOS direction).

2.2.3 SCT algorithms

In SCT algorithms, the offset or displacement between location of two co-registered and corresponding pixels is measured from two remotely sensed images taken in different dates, and is usually expressed in the form of a vector field. While the magnitude of displacement is proportional to length of the vectors, the direction is indicated by the vectors orientation.

Different mathematical algorithms and procedures have been developed to accomplish this technique such as:

1. Imageodesy using normalized cross-correlation
2. Fourier analysis
3. Wavelet analysis
4. Co-registration of optically sensed images and correlation

The image geodesy or 'Imageodesy' term was first proposed by Crippen and Blom, 1991, and the technique successfully used for measuring the sub-resolution movement of barchan sand dunes in an area, on the west of the Superstition Hills, Imperial County, California. This algorithm is based on the statistical concept of normal distribution. If measurements have errors that are random, their probability distribution is symmetric and bell-shaped, with a peak at the true value. If number of measurements increases, then the shape of the normal distribution can be defined sufficiently well and the peak is determined accurately. Thus, the probability of accuracy of the statistical determination (at any given level of precision) is improved with the number of measurements (Crippen and Blom, 1991). In this technique, surface displacement is determined at sub-pixel accuracy level through Normalized Cross Correlation (NCC) and phase correlation. NCC is also known as statistical correlation.

Fourier analysis, has been used by van Puymbroeck et al., 2000, to map ground displacements induced by earthquakes. In this algorithm, offsets caused by stereoscopic effect and roll, pitch and yaw of satellite and detector artefacts, are estimated and compensated. Images are then resampled in a cartographic projection with a low-bias interpolator and a sub-pixel correlator in the Fourier domain and provides two-dimensional offset maps with independent measurements (van Puymbroeck et al., 2000). Fourier methods are also known as frequential correlation.

NCC and Fourier method have their own advantages (Brown, 1992). According to Leprince et al., 2007a, while NCC methods are more robust for noisy data sets, better results are achieved

using Fourier methods. At the same time as NCC fits better for images with white noise, Fourier methods are good for images with frequency dependent noise (e.g. low frequency).

NCC method requires similar images and sensors, and under variable lighting and atmospheric conditions favours Fourier methods. NCC is good only for images misaligned by small rigid or affine transformation. In other words, images have to be co-registered first for applying Fourier methods.

Pritchard, 2009, has found that the NCC method can usually match the precision of the Fourier method when the data has been high-pass filtered (Scambos et al., 1992) before applying SCT.

Wavelet concept also has been applied in change detection field using boxcar functions to approximate pixel boundaries and then can give better approximation of sub-pixel displacement (Strang and Nguyen, 1997). However, application of this technique does define fault rupture well and does not give results in complex geological settings.

Despite the advantages, SCT is suffering from some limitations, mostly due to uncertainties on the imaging systems and on the platform attitude (Leprince et al., 2007b). In addition, precise image coregistration is a prerequisite in SCT and usually this critical step is a major source of limitation (Townshend et al., 1992; Bryant et al., 2003).

Leprince et al., 2007a, have described a procedure to accurately measure ground deformation from optical satellite images. The, so-called 'Co-registration of Optically Sensed Images and Correlation (COSI-Corr)' procedure allows for a precise correction of most of these limitations and for accurate estimation of sub-pixel displacements of an image pair, and has been implemented in a software package. This new algorithm has been used and tested by Leprince et al., 2007b, to analyse the M_w 7.6 Kashmir and M_w 7.3 Landers earthquakes, using ASTER and areal images, respectively. In the analysis of the conducted test cases, the coregistration accuracy was on the order of 1/50 of the image nominal resolution, and georeferencing precision was similar to the used DEM.

COSI-corr utilizes NCC and another algorithm based on Fourier Shift Theorem (FST) and computes the offsets in the frequency domain (Pritchard, 2009).

2.3 Inversion problem

Inverse problem is a procedure to find values of some model parameters from observed data (Wikipedia, 2009) and can be formulated as follows:

$$Data \rightarrow Model\ Parameters \quad (17)$$

In other words, "The inverse problem consists of using the actual result of some measurements to infer the values of the parameters that characterize the system" (Tarantola, 2005).

The transformation from data to model parameters, is a result of the interaction of a physical system such as earth, atmosphere and the gravity field (Wikipedia, 2009). Application of inverse problem in geophysics can answer questions such as how fault geometry and slip distribution are inferred from surface deformation measurements. Such a problem is highly non-linear with no-unique answer (Peyret et al., 2007).

Okada, 1985, has presented a complete suite of closed analytical expressions for the surface displacements, strains, and tilts due to inclined shear and tensile faults in a half-space for both

point and finite rectangular sources. Okada's expressions represent powerful tools, not only for the analysis of static field changes associated with earthquake occurrence, but also for the modelling of deformation fields arising from fluid-driven crack sources.

Okada's model, has been a basis for inversion problem solutions and many researchers have made assumption of a shear dislocation in a uniform elastic earth model, using Okada analytical solution for deformation (e.g. Pedersen et al., 2003; Nishimura et al., 2003; Nunnari et al., 2005; Peyret et al., 2008b).

Since inversion is strongly dependent on starting solution, overall earthquake motion (geometry and overall slip) can be estimated using a stochastic approach. Sambridge, 1999a, has introduced a new derivative-free search method for finding models of acceptable data fit in a multi-dimensional parameter space. This new search algorithm makes use of the geometrical constructs known as Voronoi cells to control the search in parameter space. These are nearest neighbour regions defined under a suitable distance norm.

The Sambridge technique, which is called Neighbourhood Algorithm (NA), determines an optimal model according to standard misfit function between predicted and observed surface displacement and also allows for an estimation of a-posteriori probability function for all the parameters of the model (Peyret et al., 2007).

NA requires just two tuning parameters: the number of new generated models for each step of the process, and the number of cells to be resampled. Depending on the value of the later parameter, the procedure is essentially exploratory, means searches for a global minimum, or it is localized, means efficient as an optimizer, but possibly detects a secondary minima (Peyret et al., 2007).

A standard linear least square inversion method is then applied to find the slip distribution on the fault plane fixed by the NA. The Least Square (LS) algorithm minimizes misfit to measured coseismic displacements weighted by measurements errors, while preserving smoothness of the slip distribution. By this method, the question of 'how precisely slip distribution models are inverted from surface displacement data can be spatially resolved', is answered (Peyret et al., 2007).

The NA and LS inversion methods have been explained in different sources (e.g. Sambridge, 1999a; Sambridge, 1999b; Peyret et al., 2007; Du et al., 1992) in details. However, a concise summary of these two algorithms, which is necessary for applying inversion method and interpretation of results, is stated here from Peyret et al., 2007, to avoid redundancy.

2.3.1 Neighbourhood algorithm

The NA is a direct search procedure in the models space with only forward modelling calculation just as genetic algorithms or simulated annealing (Sambridge, 1999a), and is particularly well-suited to highly non-linear inversion problems.

The objective is to find a set of dislocation models at depth, that preferentially sample the good data-fitting regions of models space, rather than seeking a single optimal model. So, models space is first defined, by determining the set of parameters to estimate and their respective prior boundaries.

Forward modelling is used, and an objective function that measures the discrepancy between observed data and theoretical predictions is estimated for each sample in the models space. The following Chi-square misfit function is used:

$$\chi_v^2(m) = \frac{1}{v} \sum_{i=1}^{\text{data sets}} \mathbf{w}_i (\mathbf{d}_i - \mathbf{g}_i(m))^T \mathbf{C}_i^{-1} (\mathbf{d}_i - \mathbf{g}_i(m)) \quad (18)$$

For a given model m , the predicted surface deformation projected along each axis of observation $\mathbf{g}_i(m)$ is compared to the corresponding measured data \mathbf{d}_i . In Equation 18, v is the degrees of freedom (number of data minus the number of independently constrained model parameters) and since the algorithm just requires models to be assessed for their relative fit to the data, its value is only used ultimately for determining an absolute measure of data fit. \mathbf{C}_i are the data covariance matrices constructed from the corresponding estimation of standard deviation of the noise. The weights \mathbf{w}_i are chosen in such a way that the misfit is approximately equilibrated among the different data sets used. Therefore, it is expected that the inversion will not be dominated by a part of the data. This weighting should therefore reflect the relative confidence on these data. In practice, different weights are used for increasing the prevalence of one data set over the others, in order to estimate its relative influence on the optimal derived model.

2.3.2 Linear least square inversion

While the NA provides the main characteristics of the dislocation, the geometry of the fault and the elastic parameter are retained. Since the NA was limited to a fault plane, more complexity can be introduced to this first-order geometry by defining the fault as a set of as many rectangular patches as desired. So, in this secondary inversion stage, the slip distribution is estimated over a fixed geometry.

A standard linear least-square inversion technique under constraints (known as Penalty Function Technique) is implemented. A slip vector (for model m) should be found in a way that minimizes the following penalty function:

$$Pb: \text{minimize } \mu_{sm} \|\nabla\|^2 + \sum_{i=1}^{\text{data sets}} \mu_i \|\mathbf{W}_i \mathbf{d}_i - \mathbf{W}_i \mathbf{P}_i \mathbf{G}_i \mathbf{m}\|^2 \quad (19)$$

where, \mathbf{G}_i are matrices of Okada parameters (the data kernels) which relates slip on individual fault patches to surface three dimensional motion at all surface observation points, \mathbf{P}_i are the projection matrices onto the corresponding direction of measurement (it is vertical for leveling, horizontal for offsets, and the satellite LOS direction for InSAR) and \mathbf{W}_i are weighting matrices that state the confidence for each observation.

Furthermore, the dislocation model at depth is expected to be smooth to some degree. Such a constraint is important in restoring a stable and physically meaningful solution. The roughness of the estimated slip distribution is expressed by a finite-difference approximation of the Laplacian (∇). The extent to which smoothness is enforced at the expense of fit to surface displacements, is controlled by changing the smoothing parameter μ_{sm} . A value which suppresses spurious structure in the slip distribution while not smoothing out salient features, is retained.

Comparatively for the NA inversion, the influence of each data set on the derived model is controlled by the associated weight matrix in the penalty function. An a-posteriori optimal choice of these parameters can be made by plotting models on a graph representing their misfits

relatively to different data sets (known as Tikhonov plots). The model for which the misfit to all data sets looks the most acceptable, is retained. Then, the slip-distribution model at depth can be estimated by:

$$\mathbf{m} = \left[\mu_{sm} \nabla \nabla^T + \sum_{i=1}^{data\ sets} \mu_i (\mathbf{P}_i \mathbf{G}_i)^T \mathbf{C}_i^{-1} (\mathbf{P}_i \mathbf{G}_i) \right]^{-1} \times \left[\sum_{i=1}^{data\ sets} \mu_i (\mathbf{P}_i \mathbf{G}_i)^T \mathbf{C}_i^{-1} \mathbf{d}_i \right] \quad (20)$$

This inversion procedure allows for the determination of the a-posteriori model covariance \mathbf{C} :

$$\mathbf{C} = \left[\mu_{sm} \nabla \nabla^T + \sum_{i=1}^{data\ sets} \mu_i (\mathbf{P}_i \mathbf{G}_i)^T \mathbf{C}_i^{-1} (\mathbf{P}_i \mathbf{G}_i) \right]^{-1} \quad (21)$$

and a model resolution kernel \mathbf{R} :

$$\mathbf{R} = \mathbf{C} \cdot \left[\sum_{i=1}^{data\ sets} \mu_i (\mathbf{P}_i \mathbf{G}_i)^T \mathbf{C}_i^{-1} (\mathbf{P}_i \mathbf{G}_i) \right]^{-1} \quad (22)$$

which implies how well the slip vector is resolved on each fault.

Chapter 3

The Earth doth like a snake renew
Her winter weeds outworn
Shelley, Hellas

3 The study area

L'Aquila is a historical city in centre of Italy located at (42.35°N, 13.40°E) and is both the capital city of the L'Aquila province and the Abruzzi region (L'Aquila, 2009a). L'Aquila has been established in 1254 AD (D'Addezio et. al., 1995) on top of a hill in the wide valley of the Aterno river. The city is surrounded by the highest summits of Apennines mountain range (L'Aquila, 2009b), about 93 km to the north-east of Rome, the Italy capital (Figure 4).

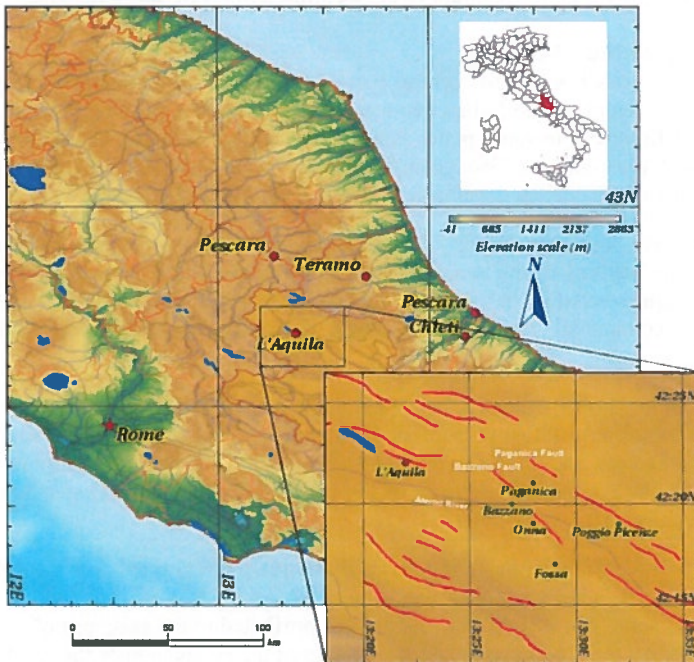


Figure 4: The study area

The area is one of the most seismically active areas, and its history has been ingrained by earthquakes. Several historical and instrumental earthquakes of different magnitudes have struck L'Aquila, during the past centuries (§ 3.2.3).

Since the end of December 2008, the L'Aquila basin experienced a long seismic sequence (Anzidei et al., 2009). On Monday April 6th, 2009 at 01:32:39 UTC, this seismic sequence culminated and the city of L'Aquila and the surrounding area was shocked by an earthquake of M_w 6.3. According to USGS, 2009a, the earthquake occurred at the coordinate of (42.334°N, 13.334°E) and at depth of 8.8 km, located in the central region of Abruzzi province.

The main shock inflicted serious damage to the city and other surrounding towns and villages including Paganica, Castelnouva and Onna. Cultural heritage in L'Aquila including masonry buildings were collapsed or seriously damaged. At least 294 people died, mostly in collapsed buildings (Mediaset, 2009), about 1500 people injured and tens of thousands were left homeless (BBC World News, 2009a). The high number of casualties made it the deadliest earthquake in Italy since Irpinia earthquake in 1980. The strongest after-shock M_w 7.3 on April 7th, 2009, at 17:47 UTC, caused even further damage (BBC World News, 2009b).

3.1 Geological and tectonic settings

After the earthquake, a number of exploring teams were activated in the affected area. Among them, Istituto Nazionale di Geofisica e Vulcanologia¹ (INGV) mobilised a group of geologists (EMERGEO team) to investigate evidences of the surface rupture and other effects. The results have been published in EMERGEO Team, 2009. The Geo-engineering Extreme Events Reconnaissance (GEER) team was another group of international individuals comprising of high level of expertises. A technical report presenting results of GEER team studies (GEER, 2009) has been published in the GEER website. The second chapter of this report was used concisely as a reference for describing the geological and tectonic settings of the study area.

3.1.1 Geodynamic evolution

The study area is located within the central part of the Apennines chain mountains which traverses most of the length of the Italian peninsula and is the result of the convergence between the African and European tectonic plates and the subsequent collision of the two continental margins. Figure 5 illustrates the Geodynamic process that began in the Neogene age (about 23 MYBP) and was responsible for the closing of the Mesozoic Tethys Ocean.

The compressive phase significantly deformed the extensive layers of marine deposits accumulated along the margins of the African Plate, uplifting them into a mountain chain. During time, orogenic thrusts acted in an asynchronous manner along the Apennines chain, deforming this sector of the continental crust from the Miocene epoch to the Upper Pliocene sub-epoch (24 to 3.6 MYBP).

The Geodynamic model which is most often cited and used to describe recently observable phenomena, is based on a thrust belt-foredeep-foreland system progressively migrating away from the Tyrrhenian sea and towards the Adriatic sea flank. This system describes a transition from continental compression in the front of the chain (Adriatic side) to extension behind the chain (Tyrrhenian sector).

The thrust belt-foredeep-foreland system's progressive migration towards the Adriatic flank would have occurred in response to a mechanism of sinking with the flexural retreat of the Apulian foreland plate. The flexural retreat could be attributed to the existence of movements in the upper mantle that have a direction contrary to that of the subduction of the Apulian plate towards the Tyrrhenian flank (Doglioni, 1990; Doglioni, 1991).

1 The national institute of geophysics and volcanology of Italy

Finally, at the beginning of the Messinian-Tortonian age (11.6 MYBP), the area experienced a process of crustal thinning accompanied by the oceanization of the Tyrrhenian Sea (retro-arc basin). Since the lower Pleistocene (1.8 MYBP), these extensional movements, which in the peri-Tyrrhenian area cause the development of Tuscany-Lazio-Campania volcanism, have been progressively migrating towards the Adriatic sectors, to the point that they have affected the Apennines chain watershed. The portion of the chain between the watershed and the Adriatic area, however, would have undergone a process of gravitational settling and collapses due to isostatic instability, with the consequent formation of several intra-Apennines basins, including the L'Aquila basin (Ghisetti and Vezzani, 2000).



Figure 5: Geodynamic model for central Mediterranean (Devoti et al, 2008)

The deformations associated with crustal thinning and the gravitational collapse, are primarily accommodated by normal faults formed in part by reactivating pre-existing thrusts associated with the emplacement of the Apennines tectonic slices, making these structures important pre-, syn- and late-orogenic normal features that define the plano-altimetric configuration (basin and range). This pattern displays alternating ridges (Simbruini-Ernici, Velino-Sirente, Gran Sasso, Maiella e Morrone, etc.) and depressions under tectonic control (Valle del Sacco, Val Roveto, Piana del Fucino, Valle dell'Aterno, Conca dell'Aquila, Piana di Sulmona, etc.) as illustrated in Figure 71 in Appendix A (Cavinato and Celles, 1999).

3.1.2 Geological settings

The central part of the Apennines chain consists of deposits that were formed on the continental crust of the African plate in different paleogeographic domains. In general terms, two great Meso-Cenozoic depositional systems are distinguishable. The first one is characterized by Mesozoic carbonate platforms (limestones and dolomites) evolving towards carbonate slope and basin environments (calcarenes and marls) and was subject to active deposition until the mid-Miocene (16.5 MYBP). The second one consists of impressive foredeep silicoclastic deposits (clays and sandstones) datable to the Upper Miocene-Pliocene interval (11 to 5 MYBP).

The emergent chain then underwent an intense erosive Plio-Pleistocene phase (5 to 1.7 MYBP). The sedimentary erosive-depositional cycles produced slope deposits and vast alluvial and lacustrine deposits that filled the intra-Apennines basins. The Pleistocene glacial cycles interacted with the tectonic deformations, through fluctuations in fluvial base level and variations of the predominant morphodynamic regime.

Elongation in the north-west to south-east direction (parallel to many of the active normal faults) is notable in these intra-Apennines basins, which include the localities (among them the L'Aquila city) that were affected by the earthquake of April 6th, 2009. In the inset of Figure 4, red lines show the active faults of the area.

The area affected by the the main shock, roughly corresponds to the valleys of the Aterno River, its right tributary Raio Creek and the plateau extending to the west of the Aterno Valley. The bedrock of the area is comprised of limestone formations, deposited from the Jurassic to the Miocene age, that largely outcrop along the valley flanks and on the ridges located within the Aterno Valley. These limestones vary in texture from micritic to bioclastic and calcareous sandstones are also common. Several formations are associated with thick chert bands and/ or layers. Glauconite rich layers are found in several of the Cretaceous formations. Bedding thickness ranges from thinly bedded to very thickly bedded massive limestones. The pelagic content of the limestone varies and several formations vary between marly limestone and calcareous marls, which tend to be thinly bedded. Calcareous conglomerates form the thickest and most competent layers within these formations. Locally the substratum consists of Miocene sandstones with marly intercalations. These outcropping formations are composed primarily of marls and clays. Marl-dominated formations also tend to be thickly bedded, within these formations the clay content can vary resulting in more clayey marls. Marly limestones are also present in these formations together with chert and glauconite.

In the central inhabited zone of L'Aquila, there are vast deposits associated with Quaternary paleo-landslides. These deposits consist of Pleistocene heterometric breccias with varying degrees of cementation, known as 'Megabreccias', at times of noteworthy dimensions (up to several cubic meters), comprised of primarily calcareous elements immersed in sandy silty matrices.

The Aterno Valley is partly filled by Pleistocene lacustrine deposits formed by a complex sequence of pelitic and coarse grained units, with frequent lateral variations, overlying the bedrock. On the left side of the Aterno river drainage basin (drainage from north-west to south-east), old breccias with large blocks are interposed between the bedrock and the lacustrine sequence (Valle Valiano formation).

The older (bottom) unit of the lacustrine sequence is the S. Nicandro formation. It consists of silts locally characterized by a significant clay fraction. On the left side of the drainage basin, alternations of silts with breccia layers are locally found at the base of the lacustrine sequence. More recent (shallower) components of the lacustrine sequence are formed by coarse-grained units, often cemented, ranging from sands with gravels to breccias with large blocks, which can present finer intercalations (silts, fresh or weathered pyroclastites, paleosols). The units differ by clast shape, abundance of finer intercalations and overall degree of cementation.

The valley bottom is topped by Holocene alluvial deposits whereas the foot of the valley flanks and of the ridges located within the valley are covered by talus debris and locally by large debris alluvial fans.

3.1.3 Tectonic setting

The Quaternary deposits of the L'Aquila area were deposited in morphological depressions inside the uplifted and emergent chain. These sedimentary basins are primarily delimited by high-angle (70°) normal faults with an Apennines trend that vertically break up, at different elevations, the orogenic structure, thereby forming a horst and graben structure. The normal fault system has its origins in a Quaternary phase (1.8 MYBP). In general, the intra-chain basins are delimited by master faults and synthetic faults (i.e., a type of minor faults whose strike and sense of displacement is similar to their associated major fault) on the eastern sides of the depressions and by antithetic faults on the western sides.

Figure 6 shows a geologic cross-section passes from south-west to north-east through the Aterno river valley, L'Aquila basin and inhabited centre of Onna. The right side of the cross-section shows an intra-Apennines basin along side an area of the chain that was overlain during the compressive phases by Apennines orogeny. The cross-section gives an idea of the tectonic structure of this sector.

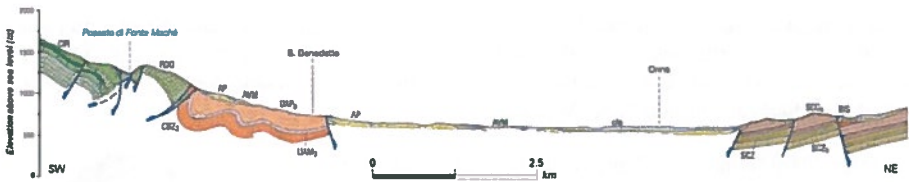


Figure 6: South-west to north-east geological cross-section, passing the L'Aquila basin (geologic map of Italy at scale 1:50,000)

In the area south-east of L'Aquila, it is possible to see morphological limestone ridges outcropping with monoclinical attitude. Some ridges are located in the centre of the old Quaternary lacustrine basin. These ridges are the surface evidence of uplifted structures (horst wedges) surrounded by depressed areas (grabens) filled with Quaternary deposits.

The extensional system, comprised of normal faults (master faults, synthetic and antithetic faults) present in the area, is active, as demonstrated by this earthquake and the regional geomorphology. Extension is also demonstrated by the normal fault focal mechanism of the present earthquake, as it is described in § 3.2. The activity of the tectonic structures, with larger movements on the eastern edges of the basins, are also evidenced by the presence of important Quaternary alluvial fans on the north-east side of depressions. With their movement, the normal faults have in fact produced a rejuvenation of the relief in the north-east areas, resulting in the increased effectiveness of the erosive processes and the deposition of coarse material in the valley zones in the south-west areas.

Figure 72 in Appendix A, shows active faults of the L'Aquila area. These are normal faults of variable length that predominantly strike in north-west to south-east direction. In this figure, features are oriented towards the hanging-wall and the stars indicate the locations of some epicentres of recent seismic sequence with $M_w > 4.0$ (Galadini and Galli, 2000; Galadini and Messina, 2001; Boncio et al., 2004). In south-east of L'Aquila, the active faults have a strongly rectilinear trend dipping, either towards the south-west or the north-east.

3.2 Seismological aspects

3.2.1 The main shock

The main shock of the seismic sequence happened on April 6th, 2009 at 01:32:39 UTC and recorded by the Rete Sismometrica Nazionale Centralizzata¹ (RSNC), operated by the Centro Nazionale Terremoti² (CNT) of the INGV. Table 6 Shows the calculated parameters for the main shock by INGV-S4 project website.

Date	Time (UTC)	Lat. (°N)	Long. (°E)	Depth (km)	M_w
2009/04/06	01:32:39	42.334	13.334	8.8	6.3

Table 6: The main shock parameters (INGV-S4 project website)

The main shock was recorded also by other seismological centres, even though the reported parameters by different centres are slightly different. Table 31 in Appendix B, shows reported parameters by European-Mediterranean Seismological Centre (EMSC, 2009).

The focal mechanism published by INGV (Table 7) shows the event took place along a normal fault trending north-west to south-east (strike 147°) with dip towards SW<50° (low-angle fault). The fault demonstrates the same direction as many of the major tectonic structures visible on the surface (see Figure 72 in Appendix A).


Date: 2009/04/06	Time: 1:32:47.2 UTC	M_w 6.3			 Event ID: 040609A
Centroid location: (42.32°N, 13.32°E), Depth: 12 km (fixed)					
Best double couple: ($M_0 = 3.7 \times 10^{25}$ ergs)					
	NP	Strike (°)	Dip (°)	Slip (°)	
	1	147	43	-88	
	2	324	47	-92	

Table 7: QRCMT for the main shock (INGV-S4 project website)

3.2.2 Seismic sequence

The earthquake of April 6th, 2009 was the largest event in a seismic sequence that started a few months earlier and had its most significant fore-shock on March 30, 2009 (GEER, 2009).

Since the main shock, an active seismic sequence has occurred with events larger than 4.0. Specially, two events as large as M_w 5.6 and M_w 5.4 occurred on April 7th and 9th, respectively. Tables 8 and 9, show the focal mechanisms of these two after-shocks, published by INGV-S4 project website. Table 10 summarizes the main parameters of the two strongest after-shocks reported by INGV-S4 project website. It should be noticed that the reported parameters for the events are not the same, even in one reference.

Table 31 in Appendix B, lists all fore-shocks and after-shocks occurred since April 5th, 2009, till April 20th, 2009, with magnitude greater than 4.0 in the area between latitude of 42°N and

1 Centralized National Seismological Network

2 National Earthquake Centre

43°N and longitude of 13°E and 14°E (EMSC, 2009). Shocks with magnitude greater than 5.0 are highlighted in this table.


Date: 2009/04/07	Time: 17:47:42.8 UTC	M_w 5.6			 Event ID: 040709B
Centroid location: (42.27°N, 13.38°E), Depth: 23 km					
Best double couple: ($M_0 = 2.9 \times 10^{24}$ ergs)					
NP	Strike (°)	Dip (°)	Slip (°)		
1	336	50	-55		
2	109	51	-124		

Table 8: QRCMT for the after-shock of April 7th (INGV-S4 project website)


Date: 2009/04/09	Time: 00:53:5.3 UTC	M_w 5.4			 Event ID: 040909A
Centroid location: (42.42°N, 13.25°E), Depth: 12 km (fixed)					
Best double couple: ($M_0 = 1.6 \times 10^{24}$ ergs)					
NP	Strike (°)	Dip (°)	Slip (°)		
1	148	40	-90		
2	328	50	-90		

Table 9: QRCMT for the after-shock of April 9th (INGV-S4 project website)

Date	Time (UTC)	Lat. (°N)	Long. (°E)	Depth (km)	M_w
2009/04/07	17:47:37	42.275	13.464	15.1	5.6
2009/04/09	00:52:59	42.484	13.343	15.4	5.4

Table 10: Parameters of the two significant after-shocks (INGV-S4 project website)

The location of instruments and the sequence of the after-shocks, shown in Figure 73 in Appendix A (updated on August 25, 2009), clearly identify two principal areas of crustal rupture: the main area in which the main shock of April 6th occurred, and a second area associated with another tectonic structure, probably of smaller dimensions, on which the earthquake of April 9th occurred. The latter structure even demonstrates that it had an extensional movement along a plane oriented in the Apennines direction and dipping towards the south-west by about 50° (Table 9). The focal mechanism for the after-shock of April 7th (Table 8), shows a component of oblique movement occurred at a deeper depth than the other two events.

3.2.3 Recent and historical seismicity

The information contained in the historical documents make it possible to compile a seismic history for each Italian region, in the form of a graph with years on the abscissa and macro seismic intensity (MCS) on the ordinate. Figure 7 shows macro seismic historical events of L'Aquila (DBMI04, 2009).

The affected area by the recent earthquake, lies between two areas with higher levels of activity: Umbria-Marche to the north-west, struck by the 1997 seismic sequence (Amato et al., 1998) and Lazio-Molise area to the south-east, shocked by the 2002 seismic sequence (Giuliani et al., 2007). This area have had low seismic activity between 1980 to 2008¹.

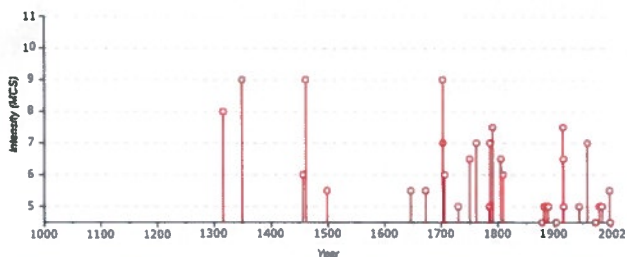


Figure 7: Seismic history of L'Aquila area (DBMI04, 2009)

The high seismic risk of the L'Aquila area has been known for some time, due to historical seismic studies that have put in evidence numerous important earthquakes (see Figure 74 in Appendix A) that affected the central Apennines (GEER, 2009). The most significant earthquakes in the area occurred on the years 1315 ($M_w > 6.7$), 1349 ($M_w > 6.5$), 1461 ($M_w > 6.5$), 1703 ($M_w > 6.7$) and 1915 ($M_w > 7.0$) (DBMI04, 2009). Other major historical earthquakes which have happened on 1498, 1646, 1750, 1786, 1791, 1809, 1874, 1908 and 1911 (two times) (Gruppo di lavoro CPTI, 2004), had lower magnitude.

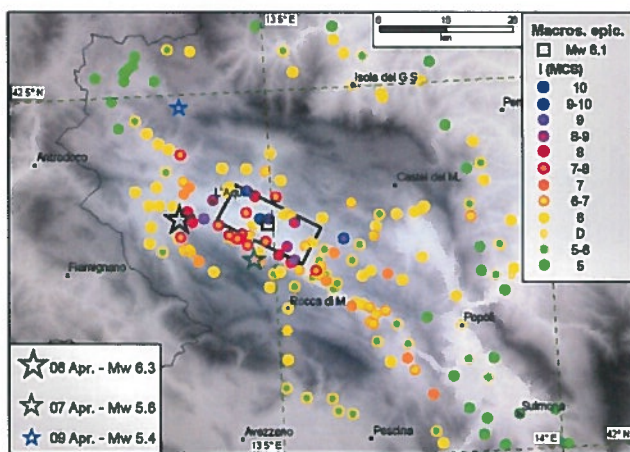


Figure 8: Results of macro seismic survey conducted by the QUEST (QUEST, 2009)

Among the historical earthquakes, the event of the year 1461, produced macro seismic effects in the same area of maximum intensity as April 6th earthquake. The area of maximum intensity was located between the city of L'Aquila and the inhabited centre of Paganica, passing

1 According to Gruppo di lavoro CPTI, 2004, the last major earthquake in this area happened in 1980 in Popoli, about 39 km to the south-east of L'Aquila.

through Onna. This event has spatial and parametric characteristics similar to those of the earthquake of April 6th, since it has a maximum intensity equal to X MCS and an estimated M_W 6.5, close to magnitude of this event (M_W 6.3).

A few hours after the main shock of the April 6th earthquake, the Quick Earthquake Survey Team (QUEST), was mobilised to the affected area and compiled a macro seismic survey from the effects of the earthquake on the built-up and inhabited areas in more than 180 localities of the L'Aquila, Pescara, Teramo and Rieti provinces (QUEST, 2009). Figure 8 shows QUEST survey results and the relevant report has been published in the QUEST website.

The map shows an asymmetric distribution of damage with respect to the earthquake's epicentre. It is observed that to the north and west of the epicentre (the black star in Figure 8) the damage is limited, and the macro seismic intensities show values no higher than VI MCS. Conversely, in the south-east area of L'Aquila, the intensities reach values of X MCS, with an area of intensity and damage that elongates to a significant distance from the epicentre. In the south-east area of L'Aquila, intensities of VI MCS are registered at distances much greater than those reached by the same level of intensity in the area in the north-west of L'Aquila.

Chapter 4

Prospero: Deeper than did ever plummet sound,
I will drown my book.
Shakespeare, The Tempest

4 Methods and materials

Generalized schematic diagram of the overall methods is shown in Figure 9.

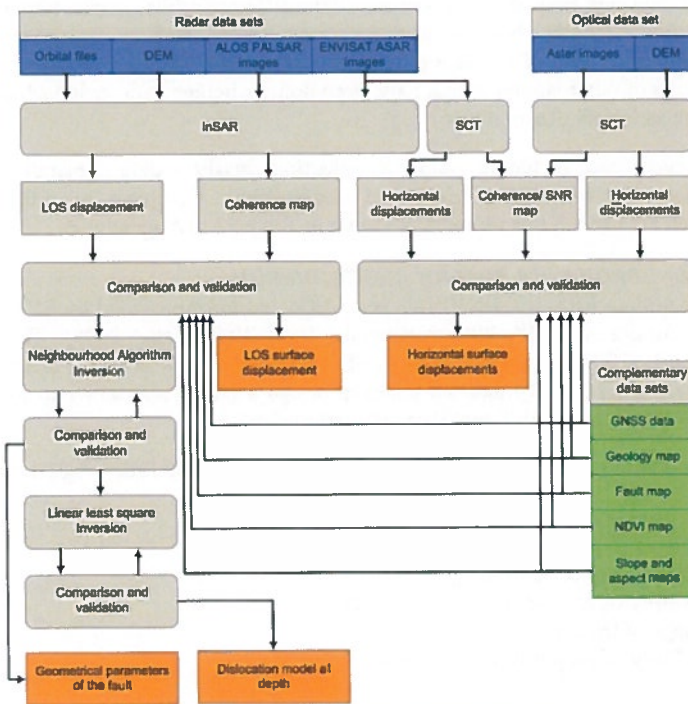


Figure 9: Overall methods and procedures

The work flow is mainly divided into three sections, namely: InSAR, SCT and Inversion problem, and each section is elaborated in the following sections.

4.1 InSAR

Theory and geophysical applications of SAR interferometry explained in §2.1. This is the technique which is used in this research for measuring land deformations along the satellite LOS

direction in L'Aquila area, caused by the April 6th earthquake. To do this, a set of main data sets (Radar images), auxiliary data sets (such as a DEM, orbital parameters of the SAR satellites and so on) and a proper software are necessary.

Interferometric and coseismic ENVISAT ASAR and ALOS PALSAR image pairs, with minimum temporal and proper spatial baselines are selected in both ascending and descending passes, and then orbit phase signature is removed from them using precise orbit files.

Interferometry is done using the reduced complex Radar images in full resolution. Interferograms are unwrapped to make displacement map in the satellite LOS direction, and then are georeferenced using the available DEM (the DEM is also used in other steps of interferometry; see § 4.1.3).

Coherence map is another output of SAR interferometry which is used for quality assessment of the interferograms. Coherence map is also used in Inversion problem to retain significant pixels and assign a proper weight to them.

Displacement maps of different pairs and different sensors are compared with themselves, and similarities and discrepancies are discussed as well as difficulties and uncertainties. Because different data sets from different sensors (with different orbits, tracks, temporal and spatial baselines, wave lengths, band widths, incidence angles, and so on) are processed and compared, it implies a kind of validation by default. However, results from this study is compared with results of other studies which have been done, whether with same technique or other techniques such as GNSS observations.

Details of every part, including main data selection, auxiliary data preparation and the algorithms of processing software, are explained here in details. Complete list of the applications and codes which are used in this research is shown in Table 32 in Appendix B.

4.1.1 Radar image data sets for interferometry

SAR images including ERS-1/2, ENVISAT and ALOS has been provided by ESA as a data set package for L'Aquila April 6th, 2009 earthquake (Italy Earthquake, 2009). This data set is mainly composed of SAR Level 0 as well as SLC products and is available from ESA virtual archive website. This extensive data set package brings a good opportunity to investigate the study area with integration of different data sets and methods.

Proper data sets were chosen from ESA package considering the following criteria:

1. Image band and wave length
2. Stability of sensors and satellites
3. Availability and price of images
4. Availability of precise orbital parameters
5. Coverage of the area
6. Availability of proper InSAR software

4.1.1.1 ERS-1/2

Life time of ERS-1 was expired on March 2000 (see §2.1.4.1) and no more SAR image has been acquired by this satellite after this date. However, before this date ERS-1 was operating in a good condition and the acquired SAR images can be used for integration with other satellite images for long time period study.

ERS-2 is operating in YCM-R status now (see §2.1.4.2) and refer to §2.1.4.3, SAR images acquired by this satellite, after February 2000, are not suitable for interferometry. In spite of this fact, many pairs of ERS-2 SAR images were chosen in interferometric condition with minimum DC frequency change (in comparison to other pairs), but all failed in process. Table 33 in Appendix B, shows list of chosen ERS-2 SAR image pairs. The error comes up in fine culling stage in the image coregistration step, when the offset should be estimated by the software (§ 4.1.3 for InSAR software).

Doppler analysis of ERS-2 SAR images shows high DC variation between two scenes. Figure 10, illustrates DC frequency variation between two images of a sample ERS-2 interferometric pair acquired on June 8th, 2003 (orbit 42518) and April 12th, 2009 (orbit 73079) in descending pass. In this figure, while by increasing number of sampled lines, DC for one image is increasing, it is fluctuating for the other one at first sampled lines, between positive and negative Pulse Repetition Frequency (PRF) values, and then starts to increase. Other ERS-2 image pairs show same instability in DC. The instability of DC in ERS-2 images is seen after the gyroscope failure problem, make them improper for interferometry and are rejected from this research, necessarily.

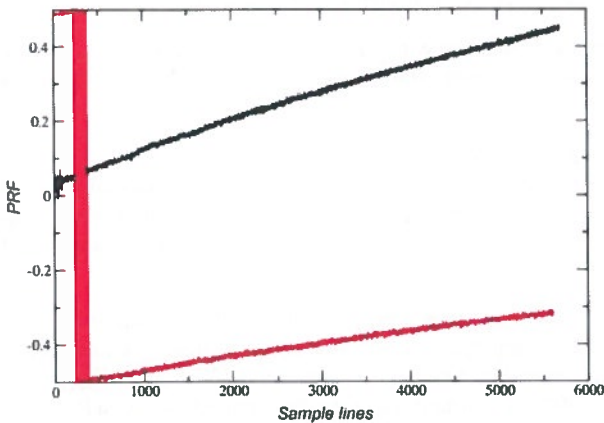


Figure 10: Comparison of DC frequency between two images of an ERS-2 interferometric pair

4.1.1.2 ENVISAT

The ENVISAT satellite works in a normal condition and acquires Radar images, properly. ENVISAT's pre- and post-seismic images of the L'Aquila area are available in raw and SLC formats in ascending and descending passes from ESA package for L'Aquila earthquake (Italy Earthquake, 2009). The images in raw format are used in this research.

Several interferometric pairs could be found among available data sets. However, just two coseismic pairs one in ascending and another in descending passes with the shortest time interval were initially selected to study the seismic event. The results cover the general objective of this research and answer the first research question to some extent, while the other part will be answered using results from SCT.

4.1.1.3 ALOS

The ALOS satellite is working in a normal condition and pre- and post-seismic images of its Radar sensor, PALSAR, are available for the study area in raw format, some of them by ESA package for L'Aquila earthquake (Italy Earthquake, 2009) and others were ordered to make two interferometric and coseismic pairs.

'ALOS_baseline' utility written by Rob Mellors and David Sandwell (available from ROI_PAC website, Contributed software page) was used for evaluation of interferometric baselines of available ALOS PALSAR images in the ESA package. The test showed that they are not suitable for making interferometric pair by themselves, because whether the pairs have very long perpendicular baselines (more than 3 km) or images are from same tracks and same orbits.

ALOS PALSAR image catalogues, e.g. Earth Observation Link of ESA (EOLi website) and Online Satellite Images Search and Order System (CROSS website) of Remote Sensing Technology Centre of Japan, were browsed to find proper coseismic and interferometric pairs in both ascending and descending passes. However, no any image of this sensor was found for the study area in descending pass. So, just two ascending pairs of ALOS PALSAR images with minimum available perpendicular baselines were chosen and processed.

The results from interferometry with ALOS PALSAR data set, will support findings of ENVISAT ASAR data set for covering the general objective and answering the third specific objective of this research.

4.1.2 Auxiliary data sets

Although auxiliary data sets including DEM, orbit files, instrumental files, precipitation data, GNSS observations and geology, active faults, vegetation, slope and aspect maps, are not necessary for interferometry, they can help to achieve the best possible accuracy and better interpretation of the results.

Among mentioned auxiliary data sets, precipitation data set and GNSS observation could not be obtained from relevant Italian organisations, even though a long email communication was done and initial agreements were signed with Centro Nazionale di Meteorologia e Climatologia Aeronautica¹ (CNMCA), Istituto Superiore per la Protezione e la Ricerca Ambientale² (ISPRA) and INGV. Other auxiliary data sets were prepared, as explained in the following text.

4.1.2.1 DEM

Topographic phase signature is removed from interferograms using a precise DEM of the study area (Hooper et al., 2004; see also §2.1.2). Such a DEM can be either generated indirectly by three pass interferometry (e.g. Graham, 1974; Massonnet and Feigl, 1998) or obtained from other sources or methods such as photogrammetry.

Before June 29, 2009, a DEM generated by Shuttle Radar Topography Mission (SRTM) was the most complete and homogeneous available DEM with highest resolution for the whole globe (Farr et al., 2007).

SRTM DEM is available in one arc sec (about 30 m spatial resolution) for United States and its territory and three arc sec (about 90 m and also one kilometre spatial resolution) globally

1 Italian National Centre for Aeronautical Meteorology and Climatology

2 Institute for Environmental Protection and Research

(USGS, 2009b), in different processing levels and formats (e.g. hgt and GeoTIFF) through different data centres (e.g. NASA, USGS, EROS, GLCF and CGIAR-CSI).

The SRTM DEM is arranged into one by one degree of latitude and longitude tiles (Berry et al., 2006). However, this is not a standard and some data centres (e.g. CGIAR) offer it in 5° by 5° tiles.

SRTM DEM is affected by shadowing or overlaying phenomena (in high mountains) and specular reflection or highlighting (for sand deserts and water bodies), which is usually led to data voids (e.g. Rees, 2000; Hall et al., 2005). The data voids are filled in some distributions of SRTM DEM, while are interpreted in the others using surrounding data. Quality of a gap filled version is better than gap interpolated one, specially when the missing data patch is big (Dowding et al., 2004).

The CGIAR consortium has released the latest gap filled version (version 4.1) of SRTM 90 m DEM (available on CGIAR consortium website) using interpolation method described by Reuter et al., 2007. This level of data, was the best available version of SRTM DEM before publishing ASTER Global DEM.

On June 29, 2009, a jointly developed Global DEM (GDEM) was released by Ministry of Economy, Trade and Industry (METI) of Japan and National Aeronautics and Space Administration (NASA) of United States. ASTER GDEM has been produced automatically as a result of processing of the entire 1.5 million scenes of ASTER archive (ASTER G-DEM, 2007). Table 11 summarizes the basic characteristics of the ASTER GDEM.

Geographical coverage	83°S to 83°N
Tile dimensions	1° by 1°
Tile size	3601 by 3601
Posting interval	1 arc sec. (about 30 m spatial resolution)
Reference system	WGS84/ EGM96 geoid
Pre-production estimated accuracy	20 m at 95% confidence interval for vertical data 30 m at 95% confidence interval for horizontal data
Format	GeoTIFF, signed 16 bits and 1 m/DN
Special DN values	-9999 for void pixels, and 0 for sea water bodies

Table 11: Basic characteristics of the ASTER GDEM (ASTER G-DEM, 2007)

Table 12 compares main characteristics of ASTER GDEM with SRTM 3¹ DEM. The ASTER GDEM which is used for InSAR and SCT processing, is available from ERSDAC data centre of Japan and LP DAAC data centre of NASA.

SAR images usually cover more than one 1° by 1° tile of DEMs and therefore, some neighbouring tiles were mosaicked into one big tile to make a proper DEM which covers the study area and all of relevant SAR images. ENVI software was used for mosaicking 8 tiles of ASTER

1 At 3 arc sec.

GDEM to cover the study area between latitude of 41°N to 44°N and longitude of 12°E to 15°E. Figure 11 shows position of each tile and a thumb nail view of the final prepared DEM.

	ASTER GDEM	SRTM 3
Data source	ASTER sensor	Space shuttle Radar
Release year	2009	2003
Data acquisition period	2000 onward	11 days (in 2000)
Posting interval	30 m	90 m
DEM accuracy (stdev.)	7~14 m	10 m
DEM coverage	83°S to 83°N	56°S to 60°N
Area of missing data	Areas with no ASTER data due to constant cloud cover (supplied by other DEMs)	Topographically steep area (due to Radar imaging geometry)

Table 12: Comparison ASTER GDEM with SRTM DEM (ASTER G-DEM, 2007)

Each ASTER GDEM tile file contains a Quality Assessment (QA) file, as well as the DEM file. QA file conveys two basic piece of information: 1- Stack number, which is the number of scene-based DEMs contributing to the final ASTER GDEM product, and 2- Source data set number, which identifies source of data set used for replacing bad values in ASTER GDEM. Each pixel in QA file, contains a number of only one of these two categories.

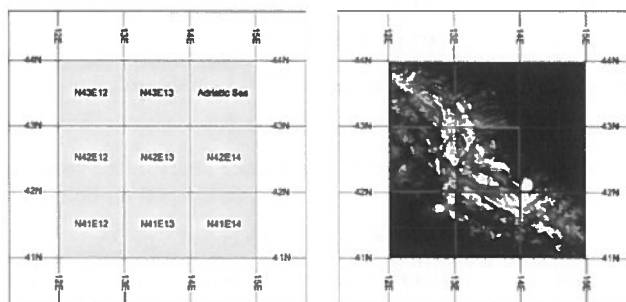


Figure 11: Sketch map of the prepared ASTER GDEM

QA files of ASTER GDEM tiles for the study area, were investigated to assess the quality of each tile. According to ASTER GDEM 'read me' file (available in zipped file of each tile), height anomalies may remain in the GDEM, where the stack number is three or less. Based on this fact, corresponding QA files of the DEM tiles were classified to two groups of pixels: Class 0 (pixels with stack number of three or less) and Class 1 (pixels with stack number greater than 3). Table 34 in Appendix B shows the result of classification. In this table, 'Ratio' shows the proportion of number of pixels in group 1 to total number of pixels in the DEM tile (equals to sum of class 0 and class 1). According to this table, maximum 0.33% of pixels (in the tile N43-E13) are prone of showing height anomalies. This ratio is even less for the other tiles, and is neglected.

4.1.2.2 *Orbital parameters*

According to interferometry equation (see Equation 1 in Chapter 2), ϕ_{orbit} is one of the contributing phase errors caused by inaccurate orbit parameters of the satellite. Conversion of phase interferograms to absolute surface displacement requires a relative baseline accuracy of 5 cm or better (Reigber et al., 1997).

Orbital parameters of SAR satellites for repeat pass interferometry or so-called orbit files, are provided by relevant agencies or universities in preliminary and precise processing and accuracy levels. Preliminary files have less accuracy, and are produced as a fast delivery product for studies in which lower accuracy is needed, for example rapid investigation of a seismic event immediately after the incidence. On the other hand, precise orbit files are produced with maximum possible accuracy, but are available with some delays.

For ENVISAT satellite, there are two sources of obtaining orbit files: Department of Earth Observation and Space Systems (DEOS) of Delft University of Technology and ESA. Both of these institutes are providing preliminary and precise orbit files, but in different formats. In this research, precise orbit files produced by EAS using Doppler Orbitography and Radiopositioning Integrated by Satellite (DORIS) method, are used to remove orbital phase signature from interferograms.

For ALOS satellite, precise orbits are delivered with the leader file of L1.0 products, as 28 state vectors with accuracy of better than one meter, and they are available three days after data acquisition (Sandwell and Wei, 2006).

4.1.2.3 *Instrumental files*

Instrumental files are all used data files to generate a product, other than the direct measurements of the instrument. Instrumental files include: calibration data that was measured on-board but are not part of the main measurements of the instrument; external calibration files from sources other than the satellite; processor configuration files, and any other files needed by instrument processors (ENVISAT Auxiliary Data, 2009). In other words, instrumental files contain the most recent information about calibration and the instrument parameters.

ESA provides the instrument files for ENVISAT satellite, available on ASAR Auxiliary Data Files website. These files will be used in this research to achieve the maximum accuracy.

4.1.2.4 *Geological map*

A geological map is used here for exploration of the study area and interpretation of the results.

Istituto Superiore per la Protezione e la Ricerca Ambientale¹ (ISPRA) of Italy, has produced geological maps of Italy, which are accessible by ISPRA website at two scales of 1:50,000 and 1:100,000. Sheet number 359 at scale 1:50,000, was chosen to study geological settings of L'Aquila area (the geological cross-section of Figure 6 in Chapter 3, was taken from this map).

A simplified geological-structural map of the central Apennines has been released in the report of Blumetti et al., 2009 (see Figure 71 in Appendix A). This map along with the geological map of Italy at scale 1:50,000, are used in this research.

1 National Institute for the Protection and Environmental Research

4.1.2.5 Faults map

Deriving approximate coordinates of the start, mid and end points of the faults and other geometrical parameters, such as length and strike, are the main applications of this map in this research, as well as interpretation of the results. Not high accuracy is expected by this map, because more accurate coordinates will be found in Inversion problem.

A map of active faults for L'Aquila area has been published in the report of GEER, 2009. This map was georeferenced in UTM coordinate system using coordinates of 20 existing cities on it, trace of faults was digitised and finally exported to shape file format (see Figure 72 in Appendix A). This map is used as a basis for deriving geometrical parameters of faults on surface and interpretation of the results.

4.1.2.6 NDVI map

In repeat-pass interferometry, seasonal variations in vegetation can cause changes in surface scattering characteristics (Hao et al., 2008), and changes of backscatter phase between two passes, can lead to decorrelation (see §2.1.3).

Normalized Difference Vegetation Index (NDVI), is an index which provides a standard method for comparing vegetation greenness between satellite images and has been accepted as a good indicator for providing vegetation properties and associated changes for large scale geographic regions (Li and Kafatos, 2000). It can be used as an indicator of relative biomass and greenness (Chen and Brutsaert, 1998) and is calculated using the following formula:

$$NDVI = \frac{NIR - Red}{NIR + Red} \quad (23)$$

NDVI ranges between -1 and 1, corresponding to pure water and temperate and tropical rainforests, respectively. Low values around zero (-0.1 to 0.1) are generally correspondent to bare lands of rock, sand, or snow and shrubs and grasslands are presented by positive mid-range values (0.2 to 0.4 approximately).

To argue about and highlight the inverse relationship between coherence values of interferograms and amount of vegetation, a NDVI map was generated using band 4 (NIR) and band 3 (Red) of four scenes of LANDSAT-7 ETM+ in SLC on, gap-filed mode and L1T¹ processing level (listed in Table 13), shown in Figure 75 in Appendix A.

Path ²	Row ²	Acquisition date	Scene ID
190	030	010609	LE71900302001160EDC00
190	031	010609	LE71900312001160EDC00
191	030	010803	LE71910302001215EDC00
191	031	010803	LE71910312001215EDC00

Table 13: LANDSAT-7 scenes used for making NDVI map

- 1 The processing level includes radiometrical, geometrical, and precision corrections. A DEM also has been used to correct parallax error due to local topographic reliefs (LANDSAT DFCB, 2009).
- 2 In Worldwide Reference System (WRS).

This map shows presence of vegetation in the study area as measured by NDVI index and formed from combination of the red and near infra-red bands of LANDSAT-7 ETM+ data set. The NDVI is more a measure of chlorophyll density than biomass. However, they are closely related, when the canopy is dense.

4.1.2.7 Slope and aspect maps

A slope and an aspect map were made separately using ASTER GDEM. The slope map classified according to incidence angles of ENVISAT ASAR (23°) and ALOS PALSAR (35°) image data sets. Pixels with slopes lower than the relevant incidence angle were assigned 1 and vice versa, separately for each sensor. The aspect map classified according to heading angles of ENVISAT and ALOS satellites in ascending and descending orbit passes, shown in Figures 12 to 13. The numbers 1, 2 and 3 in these figures are the codes used for classification of the aspect map.

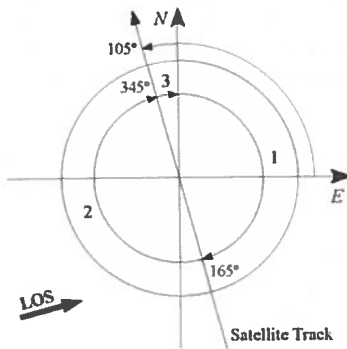


Figure 12: ENVISAT heading angle in ascending pass

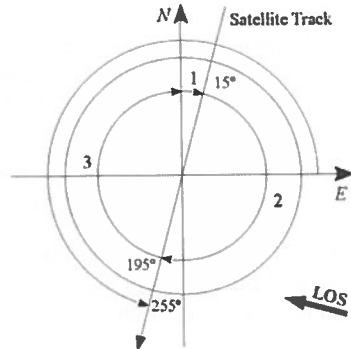


Figure 13: ENVISAT heading angle in descending pass

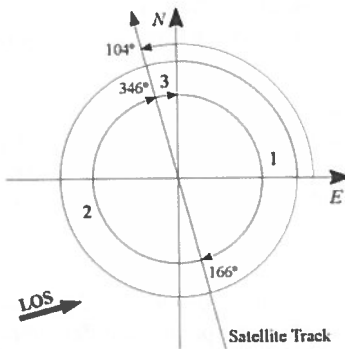


Figure 14: ALOS heading angle in ascending pass

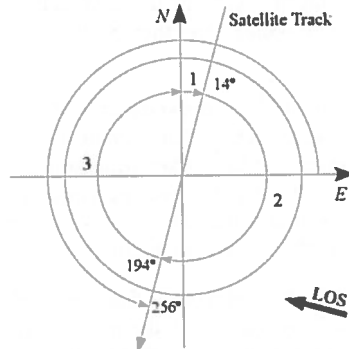


Figure 15: ALOS heading angle in descending pass

Because these two satellites have almost same heading angles (105° and 104° in ascending and 255° and 256° in descending passes, respectively for ENVISAT and ALOS), two common

aspect maps, one for the ascending and another one for the descending passes, made for ENVISAT and PALSAR satellites.

4.1.3 InSAR software

Among a variety of InSAR software, the Repeat Orbit Interferometry Package (ROI_PAC), developed by JPL/Caltech, was chosen for interferometry processing which is widely used in academic and research communities (Rosen et al., 2004; Julea et al., 2006).

From the initial experiments in space-borne Radar interferometry (Zebker and Goldstein, 1986), ROI_PAC has been developed through the collaboration of many researchers at the JPL and Caltech (Rosen et al., 2000). ROI_PAC primarily developed to work with ERS satellites SAR data sets and now is configurable to work with 'strip-mode' data from all existing satellite Radar instruments (Rosen et al., 2004).

It uses raw Radar data, Orbit files, DEMs and ancillary information from telemetry for generating the full resolution SAR images, interferograms, phase images measured as principal value and continuously unwrapped DEMs and error estimates as well as displacement maps, each of them in both Radar coordinate system and georeferenced to a DEM (Rosen et al., 2004). Figure 9 shows processing strategy of ROI_PAC.

The theory and methodology of ROI_PAC have been explained in Buckley, 2000, and Fielding, 2008a, respectively. A short summary of ROI_PAC algorithms and methods, are stated here from Fielding, 2008a, as a reference for this research.

ROI_PAC uses raw data sets in the input. SLC SAR images are formed from raw images, tie points are matched and interferograms and correlation files are made. This general procedure, is accomplished in some detailed steps and is explained as follows.

Raw SAR images are ingested with different ingestion programs corresponding to each satellite data set. ROI_PAC does azimuth spectrum filtering as a part of focussing the raw data to SLC. The average of the DC of the two input scenes and the amount of azimuth spectrum overlap for filtering, are calculated. Baselines are also calculated between two orbits for the area covered by the scenes, and then SAR images are formed or focused (range and azimuth compression).

2D field of offsets between two SLC images are calculated, and then the initial offsets between scenes are estimated from orbits and scene parameters, and then are refined by a gross matching process. A first order affine transformation is fitted to gross offsets and cull points that exceed 0.5 pixels from fit. Average of gross offsets is taken and offsets from gross matching are filtered in fine matching step. An affine transformation is fitted to fine offsets and cull points that exceed 0.08 pixels from the fit.

A second order polynomial function is fitted to the culled offsets. Slave SLC image is resampled and co-registered to the master SLC image using these points. Interferogram is then formed by multiplying each complex pixel of the first scene by complex conjugate pixel of the second scene. Looks are taken in azimuth before writing the interferogram to a complex output file.

The formed interferogram has all phase signatures including orbit geometry, topography, deformation, atmosphere, etc. (see Equation 1 in Chapter 2). Initial flattening of the interferogram is done by removing the expected phase for the InSAR orbit geometry with a 'curved earth'

model without any topography. A fake DEM with constant elevation (zero by default) is constructed, and then its phase signature is subtracted from raw interferogram (interferogram flattening). The flattened interferogram has still phase proportional to elevation, but orbit fringes have been removed.

After the initial flattening of the interferogram, ROI_PAC calculates the spatial correlation of the phase as an estimate of the interferometric coherence changes between 0.0 and 1.0. Amplitude of the correlation image is the average of the amplitudes of the two scenes.

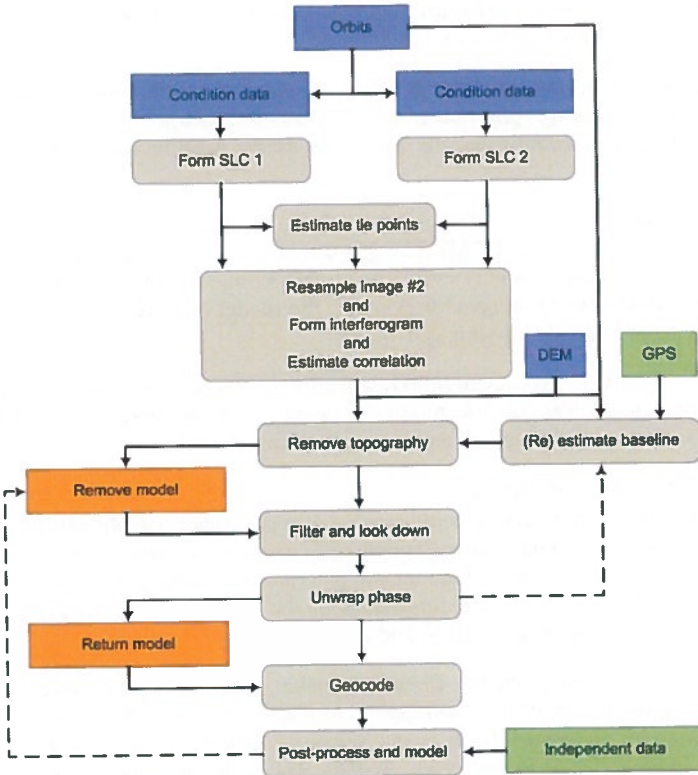


Figure 16: ROI_PAC work flow (modified from Fielding, 2008a)

ROI_PAC simulates the Radar image amplitude from a DEM and the orbit for the master scene, and projects the elevations into the Radar coordinates of the interferogram and then calculates the topographic phase and subtracts it from the original interferogram. The DEM can be either in Geographical (latitude-longitude) or UTM coordinate system.

A deformation model can also be supplied to the software to remove large-scale phase effects that might bias the baseline estimate (Rosen et al., 2004). The models which can include coseismic models or inter-seismic models, are projected into SAR geometry and subtracted from the 'seismic' interferogram. Models are in original DEM coordinates, but can be at coarser resolution.

Filtering is done differently depending on unwrapping method, either before masking (when old unwrapping method is used) or within unwrapping (when new unwrapping method is used). Power spectrum filtering (Goldstein and Werner, 1998) is applied first and then additional filtering is done, if specified by user. There is also a way to run a simple boxcar filter, but this is not in the regular work flow.

Phase unwrapping is done according to the method specified by user (classic or new method). The new method, does the unwrapping in patches. Segmenting the image is faster and helps to localize unwrapping errors (Rosen et al., 2004). So, it can work on very large images that are not unwrapped with the classic program. The new method includes also additional techniques, such as guiding centres for branch cuts.

In the default flattening method, the baseline calculated from the orbits is used for the final products. However, if 'topography flattening' method is set, then the unwrapped phase and the topography in the Radar coordinates are used to refine the baseline length, and new baselines are estimated.

Final unwrapped phase is transformed from Radar coordinates to geographic coordinates (same as the system used in the DEM). The geo-coded result is usually a subset of DEM area, but has the same grid spacing and is shifted by an integer number of DEM pixels. If coseismic or inter-seismic model was subtracted previously, the model or models are added back to the unwrapped phase and then the result is geo-coded.

Although ROI_PAC is a complete InSAR software, it should be supported by other complementary programs and codes, such as phase unwrapping. Among these codes, SNAPHU has a key importance for phase unwrapping and is explained in § 4.1.3.1 .

4.1.3.1 Unwrapping software

Two dimensional phase unwrapping is the process of recovering unambiguous phase data from a two dimensional array of phase values known only modulo 2π radian, and it is a key step in the analysis of InSAR data. While phase unwrapping is even challenging in the best situations, it poses unique difficulties when the dimensions of the interferometric input data exceed the limits of computational capabilities (Chen and Zebker, 2002).

In order to address these problems, Chen and Zebker, 2002, have proposed a Statistical-cost Network-flow Algorithm for Phase Unwrapping, implemented as a code and named SNAPHU. This code has been referenced to in many scientific articles as an unwrapper code (e.g. Pritchard and Simons, 2004; Peyret et al., 2008b). The code attempts to compute congruent phase-unwrapped solutions that are maximally probable in an approximate a-posteriori sense. The algorithm's solver routine is based on network optimization (SNAPHU Online Help, 2003).

According to SNAPHU website, the algorithm consider phase unwrapping problem as a maximum a-posteriori probability (MAP) estimation problem, the objective of which is to compute the most likely unwrapped solution given by the observable input data.

Because the statistics which relate the input data to the solution depend on the measured quantity, SNAPHU incorporates three built-in statistical models for: topography data, deformation data, and smooth generic data. The posed optimization problem is solved approximately with use of network-flow techniques. SNAPHU always produces complete unwrapped solutions, and in the conducted tests, its accuracy was comparable to or better than of other avail-

able algorithms. SNAPHU is specially helpful when the coherence is low and built-in unwrapping module of ROI_PAC fails.

4.2 SCT

InSAR is poorly sensitive to displacements perpendicular to the satellite LOS direction, due to incidence angle. So, the horizontal surface displacements are expected to be estimated weakly by this technique, in the area close to a fault trace or rupture. A way to complete InSAR technique, is to estimate the west-east and south-north components of surface deformation by computing sub-pixel offsets between two images (optical or SAR), acquired before and after the seismic event. In this research, both SAR and optical image data sets are used for SCT.

Coseismic ENVISAT SAR images with minimum available spatial baselines are selected in ascending and descending passes and then phase signature is removed from SAR images using precise orbit files.

SAR sub-pixel correlator software is used to apply SCT on the reduced SAR images in complex space, using both phase and amplitude. The result will be two offset files in range and azimuth directions.

SCT is also applied on band 3N of two pairs of ASTER optical images (to cover the whole study area) with minimum B/H ratio. The result will be two offset files in west-east and south-north directions.

Offsets from both data sets, are geo-referenced using the available DEM. Finally, all results from different data sets and image pairs are compared and similarities and differences are discussed and interpreted. The comparison of the results from different sources and techniques (SAR versus optical data set, SCT in domain versus in complex space), brings a type of validation, intrinsically. However, the results will be compared with results of other studies from other techniques and data sets such as GNSS observations.

The available image data sets and appropriate software for SCT, are introduced here and the result of applying the technique will be presented and discussed on the next chapter.

4.2.1 SCT using SAR image data sets

Different algorithms have been developed (see §2.2.3) and accordingly, different software are available for applying SCT on SAR images. Among them, IMCORR (Scambos et al., 1992) and AMPCOR (part of ROI_PAC, Rosen et al., 2004) are two scientific and open source image correlators which generate offsets using NCC method in spatial domain. The later code is used in this research to apply SCT on the following SAR data sets.

4.2.1.1 Radar image data sets for SCT

AMPCOR (§ 4.2.1) can work with all raw SAR images that ROI_PAC can process (among them ERS 1/2 AMI, ENVISAT ASAR, ALOS PALSAR and RADARSAT-1/2 SAR). Table 14 shows minimum detectable horizontal displacements in range and azimuth directions, for some of the supported image data sets by AMPCOR.

Specific considerations should be taken into account for choosing SAR image data set, as well as common issues mentioned in § 4.1.1 : 1- SAR image pairs should bracket the seismic event (coseismic pairs) and, 2- have minimum available perpendicular baseline. These features are highlighted when the study area is exposed by decorrelating factors, e.g. due to vegetation, snow and soil moisture.

Considering all technical parameters and financial limitations, this study is limited to coseismic ENVISAT ASAR images with minimum available spatial baselines.

Satellite/ Sensor	Incidence angle	Ground Resolution ¹		Detectable disp. ²	
		Azimuth	Range	Azimuth	Range
ERS-1/2/ AMI	23°	3.98	20.23	0.20	1.01
ENVISAT/ ASAR	23°	4.04	20.11	0.20	1.01
ALOS/ PALSAR	35°	6.25	7.49	0.31	0.37
RADARSAT-1/ SAR	35°	4.89	20.63	0.24	1.03

Table 14: Minimum detectable displacements by AMPCOR for some supported data sets

4.2.1.2 Sub-pixel correlator software for SAR data sets

Matt Pritchard et al. from Cornell University, have developed a set of python scripts to utilize power of correlator engine of ROI_PAC software, AMPCOR, to create dense sub-pixel offsets of SAR and optical images (Pritchard, 2009). The algorithm originally developed by Mark Simons in Caltech and they added capabilities of geo-rectification of the offset field, corrections for topography and computation of sub-pixel offsets for optical images (Pritchard, 2009).

This script, which is called 'pixelTrack', is complementary to ROI_PAC and is intended to take common parts of image pairs and creates pixel offsets using AMPCOR. Since ROI_PAC (§ 4.1.3) uses NCC method to calculate offsets between two SAR images in spatial domain (Pritchard, 2009), pixelTrack also uses this method to compute azimuth and range offsets. The code can also work with ASTER HDF images, as well as full SAR images.

pixelTrack can go from raw SAR data to a final geo-rectified set of offsets. Raw SAR images are converted to internal raw format of ROI_PAC, using precise orbital and ancillary files, and then baselines are estimated between pairs. Image pairs with perpendicular baselines lower than a threshold, are co-registered precisely. Azimuth and range pixel tracking results are then generated for the image pairs, using AMPCOR correlator, and finally results are looked down and geo-coded using the available DEM.

4.2.2 SCT using optical image data sets

Among different algorithms and procedures explained in §2.2.3, the newly developed procedure for coregistration of optically sensed images and correlation (COSI-Corr) is used to apply SCT on the optical image data sets.

4.2.2.1 Optical image data sets

For choosing optical image data sets, some considerations should be taken into account regarding ground resolution as well as the other common parameters, mentioned in § 4.1.1 for Radar image data sets. These features become more important specially when the geometry of causative fault is normal or magnitude of the seismic event is less than 7.0, and consecutively not too much horizontal displacement is expected.

1 Derived from header of corresponding images for mid-range.

2 Detectable displacement is calculated of 1/20 of the ground resolution.

Using COSI-Corr, image pairs can be co-registered with a 1/50 of image nominal resolution at maximum, without providing supplementary data (Leprince et al., 2007a). The minimum detectable displacement which can be achieved by COSI-Corr (equal to 1/20 of the pixel size), are summarized in Table 15 for all of supported data sets (§ 4.2.2.2).

As shown in Table 15, the finer ground resolution, the smaller detectable displacement. So, when small horizontal displacement is expected, an image data set with the finest ground resolution should be chosen. Among the supported image data sets (with considering financial limitation¹), ASTER data set is available for this research and can be obtained from WIST or GLOVIZ websites.

Satellite/ Sensor	Ground resolution	Detectable displacement
ASTER	15m ²	75 cm
FORMOSAT-2	2m ³	10 cm
SPOT 1-4	10m ⁴	50 cm
SPOT 5	2.5m ⁴	12.5 cm
QuickBird	0.6m ⁴	3 cm
WorldView-1	0.5m ⁴	2.5 cm

Table 15: Minimum detectable displacement by COSI-Corr for supported data sets

4.2.2.1.1 ASTER

Advanced Spaceborne Thermal Emission and Reflection Radiometer (ASTER) is one of the five on-board sensors of Terra satellite launched at December 1999. ASTER equipped with pushbroom sensors which are perpendicular to the platform flight path and captures high spatial resolution data in 14 different bands of EMS, from the visible to the thermal infra-red wavelengths with different ground resolutions (ASTER, 2004). Table 16 summarizes specifications of Terra and ASTER sensor.

Launch date	December 18, 1999
Orbit	Sun-synchronous
Altitude	705 km
Inclination	98.3°
Period	98.88 min
Repeat cycle	16 days
ASTER instruments	VNIR, SWIR and TIR
Swath	60 km

Table 16: Terra and ASTER specifications (ASTER, 2004)

- 1 High resolution images are so expensive and go beyond of financial range of this research.
- 2 For VNIR-3N band.
- 3 For panchromatic and merged colour bands.
- 4 For panchromatic band.

Table 35 in Appendix B, summarizes spectral bands and spatial resolution of each instrument for ASTER sensor. In this table, all looking angles are nadir except for band 3 in the range of 0.76-0.86 μm , which is backward.

4.2.2.2 *Sub-pixel correlator software for optical image data sets*

The described algorithm in Leprince et al., 2007a, has been implemented in COSI-Corr, developed with IDL and integrated under ENVI (COSI-Corr, 2004). This code was selected for SCT in this research due to its advantages (see §2.2.3).

COSI-Corr can process both satellite and aerial images. ASTER, FORMOSAT-2, SPOT/SPOT 5, QuickBird and WorldView-1, are supported data sets in the satellite image category. All of these satellites have pushbroom imaging system in which, all optical parts remain fixed during image acquisition, and the scanning is accomplished by the forward motion of the spacecraft. Consequently, every image line depends on the varying attitude of the platform. COSI-Corr corrects the viewing parameters by linearly correcting the camera look directions to compensate for attitude drifts and sensor orientation uncertainties during image acquisition (Leprince et al., 2007a).

COSI-Corr allows for automatic and precise ortho-rectification and co-registration of all of supported images and as an important advantage, does not require complementary information such as GCPs. The algorithm is only based on the ancillary data provided by observing platform (such as positions, velocities, attitudes variations and pointing directions for space crafts, or calibration reports for aerial photographs) and the knowledge of the topography of the area. Then, sub-pixel offsets are detected using the produced set of ortho-rectified images (Leprince et al., 2007b).

The precise ortho-rectification procedure relies on the automatic generation of precise GCPs. These points are generated in a way that their implied correction on the viewing geometry of the observing platform, allows for precise ortho-rectification and co-registration of the images. To make this process automatic and bias-free as much as possible, the generated GCPs and the viewing geometry parameters are both optimized.

Initial GCPs are extracted from tie points which are selected roughly between the ortho-rectified master and the raw slave images. Then a precise set of GCPs from the raw image (slave) is generated, with respect to the already ortho-rectified image (master) and refining the initial GCPs, iteratively. Image patches from the raw slave image are ortho-rectified and then, their mis-registration with the master ortho-image are estimated from correlation. The precise set of GCPs is finalized when the measured mis-registration at each patch converges to a minimum value. This procedure is made independent of any external data, if a shaded image of the DEM is available. As the first ortho-rectified image is produced, it becomes the master image for subsequent slave images. This approach is applicable for almost any region by taking advantages of the accurate available global DEMs such as SRTM DEM or ASTER GDEM, explained in § 4.1.2.1 (Leprince et al., 2007b).

Once a set of precise GCPs has been produced, the inverse mapping matrices that associate ground coordinates to raw pixel coordinates are calculated. These matrices define an irregular re-sampling grid in the raw image. To avoid the presence of aliasing in the ortho-rectified image, the irregular re-sampling problem is accounted for, and then the ortho-image is built (Leprince et al., 2007a).

Raw images are wrapped onto the topography within the DEM resolution, and pairwise co-registered with a 1/50 pixel accuracy, which allows for the measurement of horizontal displacements with an accuracy of 1/20 of the pixel size (Leprince et al., 2007b).

Horizontal displacements are retrieved by applying the sub-pixel correlation of the pre- and post-earthquake ortho-rectified images. Image correlation is achieved with an iterative, unbiased correlator that estimates the phase plane in the Fourier domain (Leprince et al., 2007b). Two correlation images are the results of processing, one presenting horizontal displacement in the west-east direction (positive toward the east) and the another one in south-north direction (positive toward the north), as well as a SNR channel to assess the quality of measurements. Figure 17 summarizes the processing steps of COSI-Corr.

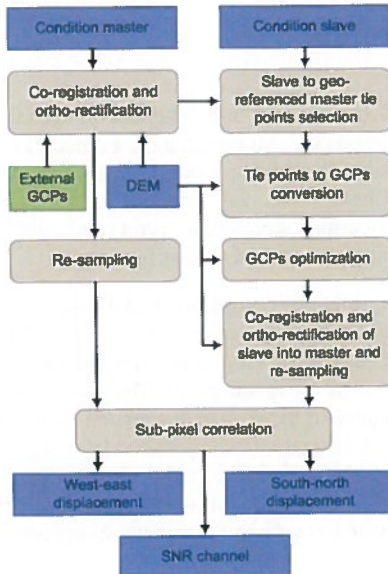


Figure 17: COSI-Corr work flow

Except some limitations in number of supported satellites image data sets, COSI-Corr is a complete software for SCT, specially that the main core has been bundled with a couple of complementary tools for de-noising data sets, filtering and changing pixel values, de-stripping images and removing undulations, displaying vector field, stacking profiles across a fault on the correlation file and compute the re-sampling distances.

4.3 Inversion problem

Theory and applications of Inversion problem were explained in §2.3. To find geometrical and source parameters of the causative fault, and distribution of slip at depth, are the main objectives of using Inversion problem in this research. Indeed, this is continues of InSAR technique in depth (Figure 9); while InSAR finds deformation on the surface, Inversion problems looks for underground deformation (slip).

The inversion problem is done in two main steps, namely the NA and the LS Inversion. While the NA algorithm is applied to find overall earthquake motion, LS algorithm finds distribution of slip on the fault plane, which has been already fixed by the NA algorithm.

Two outputs of interferometry step: phase of unwrapped interferograms and corresponding coherence file (§ 4.1) are used as the main input files for both NA and LS inversion algorithms. Other inputs are some setting parameters (for the inversion code or the inversion model) which are either assumed or calculated.

Part of the unwrapped interferometric phase image (georeferenced in UTM coordinate system) is subset using the corresponding coherence files in order to select just the significant pixels and then is spatially sampled to a certain step to reduce computational costs (using a small step, requires a large amount of memory). Then both files are converted to binary array of floats, and are fed to inversion codes.

4.3.1 NA algorithm

The NA algorithm (see §2.3.1) has been implemented in 'geodinv_na' executable code, by Michel Peyret et al., from Université Montpellier 2, France (Peyret et al., 2007) based on stochastic approach of Malcolm Sambridge from The Australian National University (Sambridge, 1999a; Sambridge, 1999b). The code has been applied successfully for finding the source parameters of the Bam earthquake, 2003 (Peyret et al., 2007) and Chalan-Chulan, 2006 (Peyret et al., 2008b) in Iran, along with the LS algorithm.

The code is run by passing a set of computation and model parameters as well as the unwrapped interferogram and corresponding coherence files (§ 4.3). Computational parameters consist: maximum number of iterations, sample size for the first iteration, sample size for all other iterations and number of cells for re-sampling. Model parameters include: fault strike and dip angle, approximate coordinates of the mid-fault segment on the ground surface, components of sensitivity vector (see §2.1.4.4), and adjusting interval for seven parameters of: position of centroid along strike and along dip (relative to mid-fault coordinates), width and length of the rectangular patch of uniform slip, Young modulus, and strike and dip slip components. A coherence threshold also can be adjusted as an input parameter along other parameters to choose only significant pixels.

Computational parameters are assumed in a way that the algorithm is convergent. For the model parameters, strike and dip angles are assumed first according to geological map (§ 4.1.2.4) and seismological report (e.g. CMT; see §3.2.1). Coordinates of mid-fault is derived from faults map (§ 4.1.2.5) or geological map. The other seven parameters of the model are assumed close to reports from seismology, but intervals are taken large enough to give flexibility to the model.

Optimizing the model is done iteratively with different parameters for strike and dip. The code developer, advises to limit the search interval for the strike-slip parameters. According to him, it is useless and sometimes risky to test unlikely models. If the optimal model is satisfactory, the domain of analysis can be enlarged later (Peyret, 2009, personal communication, September 8). Also Young modulus interval should be kept small, since this is not a sensitive parameter at this step of processing (Peyret, 2009, personal communication, September 7).

RMSE misfit and correlation between observed and modelled unwrapped interferograms, are then computed for every pair of strike and dip angle. Following this, different intervals are

tested for the seven parameters. The model is optimized when RMSE misfit and correlation are respectively minimum and maximum.

4.3.2 *Linear least square inversion*

The LS inversion algorithm (see §2.3.2) for SAR data set¹, has been implemented in 'inverseokada_SAR' executable code, by Michel Peyret et al., from Université Montpellier 2, France (Peyret et al., 2007). The code has been applied successfully for finding the source motion of the Bam earthquake, 2003 (Peyret et al., 2007) and Chalan-Chulan, 2006 (Peyret et al., 2008b) in Iran, along with the NA algorithm.

The first step for LS inversion consists of creating a grid of nodes for the fault geometry. This grid is made by coordinates of start and end points of the fault (using the strike angle from NA inversion, faults map and geological map, but the length is taken long enough to reach the zero deformation area), dip angle (from NA inversion), depth along dip (approximately from reports of seismology), and number of nodes along strike and dip.

The code is run by passing some parameters for the model, as well as the sub-sampled unwrapped interferogram and corresponding coherence files (§ 4.3). Model parameters consists: satellite heading track angle, incidence angle, a-priori dip slip and its weight, weight for InSAR data set and weight for roughness constraint.

Various smoothness constraints and weights for InSAR data set are tested and RMSE misfit and correlation between observed and predicted models are computed for every model. Decreasing the smoothness leads to solutions with higher geodetic moment and lower RMSE. However, slip models with smoothness lower than some threshold do not significantly improve the data fitness and results in unrealistic slip gradients (Peyret et al., 2007). For the final solution, a compromise among these parameters is necessary and gives the best solution.

1 Michel Peyret and colleagues, have also developed an inversion code for GNSS data set.

Chapter 5

Cassandra: ... Destroyed again, and this time utterly!
Chorus: She seems about to predict her own misfortunes ...
Of your prophetic fame we have heard before, but in this matter, prophets are not required.
Aeschylus, The Agamemnon

5 Results and interpretation

The earthquake of April 6th, 2009, in L'Aquila, was studied from geology, space geodesy and geophysics points of view using InSAR, SCT and Inversion problem techniques. Accordingly, different data sets were chosen and processed in a way that, at least two independent data sets were available for each part. This approach gives the opportunity to compare the obtained results for each method and implies a type of validation, intrinsically.

5.1 SAR interferometry

InSAR was employed in this study to measure ground surface deformation caused by the April 6th, 2009, earthquake in L'Aquila area in the satellite LOS direction and the deformation was determined using two interferometric pairs of ENVISAT ASAR and ALOS PALSAR data sets.

5.1.1 ENVISAT ASAR data set

The InSAR technique was applied on two coseismic and interferometric pairs of ENVISAT ASAR images, listed in Table 17, all acquired in imaging mode, image swath two (IS2) and L0 processing level.

Pair no.	Orbit	Track	Acquisition date	Pass	B_{\perp} ¹	Height ambig. ²
1	37257	129	2009/04/15	Asc.	197 m	46 m
	36756		2009/03/11			
2	37207	079	2009/04/12	Des.	-168 m	-54 m
	36205		2009/02/01			

Table 17: ENVISAT ASAR image pairs for interferometry

These two pairs cover extents of the epicentral region spatially very well and have minimum temporal baselines (35 days for the ascending and 70 days for the descending pair) and also bracket the two main after-shocks (see §3.2.2 and Table 31 in Appendix B, for the list of after-shocks).

¹ Refined using the unwrapped phase and the topography.

² Calculated from ancillary data files provided in header of images, using Equation 10 in Chapter 2.

Raw data was converted to SLC format using DORIS precise orbit parameter and instrumental files (see §4.1.2) by InSAR software (see §4.1.3) to remove orbital phase signature. The average of the DC was calculated separately for the images of each pair. The amount of azimuth spectrum overlap for filtering are shown in Figures 76 and 77 in Appendix A. In these figures, the DC is stated in Pulse Repetition Frequency (PRF) unit and has to be multiplied by the PRF value, in order to be converted to Hertz unit.

Figures 76 and 77 show that, except in a small portion of the ascending pair, the scenes in each pairs have the same DC shift pattern. The image acquired on April 15th, 2009 (in Figure 76), shows small jump between the line numbers 3390 and 3930 (the black line) which is less than one percent of the spectrum width and is negligible. Comparing these figures with Figure 10 in Chapter 4, will explain the instability and changes in DC of ERS-2 SAR images more (which was the main reason of failure for SAR interferometry using ERS-2 images).

Tie points were matched, to make interferograms and coherence files. Figures 78 and 79 in Appendix A, show the distribution of range and azimuth offsets versus range and azimuth samples for the ascending and descending interferometric pairs, respectively. The figures show a good spatial distribution of tie points over scenes, and this indicates the good quality of image matching.

Interferograms were corrected from topographic phase signature and were georeferenced using ASTER GDEM. The remained fringe system is mainly related to the L'Aquila earthquake movement. Figures 18 and 19 show these two coseismic ASAR interferograms in ascending and descending passes, respectively. In these figures, red line segments show active faults of the area superimposed from the active fault map (see Figure 72 in Appendix A).

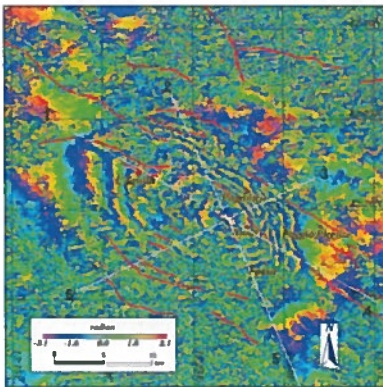


Figure 18: ASAR interferogram for the ascending pair (09/04/15-09/03/11)

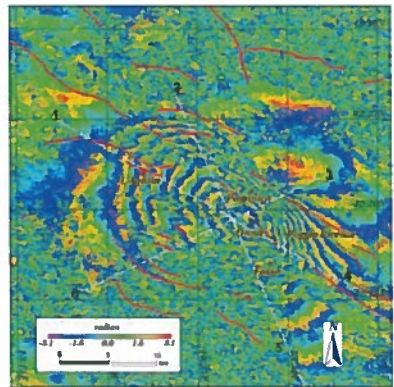


Figure 19: ASAR interferogram for the descending pair (09/04/12-09/02/01)

Although some residual fringes which might be due to atmospheric artefacts, are seen in the interferograms, particularly in eastern and south-eastern parts of Poggio Picenze, their amplitude is estimated less than a fringe, which should not affect the deformation fringe pattern significantly.

The structure of fringes is relatively simple and displays a one lobe pattern for the ascending interferogram on the hanging-wall and an asymmetric two lobes pattern for the descending interferogram, on the hanging and foot-wall of the causative fault. The fringes are corresponding to elongation on the hanging-wall and shortening on the foot-wall of the fault in the satellite LOS direction, and with respect to the geometry of the fault, they are interpreted as subsidence and uplift in the satellite LOS direction, respectively.

This result is equivalently consistent with a dip-ward motion on a north-west to south-east strike trending normal fault, dipping to the south-west. This fault which is located about 6.5 km to the east of L'Aquila city and surrounds Paganica village from the east, is named 'Paganica fault' and is supposed to be responsible for the main event.

The fringes systems do not suddenly close on the trace of the Paganica fault, but display two trends with different gradients: one to the north-east and the other to the south-west of the area with the maximum deformation in the satellite LOS direction (GEER, 2009).

The gradients of deformation in the satellite LOS direction on the hanging-wall are asymmetric in both interferograms with the greatest gradients on north-east of the lobes. Due to 23° incidence angle for ENVISAT ASAR image data set, the technique is more sensitive to vertical displacement than horizontal (see Table 3 in Chapter 2) and provides estimation of the satellite LOS deformation component directly.

The fringe systems show variations in trend at many points and along different lines, which are associated with active tectonic elements that have had a coseismic displacement of modest extent, i.e. Pettino fault (located to the north-west of L'Aquila) and Bazzano fault (located between L'Aquila and Paganica) (GEER, 2009).

The calculated baselines from orbits, were refined using the unwrapped phase and the topography in the Radar coordinates, and then were used for calculation of ambiguity of height, presented in Table 17. Accuracy of ASTER GDEM used for this process, is less than the height ambiguities of both pairs (see Table 12 in Chapter 4). This shows contribution of topographic residues are smaller than one fringe (in proportion).

The centres of fringes are slightly different in the ascending and descending interferograms. The separation is about 1 km and the centre of fringes in the ascending pair is located to the south-east of the centre of fringes in the descending pair, both of them placed on flat farmlands. The separation in centres of fringe systems, which are coincident with maximum subsided points in satellite LOS direction, is due to post-seismic relaxation which is found out by comparing study of Salvi et al., 2009, and interferograms in Figures 18 and 19.

Salvi et al., 2009, have processed one pair of COSMO-SkyMed SAR image data set acquired on February 19th and April 9th, 2009, shown in Figure 35 (with 480 m perpendicular baseline and 36° incidence angle). In this figure, the bigger green square shows the main shock epicentre and the corresponding focal mechanism, and the smaller squares show after-shocks with $M_w > 5$ in the area. The yellow segment indicates the observed fracture surface in this study, and the triangles mark the position of the GPS permanent stations used for comparison with the InSAR results (§5.2.1).

This figure shows that the initial coseismic surface deformation was concentrated to the north of the main event epicentre along a line running from L'Aquila and Poggio Picenze. But ENVISAT ASAR coseismic interferograms from this study, show that the extent of the displace-

ment increased considerably towards south and south-east of the main shock epicentre after April 9th, and has become much more homogeneous around it. In other words, the deformation has had a movement from north-west to south-east, along L'Aquila to Poggio Picenze axis.

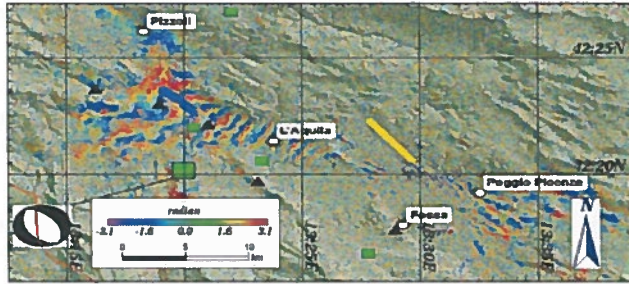


Figure 20: COSMO-SkyMed interferogram (09/02/19-09/04/09) modified from Salvi et al., 2009

Therefore, because the ascending interferogram spans three days after the descending pair, it has more share of the movement and can reveal it to south-east. During the time interval between end of the ascending and the descending pairs (since April 12th till April 15th), the movement was current with the calculated rate of ~ 0.3 km/day toward the south-east.

Six cross sections (white lines in Figures 18 and 19), were drawn from centre of fringe systems outward to count number of fringes in different directions. The cross sections were replicated on the other figures related to ENVIASAT SAR interferograms and have made a frame to compare different parts of relevant fringe systems. Eight and nine fringes, equivalent to 22.6 cm and 25.5 cm subsidence in the satellite LOS direction, are observed in ascending and descending pairs, respectively (the descending pair shows one more fringe on foot-wall of the fault corresponding to 2.8 cm uplift in the satellite LOS direction as well). Table 36 in Appendix B, shows number of fringes along each cross section.

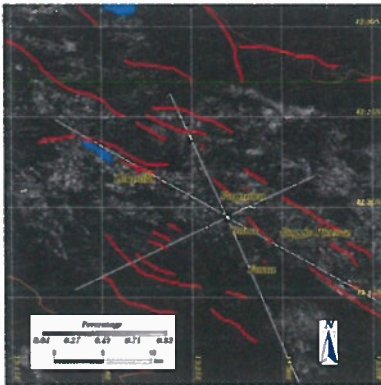


Figure 21: coherence map of the ascending ASAR interferogram

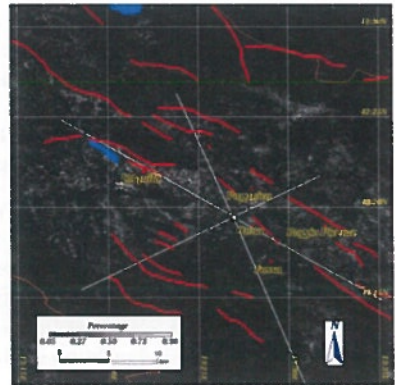


Figure 22: coherence map of the descending ASAR interferogram

The interferograms (in Figures 18 and 19) have high quality at least in three quarters of the affected area and clear fringes are seen on L'Aquila city, and Paganica and Fossa villages. However, the interferograms have decorrelated in the south and south-western parts of the fringe systems centre, where a hill of higher than 2100 m elevation is located among Bango, Lucoli and Casamaina villages. The coherence maps of the interferograms also show low values in the decorrelated area over the hill (Figures 21 and 22).

The corresponding NDVI map (Figure 23) for the area, does not show significant vegetation over the hill that can decorrelate interferograms. Other hypotheses for the decorrelation, might be shadow (due to deep steep and Radar imaging geometry) and other sources of temporal variations of the earth surface (e.g. due to snow coverage).

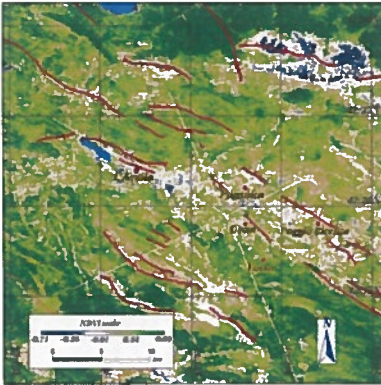


Figure 23: NDVI map

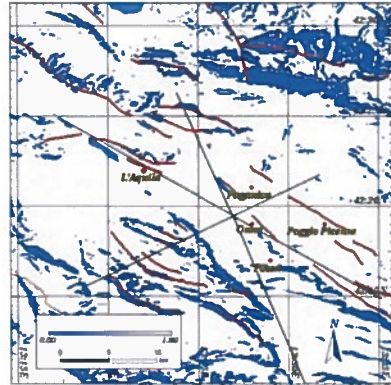


Figure 24: Slope map for ASAR

To investigate the first hypothesis, interferograms were superimposed on the slope map (Figure 24). A meaningful relation between the uncorrelated area and the area with slopes more than ENVISAT ASAR incidence angle (23°), was observed. These area (blue patches in the slope map), make strong layover and shadow effects (slope > incidence angle) on the SAR images and lead to the decorrelation.

To evaluate the second hypothesis, another interferometric pair of ENVISAT ASAR images, was chosen, almost from the same date of two consecutive years, when it is supposed there is no ice or snow on the hill at acquisition time (April). Table 18 shows specifications of the new coseismic interferometric pair, and the resulted interferogram is shown in Figure 25.

Pair no.	Orbit	Track	Acquisition date	Pass	B_{\perp}^1	Height ambig. ²
3	37207	079	2009/04/12	Des.	36 m	251 m
	32197		2008/04/27			

Table 18: ENVISAT ASAR image pair for interferometry

1 Refined using the unwrapped phase and the topography.

2 Calculated from ancillary data files provided in header of images using Equation 10 in Chapter 2.

This interferogram shows clear fringes over the hill, where it was almost completely decorrelated in the first and the second interferograms. Also the corresponding coherence map of this interferogram (Figure 26) shows high values over the hill.

Although the new interferogram show high quality of fringes over the hill, in the area between Paganica and Pettino faults (white dashed line box in the Figure 25), it is not as good as the main interferograms (shown in Figures 18 and 19) are. This is seen also from the corresponding coherence map. While the coherence map is white over the hill and the urban area of L'Aquila city (corresponding to high values), it is dark over the other area (corresponding to low values). Farmlands of Paganica, Onna and Poggio Picenze villages are located here and at the image acquisition date (April), farmlands are supposed to show maximum temporal variations due to rapid grow of vegetations and drainage system.

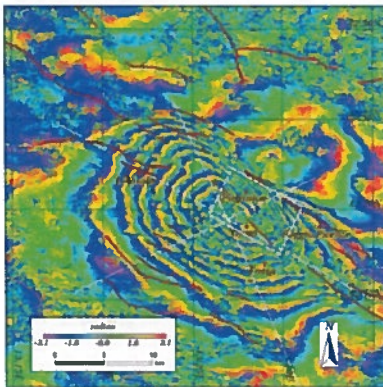


Figure 25: ASAR interferogram for the third pair(09/04/12-08/04/27)

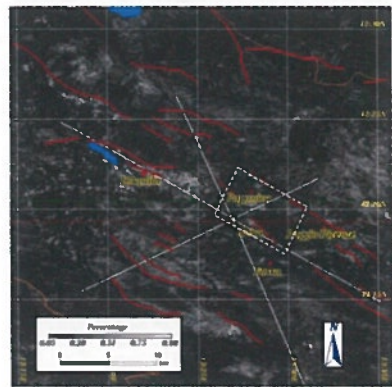


Figure 26: coherence map of the third ASAR interferogram (09/04/12-08/04/27)

The two main interferograms were unwrapped using Snaphu software (see §4.1.3.1) and converted to displacement map in the satellite LOS direction, shown in Figures 27 and 28.

Three profiles and six cross sections were drawn respectively along (parallel to the causative fault) and across (perpendicular to the causative fault) the deformed area (Figures 27 and 28). Deformation was measured along profiles and cross sections and results are shown in Figures 80 and 81 for the ascending and Figures 82 and 83 for the descending interferograms, in Appendix A.

Profiles from the ascending (Figure 80) and the descending (Figure 82) interferograms are in agreement in terms of measured values for subsidence, except at the beginning of the descending pair, where more uplift is seen on the foot-wall of the fault. Maximum 24.2 cm and 23.8 cm subsidence and 0.3 cm and 2.0 cm uplift in the satellite LOS direction are seen on the ascending and the descending profiles, respectively. Also values of the profile 1 and the profile 2, are closer together rather than the profile 2 and profile 3, in both figures. This shows more displacement gradient (in the satellite LOS direction) in the area between the profile 1 and the profile 2 in compare with the area between the profile 2 and the profile 3.

On the other hand, maximum 26.1 cm and 27.9 cm subsidence and 4.1 cm and 5.4 cm uplift in the satellite LOS direction, are seen on the ascending and the descending cross sections, respectively. The cross sections, both in the ascending and in the descending interferograms correspond to trace of Paganica and Aterno-Poggio Picenze faults. The cross sections show that the subsidence has started about 0.5 km before the common trace of these faults (to the north-west).

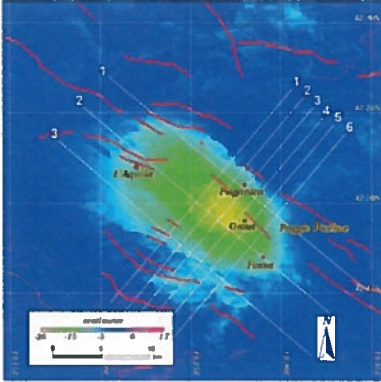


Figure 27: Unwrapped ENVISAT ASAR ascending interferogram

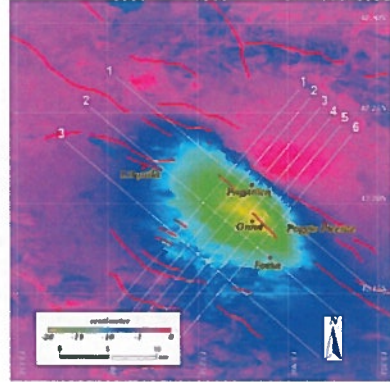


Figure 28: Unwrapped ENVISAT ASAR descending interferogram

Spatial analysis, using GRASS GIS software (see Table 32 in Appendix A), showed that maximum 26.1 cm and 28.1 cm subsidence in the satellite LOS direction have occurred in the two separate points, one at (42.321°N, 13.446°E) about 2.3 km, and the other at (42.326°N, 13.458°E) about 1.5 km to the north-west of Onna village, and maximum 1.3 cm and 5.5 cm uplift in the satellite LOS direction in the two separate points of (42.357°N, 13.490°E) about 2.7 km and (42.367°N, 13.478°E) about 2.3 km to the north-east of Paganica village on the foot-wall of the Paganica fault in the ascending and descending interferograms, respectively. This is in agreement with the field report of GEER, 2009. The report indicates that the village of Onna which is the nearest habitat centre to the point of maximum subsidence, experienced the hardest hit village near the city of L'Aquila.

The descending interferogram shows larger values for subsidence in the satellite LOS direction, than the ascending interferogram. This is due to the looking direction and the incidence angle of ENVISAT ASAR (the sensitivity vector), and the geometry of the fault (displacement vector). If the Equation 12 in Chapter 2 is expanded, the measured displacement in satellite LOS direction is:

$$r = v_x \cdot d_x + v_y \cdot d_y + v_z \cdot d_z \quad (24)$$

By substituting values of sensitivity vector (v) for ENVISAT ASAR from Table 3 in Chapter 2 into Equation 24, it is resulted:

$$r_{Asc} = (0.377) \cdot d_x + (0.101) \cdot d_y + (-0.921) \cdot d_z \quad (25)$$

for the ascending pass, and:

$$r_{Des.} = (-0.377) \cdot d_x + (0.101) \cdot d_y + (-0.921) \cdot d_z \quad (26)$$

for the descending pass. In the case of Paganica fault and April 6th, 2009 earthquake, components of the displacement vectors (\mathbf{d}), are all equal, negative and d_x and d_y are estimated too less than d_z (§5.2). By subtracting common terms of Equations 25 and 26, it is resulted:

$$r_{Des.} > r_{Asc.} \quad (27)$$

and the absolute value of difference is equal to:

$$|2v_x \cdot d_x| \quad (28)$$

Equation 27, emphasises that the difference between maximum subsidence points in the satellite LOS direction, should be more than what was observed in this study. This is due to the different spanning days of the ascending and descending pairs and the movement of deformation after the main shock. While the ascending pair spans 35 days (including nine days after the main event), the descending pair spans 70 days (including six days after the main event). Therefore, although mathematically the descending pair should show much more subsidence in the satellite LOS direction in comparison to the ascending pair, the ascending pair spans three days more during the post-seismic relaxation time, and consequently the difference between the ascending and descending pairs, is decreased.

5.1.2 ALOS PALSAR data set

The InSAR technique was applied on two coseismic and interferometric pairs of ALOS PALSAR images, listed in Table 19, all acquired in fine resolution imaging mode, fine scan (FS) and L1A processing level.

Pair no.	Orbit	Track	Acquisition date/ Mode	Pass	B_{\perp} ¹	Height ambig. ²
1	17706	840	2009/05/21/ FBS	Asc.	-355 m	-162 m
	13009		2008/07/03/ FBD			
2	17283	830	2009/04/22/ FBS	Asc.	202 m	285 m
	13257		2008/07/20/ FBD			

Table 19: ALOS PALSAR image pairs for interferometry

These two pairs cover extents of the epicentral area spatially well and have temporal baselines of 322 days for the first and 276 days for the second pair. They also bracket the two main after-shocks (see §3.2.2 and Table 31 in Appendix B, for the list of after-shocks).

The raw data in Fine Beam Dual-polarization (FBD, 14 MHz) mode was converted to Fine Beam Single-polarization (FBS, 28 MHz) mode, and then was ingested to SLC format as well as scenes in FBS mode, using precise orbits information available in the PALSAR image leader files to remove orbital phase signature (see §4.1.2.2). This conversion has been recommended by Fielding, 2008b, and according to this reference, the interferograms made from the FBD to

1 Refined using the unwrapped phase and the topography.

2 Calculated from ancillary data files provided in header of images using Equation 10 in Chapter 2.

FBS conversion have lower noise than the interferograms made from the FBS to FBD conversion.

The average of the DC, was calculated separately for the images of each pair. The amount of azimuth spectrum overlap for filtering are shown in Figures 84 and 85 in Appendix A, for the first and the second pairs, respectively. In these figures, both scenes of each interferometric pairs have the same DC shift pattern, except for the first lines in the first pair. In this pair, the image acquired on May 21th, 2009 (see Figure 84 in Appendix A), shows some variations between line 0 and 130. Decorrelation of the resulted interferogram (in its first lines in Radar coordinate system), is the direct effect of this variations in DC. The problem was solved by swapping scenes order in the interferometric pair. This method does result in phase to be the negative of the range change and to compensate it, phase was multiplied by -1 to convert back the negative range change to the positive.

Following this, tie points were matched between images of each pair and interferograms and coherence files were made. Figures 86 and 87 in Appendix A, show distribution of range and azimuth offsets versus range and azimuth samples for the first and the second interferometric pairs, respectively. These figures show that automatically selected tie points have a good spatial distribution over scenes and this shows a good quality of image matching.

In the same way as for the ENVISAT ASAR data set, the interferograms were corrected from topographic phase signature, and then were georeferenced using ASTER GDEM. The remained fringe system is mainly related to the L'Aquila earthquake deformation, even though some residual fringes which might be due to atmospheric artefacts, are present particularly in western parts of the city of L'Aquila. However, their amplitude is visually estimated less than a fringe, which should not affect the deformation fringe pattern significantly. Figures 29 and 30 show the first and the second coseismic ALOS PALSAR interferograms in ascending orbits, respectively.

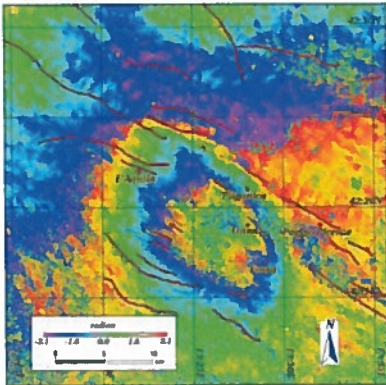


Figure 29: PALSAR interferogram for the first pair (09/05/21-08/07/03)

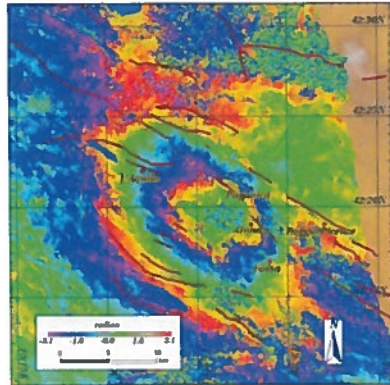


Figure 30: PALSAR interferogram for the second pair (09/04/22-08/07/20)

The structure of fringes is relatively simple and displays a one lobe pattern on hanging-wall and less than one fringe on the foot-wall of the the Paganica fault. The interferograms show an

asymmetric gradients of deformation in the satellite LOS direction on the hanging-wall with the greatest gradients to the north-east of the lobes.

Two clear fringes are seen in Figures 29 and 30, corresponding to 24 cm elongation in LOS direction. This elongation, with respect to the geometry of the fault, is interpreted as subsidence on the hanging-wall, equivalently consistent with a dip-ward motion of the fault.

The centre of fringe systems in the first and the second pairs are slightly different. The centre of the first interferogram is placed about 2 km far on the south-east of the second interferogram. This is, as explained in § 5.1.1, due to different temporal baselines of interferograms and the post-seismic relaxation. The first interferogram spans 29 days more than the second interferogram, and during this time slot, the point with maximum deformation still has moved toward south-east, parallel to L'Aquila- Poggio Picenze axis, with the calculated rate of ~ 0.07 km/day. This shows that the post-seismic relaxation is decreasing significantly, in comparison to the calculated rate of the movement between April 9th and April 15th obtained from ENVISAT ASAR interferograms.

Calculated baselines from orbits, were refined using the unwrapped phase and the topography in the Radar coordinates, and then was used for calculation of ambiguity of height, presented in Table 19. Accuracy of ASTER GDEM used for this process, is less than the height ambiguities of both pairs (see Table 12 in Chapter 4). This shows contribution of topographic residues are lower than one fringe (in proportion).

ALOS PALSAR interferograms show higher quality, and fringes are closed. The corresponding coherence maps (Figures 31 and 32) show higher values (more white patches), in comparison to coherence maps of ENVISAT ASAR (Figures 21 and 22).

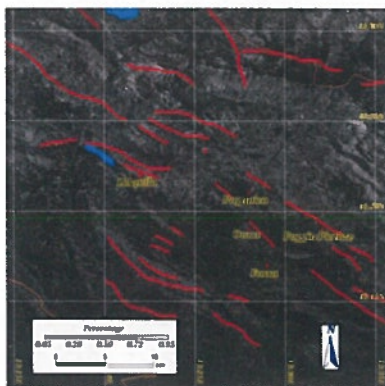


Figure 31: coherence map of the first ALOS PALSAR interferogram

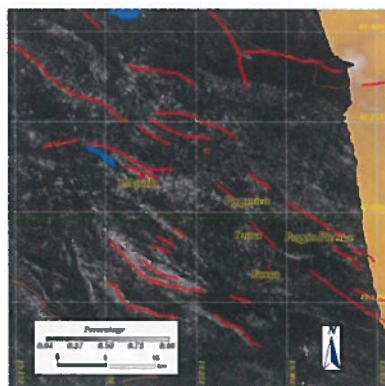


Figure 32: coherence map of the second ALOS PALSAR interferogram

The better quality of ALOS PALSAR interferograms is related to longer wave length of the sensor: waves with longer length can penetrate more. While NDVI map (Figure 33) shows presence of vegetations all over the area, less decorrelation is seen in resulted interferograms.

ALOS PALSAR has higher incidence angle (in comparison to ENVISAT ASAR), and is affected less by topography. Figure 34, shows the slope map in which, areas with the slope more than ALOS PALSAR incidence angle (35°), are highlighted in blue. The blue patches show the area affected by shadow and layover, because slope $>$ incidence angle. In comparison to the ENVISAT ASAR slope map (Figure 24), this figure shows less shadow and layover prone area over the mountains. So, shadow and layover phenomena are less expected in ALOS PALSAR interferograms, as it is seen.

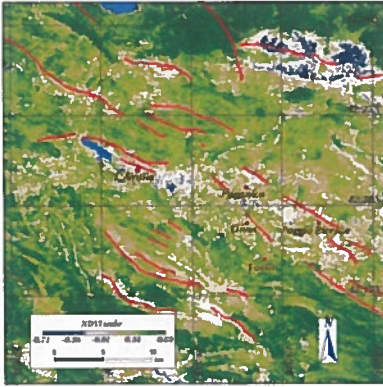


Figure 33: NDVI map

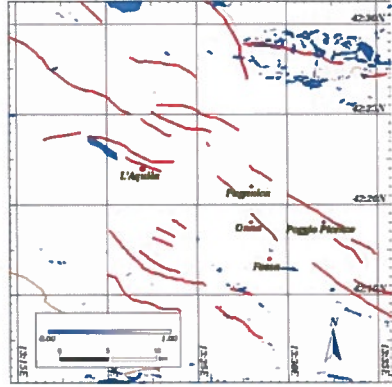


Figure 34: Slope map for PALSAR

Since the incidence angle for the PALSAR image data set is 35° , the technique is more sensitive to vertical rather than horizontal displacements. Also because of the higher incidence angle, ALOS PALSAR data set has a bigger horizontal component in east-west direction than ENVISAT ASAR (see Table 5 in Chapter 2) and consequently, it is more suitable for revealing significant horizontal displacement in this direction by the SCT (compare with sensitivity vector of ENVISAT ASAR; see Table 3 in Chapter 2).

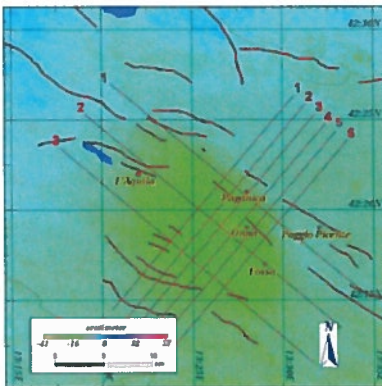


Figure 35: Unwrapped interferogram of the first ALOS PALSAR pair

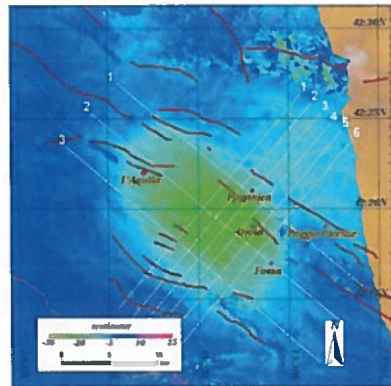


Figure 36: Unwrapped interferogram of the second ALOS PALSAR pair

Both of the ALOS PALSAR interferograms were unwrapped with Snaphu software (see §4.1.3.1) and converted to displacement map in the satellite LOS direction, shown in Figures 35 and 36.

Deformation was measured from ALOS PALSAR unwrapped interferograms along the same profiles and cross sections of the ENVISAT ASAR unwrapped interferograms, and results are shown in Figures 88 and 89 for the first, and in Figures 90 and 91 for the second interferometric pairs, in Appendix A.

In terms of subsidence pattern, the profiles are in agreement. But high frequency variations are seen in profiles and cross sections of the both interferograms, which are due to unwrapping errors and noise. On the contrary, the profiles and cross sections from the ENVISAT ASAR data set (see Figures 75 to 78 in Appendix A) show less variations, in comparison to the ALOS PALSAR data set. In this noisy condition, minimum subsidence and maximum uplift are affected by local variations of single pixels, and do not show true values.

For noise reduction, several techniques have been proposed in the literature to improve the quality of interferograms such as multi-look processing, pivoting mean/ median filtering and Lee filter (Meng et al., 2006). In this study, the 'Enhanced Lee filter' was applied on both unwrapped interferograms to reduce the effect of local extrema (maxima and minima). Speckle effect in Radar imagery is reduced by this filter, while texture information is preserved simultaneously. Lee filtering is a standard deviation based (σ) filter that filters data based on statistics calculated within individual filter windows. Unlike a typical low-pass smoothing filter, the Lee filter and other similar sigma filters preserve image sharpness and detail while suppressing noise. The pixel being filtered is replaced by a value calculated using the surrounding pixels (Lee, 1980). The filter has been adapted from Lee filter and uses local statistics (coefficient of variation) within individual filter windows (Lopes et al., 1990).

Noise variation coefficient (C_u) and its maximum threshold (C_{max}) for the enhanced Lee filter were calculated using the following formulae:

$$C_u = 0.523 / \sqrt{L} \quad (29)$$

and

$$C_{max} = \sqrt{1 + 2/L} \quad (30)$$

where, L is the number of looks of the Radar image (Lopes et al., 1990). For this case, the Enhanced Lee filter were applied with kernel size of 13^1 , $C_u = 0.234$ and $C_{max} = 1.183$ for $L = 5$.

Figures 37 and 38, compare the results from the filtered and unfiltered unwrapped interferograms along profiles number 2 in Figures 35 and 36, which pass almost from the centre of fringe systems. As shown in both figures, the profiles from filtered unwrapped interferograms (the green graph), are quite smooth (no local variations are seen) and fit to the profiles from unfiltered ones (the purple graph). The new profiles give more realistic values for the deformation.

Before applying the filter, maximum 28.9 cm and 30.2 cm subsidence and 2.4 cm and 1.1 cm uplift in the satellite LOS direction were observed on the profiles of the first and the second pair, respectively (see Figures 88 and 90 in Appendix A). On the other hand, maximum 31.2 cm and 30.0 cm subsidence and -3.4 cm and 1.4 cm uplift in the satellite LOS direction,

1 Kernels with different sizes were tested, and this size of the kernel fits better to the data set.

were detected on the cross sections of the first and the second pair, respectively (see Figures 89 and 91 in Appendix A). The cross sections correspond to the trace of the Paganica and Aterno-Poggio Picenze faults. They show that the subsidence has started from common trace of these faults.

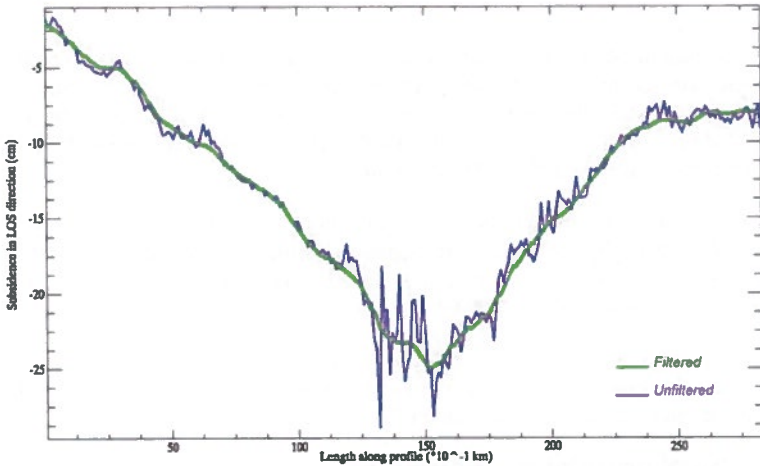


Figure 37: Comparison between profiles from filtered and unfiltered unwrapped interferograms for the first ALOS PALSAR pair

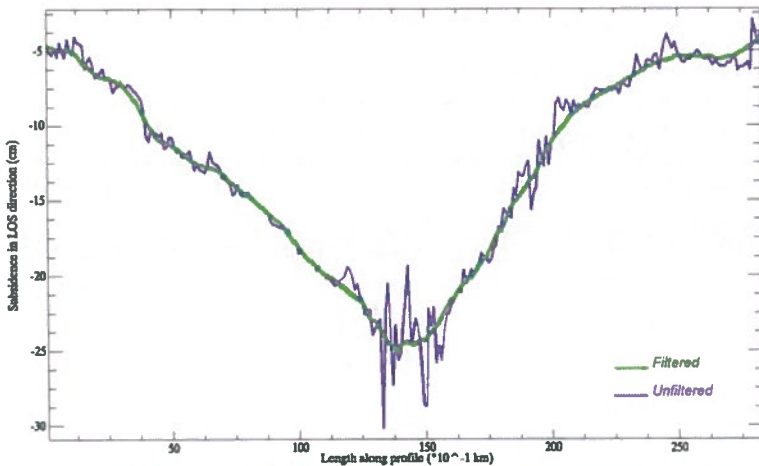


Figure 38: Comparison between profiles from filtered and unfiltered unwrapped interferograms for the second ALOS PALSAR pair

After applying the filter, maximum 25.0 cm subsidence in the satellite LOS direction is measured on both profiles of the first and the second pairs (Figures 37 and 38).

Spatial analysis showed that maximum 25.6 cm and 25.1 cm subsidence in the satellite LOS direction occurred in two separate points, one at (42.319°N, 13.451°E) about 1.8 km, and the other at (42.325°N, 13.431°E) about 4.0 km to the north-west of Onna village which was highly devastated during the April 6th earthquake (GEER, 2009). ALOS PALSAR interferograms do not show uplift on the foot-wall of the fault in the limits of the profiles, and consequently were not measured.

The results from the ALOS PALSAR data set are strongly supported by the results from ENVISAT ASAR data set; however, ALOS PALSAR interferograms show less values for subsidence in the satellite LOS direction. While maximum 25.6 cm and 25.1 cm subsidence in the satellite LOS direction are observed from ALOS PALSAR data set, maximum 26.1 cm and 28.1 cm are reported from the ENVISAT ASAR data set.

The difference is due to smaller vertical component of ALOS PALSAR sensitivity vector (v_z in Equation 24) and negligible horizontal displacement on the ground surface (d_x and d_y in Equation 24). For this reason, ALOS PALSAR interferograms are less sensitive to vertical displacements in comparison to ENVISAT ASAR data set.

Spatially, the maximum subsidence in the satellite LOS direction was measured (from both of the data sets) somewhere between 1.5 km and 4.0 km far from the village of Onna to the north-west direction (see Figure 70 in Chapter 6).

5.2 Sub-pixel correlation technique

SCT was used in this research to investigate the horizontal displacements caused by the April 6th, 2009, earthquake in L'Aquila area. Both SAR and optical image data sets were employed and horizontal displacements in Range/ Azimuth (for SAR data set) and in west-east/ south-north (for optical data set) directions were computed, respectively.

5.2.1 ENVISAT ASAR data set

SCT was applied on two coseismic pairs of ENVISAT ASAR images, all acquired in image mode, IS2 and L0 processing level with minimum available perpendicular baselines, listed in Table 20. In this condition (i.e. same incidence angle and short baselines), the speckle signature remains similar on both images and stereoscopic effect is avoided, as much as possible.

Pair no.	Orbit	Track	Acquisition date	Pass	B_{\perp}^1
1	38531	401	2009/07/13	Asc.	44 m
	36026		2009/01/19		
2	39211	079	2009/08/30	Des.	28 m
	26185		2007/03/04		

Table 20: ENVISAT ASAR image pairs for SCT

The two pairs were selected from twelve other pairs, because they cover the spatial extent of the study area and have the minimum available perpendicular baselines.

Both the phase and amplitude of SAR images were used to generate offsets with azimuth and range window size of 100 and 20 pixels, respectively (the spatial resolution of this tech-

1 Refined using the unwrapped phase and the topography.

nique depends on the size of the correlation window). Images were ortho-rectified using ASTER GDEM (see §4.1.2.1).

Unrealistically, outputs of SCT are quite noisy and the pixel values are dispersed and range between extremely high values (e.g. 200 times larger than length of the correlation window). Figures 92 and 93 in Appendix A, show histograms of the ascending and the descending pairs in azimuth and range directions, respectively. The histograms show that majority of pixels are accumulated around zero.

Highly dispersed values for displacements in azimuth and range, can be due to temporal changes (e.g. variation in vegetation coverage, soil moisture and so on) that affect SAR imagery. The other reason would be length of baselines which are still long and lead to domination of speckles. The later reason could not be examined further, because there was no other ENVISAT ASAR coseismic interferometric pair with a shorter baseline, in the ENVISAT ASAR catalogue (see §6.2 for discussion about the spatial baseline).

Anzidei et al., 2009, have studied the earthquake of April 6th using GPS observations. The GPS data set for this study includes observations of forty permanent sites, ten days before and two days after the main shock of April 6th (i.e. until the first significant after-shock on April 7th, 17:47 UTC). This selection, minimizes the effects of cumulated deformation caused by the after-shocks that occurred after the main shock (Anzidei et al., 2009), even though contribution of the post-seismic deformation till April 15th, has been measured about 7% of the main shock moment release by Cheloni et al. (manuscript in preparation, 2009, from Walters et al., 2009).

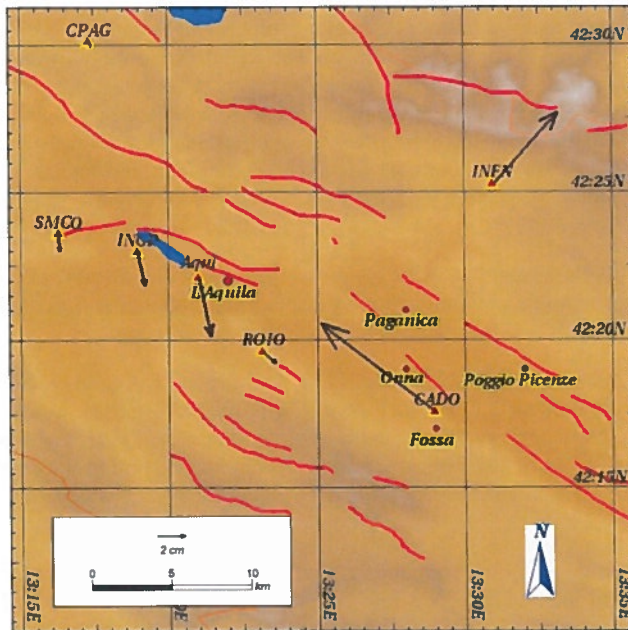


Figure 39: Coseismic horizontal displacement of permanent GPS stations in L'Aquila (modified from Anzidei et al., 2009)

Figure 39 shows the measured coseismic horizontal displacements in near field GPS stations (from Anzidei et al., 2009), overlaid on the DEM of the study area. In this figure, the red triangles show position of GPS stations. According to this study, the horizontal displacement of 7.03 ± 0.36 cm toward the north-east direction has been observed at INFN station, which is aligned to the foot-wall motion of the fault. The maximum coseismic horizontal surface displacement, has been detected at CADO station, equal to 10.39 ± 0.45 cm toward the north-west direction. The other sites around the epicentre show minor (a few centimetres) displacements. The relevant numerical values of the displacement vectors are presented in Table 37 in Appendix B.

The figure shows that GPS stations in L'Aquila are not located sufficiently dense to give a clear spatial pattern of the coseismic displacements. While horizontal displacement vector at INFN is aligned to direction of foot-wall motion, the displacement vector in CADO is toward north-west and is not aligned with the expected direction of the hanging-wall motion (toward south-west). Other stations are almost oriented to the south, except in the SELL which is toward south-west (not shown in Figure 39, because it is far from the main event epicentre; see Table 37 in Appendix B for numerical values).

The measured values for horizontal displacements from the study of Anzidei et al., 2009, are still smaller than minimum detectable horizontal displacement by using ENVISAT ASAR data set (20 cm in azimuth and 1.0 m in range; see Table 14 in Chapter 4). However, measuring surface displacements using GNSS observations is a point-wise technique, and gives changes only on the antenna installation point.

Based on this study and minimum detectable displacement from the ENVISAT ASAR data set, an interval between -30 cm and +30 cm for horizontal displacement in azimuth direction and between -150 cm and +150 cm (five¹ times bigger than the interval in the azimuth direction) for horizontal displacement in range direction, were assumed. All the values out side of these intervals (which are supposed to be either noise or artefacts) were masked out and the results are shown in Figure 40 and Figure 41 for the ascending pair and Figure 42 and Figure 43 for the descending pair, respectively in azimuth and range directions, superimposed on the DEM.

Neighbouring pixels (in azimuth offsets) are changing from one extreme of the displacement interval to the other extreme randomly, and no displacement pattern is observed in the results, neither in azimuth direction (which has a finer resolution) nor in range.

The big aggregation of pixels on the ascending pair, around L'Aquila extended toward east (enclosed with white dashed line box in Figure 40), is related to urban area of L'Aquila city. Also some pixels have aggregated on south-west of Paganica fault (enclosed with yellow dashed line box in the Figure 40). This group of pixels are located on farmlands of the village of Paganica and might be resulted from temporal decorrelation between acquisition of the two images.

The offsets, in range direction from both ascending and descending passes, do not show any pixels in the assigned interval, except a few in the ascending pair to the west of Onna. This is due to five times coarser resolution of ENVISAT ASAR image pixels in the range direction.

1 Equals to number of looks for ENVISAT ASAR data set.

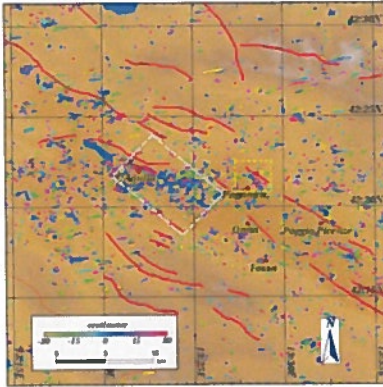


Figure 40: Azimuth offset of the ENVISAT ASAR ascending pair

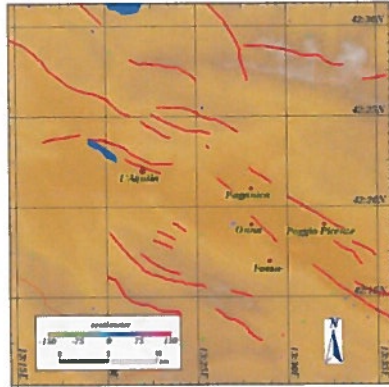


Figure 41: Range offset of the ENVISAT ASAR ascending pair

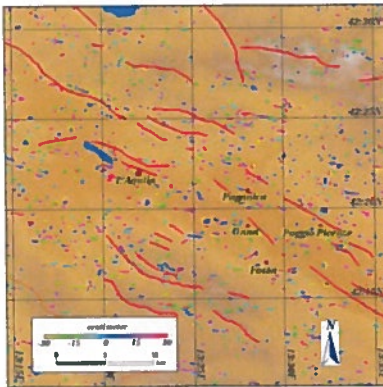


Figure 42: Azimuth offset of the ENVISAT ASAR descending pair

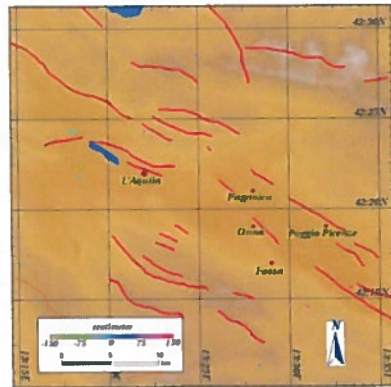


Figure 43: Range offset of the ENVISAT ASAR descending pair

The offset from ascending pair, which has shorter temporal (175 days in comparison to 910 days) and longer spatial (44 m in comparison to 28 m) baseline, shows more pixels in comparison to the descending pair. This result shows that the technique is more sensitive to spatial baseline rather than temporal (see §6.2 for discussion). However, the longer the temporal and spatial baselines in SAR SCT, the stronger is the noise.

The corresponding coherence files for the ascending and the descending pairs, are shown in Figure 44 and Figure 45, respectively. By comparing these figures with Figures 40 to 42, no meaningful relation between the displaced points and high coherent points (white patches) are seen; but in south-west of the Paganica fault, the ascending pair shows higher coherence (some white patches are seen), where the more pixels are aggregated on the corresponding offset file. This can be another evidence that shows the resulted displacement points are actually noise.

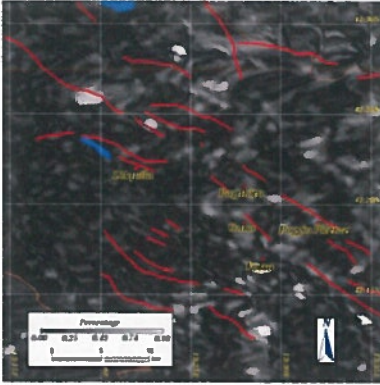


Figure 44: Coherence map for the ascending pair

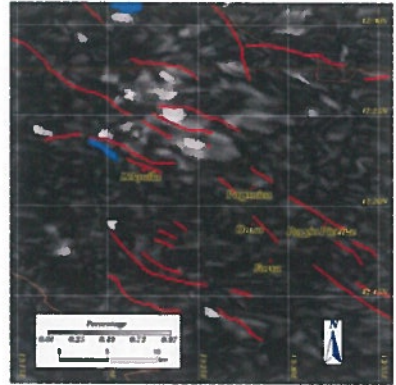


Figure 45: Coherence map for the descending pair

Absence of any displacement pattern is due to either not sufficiently fine spatial resolution of ENVISAT SAR images, which is insufficient to detect small horizontal displacements, or insignificance of the induced horizontal displacements by the earthquake, due to the normal structure of the causative fault. Also, it can be inferred that the causative fault either is not ruptured or the rupture is not significant enough to be detected by the ENVISAT SAR data set (see §6.2 for discussion).

5.2.2 ASTER data set

SCT applied on two image pairs of ASTER in L1A processing level and HDF format, listed in Table 21. Spatially, the whole area affected by the earthquake is not covered completely by one of these image pairs, and therefore, two pairs were chosen. While the first pair covers the northern parts of the area, the second pair covers the epicentre and the southern parts.

The pairs are cloud free with minimum baseline to height ratio (B/H) to avoid stereoscopic effect between scenes. For reducing the solar illumination difference effects, images of each pair were selected at the same time of the acquisition dates (the time differences are in the order of a few seconds). No any other suitable image pair (i.e. cloud free, with minimum B/H ratio and bracketing the earthquake) was available to apply the technique.

Pair no.	Scene ID	Acquisition date	B/H ¹
1	2017273508	2003/09/19	0.0038
	2075058906	2009/07/17	
2	2017273494	2003/09/19	0.0038
	2075058903	2009/07/17	

Table 21: ASTER image pairs for SCT

¹ Calculated from ancillary data files provided in header of images.

A pre-processing of the radiance correction is necessary for ASTER images. Although all bands of ASTER images are supported by the COSI-Corr software, the band VNIR 3N was selected, as it is recommended in the user's manual of the software (Ayoub et al., 2009).

The pre-earthquake images in each pair were co-registered and ortho-rectified using ancillary data provided with image files and ASTER GDEM, respectively. Sinus cardinal (Sinc) resampling kernel was used to reconstruct the images according to mapping matrices defined in orthorectification step (see §4.2.2.2) with the kernel size equals to 25^1 . By this way, the absolute precision of displacement maps will be of the same order of the used DEM.

To co-register the post-earthquake images, 30 tie points were selected initially between images of each pair. Tie points were spread all over the images, but mostly far from the area which was expected to the occurrence of maximum displacements. Then points with high RMSE values were removed and finally 21 and 22 points were remained for the first and the second pair, respectively. In the next step, the selected tie points were converted to GCPs and were optimized with the frequential correlator. In this case, the maximum placement error which is allowed on initial GCPs corresponds to the half of the correlation window size (Ayoub et al., 2009). Table 22 shows first degree RMSE values for initial and standard deviation values for optimized GCPs for each image pair.

Pair no.	Initial RMSE	Standard deviation
1	0.782	2.807
2	0.690	3.451

Table 22: RMSE for initial and standard deviation for optimized GCPs

The raw post-earthquake images then transferred into the already ortho-rectified pre-earthquake images using optimized GCPs and the same DEM as was used for pre-earthquake images.

Eventually, the two co-registered and ortho-rectified images in each pair, were correlated using frequential correlator engine with the parameters listed in Table 23. Different values tested for these parameters and the table shows the values for the best obtained displacement model for each pair.

Correlation parameters	First pair	Second pair
Window size (pixel)	32	64
Step (pixel)	4	8
Robustness iteration	2	2
Mask threshold (%)	0.90	0.90

Table 23: Correlation parameters for applying SCT on the ASTER images

Offsets in west-east and south-north directions (after de-striping) and displacement vector field map, all superimposed on active faults map and DEM of the area, are shown respectively in Figures 46, 47 and 48 for the first pair and Figures 50, 51 and 49 for the second pair.

1 Kernels with different sizes were tested, and the best result obtained by this size.

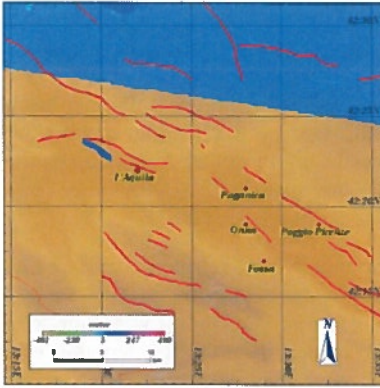


Figure 46: West-east offset of the first ASTER pair

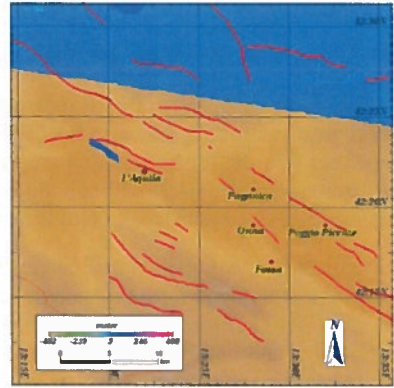


Figure 47: South-north offset of the first ASTER pair

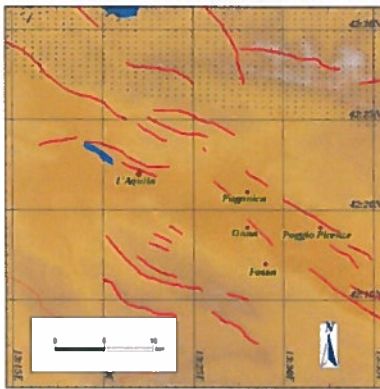


Figure 48: Displacement vectors of the first ASTER pair

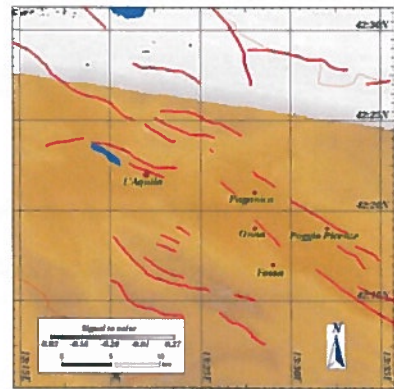


Figure 49: SNR channel of the first ASTER pair

The offsets do not show any meaningful pattern for horizontal displacements, neither in west-east, nor in south-north direction. This result is supported by results from the ENVISAT ASAR data set. Coarse resolution of the used image data set, is the main barrier against detection of small horizontal displacements. Temporal variation mainly due to changes in vegetation, is another important obstacle for optical SCT.

While according to study of Anzidei et al., 2009 (§ 5.2.1 for more details about this study), maximum coseismic horizontal displacement of $10.39 \pm 0.45 \text{ cm}$ observed in the south-eastern of the village of Onna, the minimum detectable horizontal displacement which can be achieved by ASTER data set is about 75 cm (see Table 15 in Chapter 4). Still this is much coarser than the maximum observed horizontal displacement by the GPS data set. In other words, it can be inferred that the real coseismic horizontal displacement was not significant enough to be detected by this data set and another image data set with sufficiently fine pixel resolution, is strongly needed.

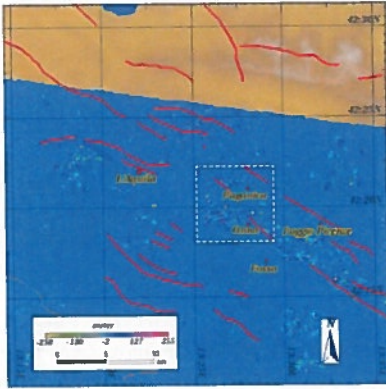


Figure 50: West- east offset of the second ASTER pair

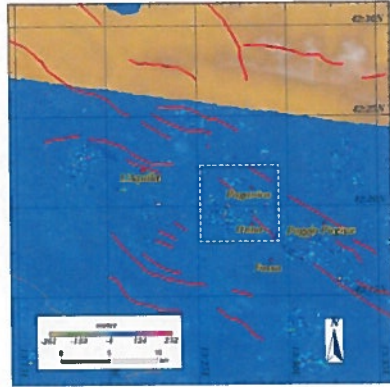


Figure 51: South-north offset of the second ASTER pair

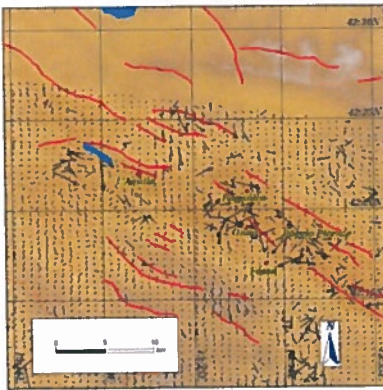


Figure 52: Displacement vectors of the second ASTER pair

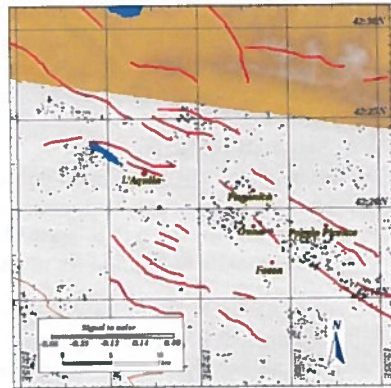


Figure 53: SNR channel of the second ASTER pair

Some patches of aggregated points are seen in the offsets of the second pair. To find the reason, offsets were overlaid on land cover map of the area using GIS software (see Table 32 in Appendix B). Overlay analysis showed that these patches are matched with large farmlands of the villages of Paganica and Onna and they are resulted from temporal variations of vegetations in the area, even though they are distributed between Paganica and Pettino faults and also south-western of Pettino fault (the white dashed line box on the Figures 50 and 51), where the maximum horizontal displacements are expected. Other patches of aggregated displaced points were investigated in the same way and it was observed that all of them were related to other big farmlands in the area.

Displacement vectors corresponding to these points (Figures 48 and 49 for the first and the second pairs, respectively) show a dispersed pattern; means displacement vectors with different length and directions without any detectable pattern. These vectors are not coincident with displacement vectors observed from GPS data sets (Figure 39).

Signal to Noise Ratio (SNR) channels of the correlated files, are shown in Figures 49 and 53 for the first and the second pairs, respectively. SNR channels are used for quality assessment of measurements, and pixels with low SNR values, practically 90 percent (Leprince, 2008), are considered as outliers.

Low SNR values for the whole images (maximum 0.27 for the first and 0.40 for the second pair), show low quality of coherence or high amount of variations between two images of each pair. Because the area is dominantly covered by vegetation, this is due to temporal variation of vegetation between two image acquisitions. While SNR value is generally low for the whole image extents (Figures 49 and 53), it is lower yet and even negative for the aggregated points. This is another evidence that these points can not be considered as a true result for real horizontal displacements.

Regardless of the noisy aggregated points, other parts of the offsets show zero horizontal displacements. This is shown not only by offsets maps, but also by quivers of displacement vector maps (Figures 48 and 52).

Figures 94 and 95 in Appendix A, show histograms of the second ASTER pair for offsets in west-east and south-north directions, respectively. In this histograms the majority of pixels are accumulated around zero. This is supported convincingly by the previous results and is the most important finding from this data set. In other words, no significant horizontal displacements (larger than 75 cm) was observed in the study area.

5.3 Inversion problem

Geometry of the fault and slip distribution on the fault plan were inferred from surface deformation measurements by using a two-step procedure, namely: neighbourhood algorithm (NA) and linear least square (LS) inversion. The shear dislocation is assumed in a uniform elastic earth model, using Okada analytical solution for deformation (Okada, 1985).

The two coseismic unwrapped interferograms of the ENVISAT ASAR data set (obtained from SAR interferometry in this research in §5.1.1), were modelled using a direct stochastic method based on the NA (see §4.3.1) and the standard weighted LS inversion method (see §4.3.2). Models were optimized by minimizing the RMSE misfit and maximizing correlation between the observed and predicted coseismic unwrapped interferograms.

5.3.1 NA algorithm

To estimate the overall geometry of the fault, the NA algorithm was applied on the two coseismic unwrapped interferograms of the ENVISAT ASAR data set (§5.1.1). Contribution of the post-seismic deformation in the interval of coseismic interferograms, measured about 7% of the main shock moment release (D. Cheloni et al., manuscript in preparation, 2009, from Walters et al., 2009) and equivalent to less than one fringe, was neglected. Unwrapped interferograms were also checked for null deformation zones in the far field to see if they are not affected by any constant offset or gradient (deformation was estimated to zero).

First, a model space of 7 parameters including: 1- position of centroid of the fault plane along strike (relative to mid-fault point), 2- position of centroid of the fault plane along dip (relative to mid-fault point), 3- length of the patch of uniform slip, 4- height of the patch of the uniform slip, 5- Poisson's coefficient, 6- strike slip component, and 7-dip slip component, were defined. While direct interpretation of geodetic data sets, makes it possible to find a proper interval for each parameter, not too much constrains were imposed for testing the NA approach.

The complete interferograms (100 km by 100 km) and corresponding coherence files were projected onto UTM coordinate system and sub-sampled onto a 100 m regular grid in order to reduce computational cost, and then the deformation area (50 km by 50 km) was subset. Although some high frequency patterns are removed by sub-sampling, specially along the fault trace, the main deformation patterns are remained (Peyret et al., 2007).

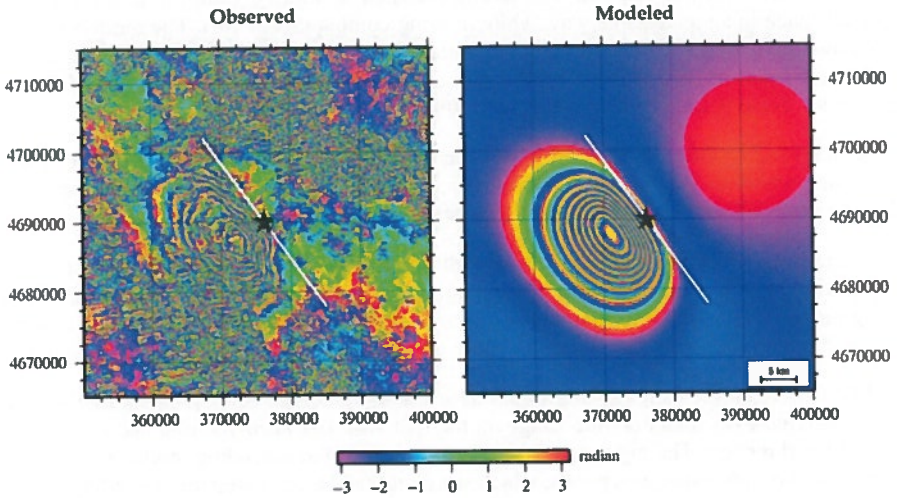


Figure 54: Observed and optimised-modelled interferograms for the ascending pair from the NA inversion

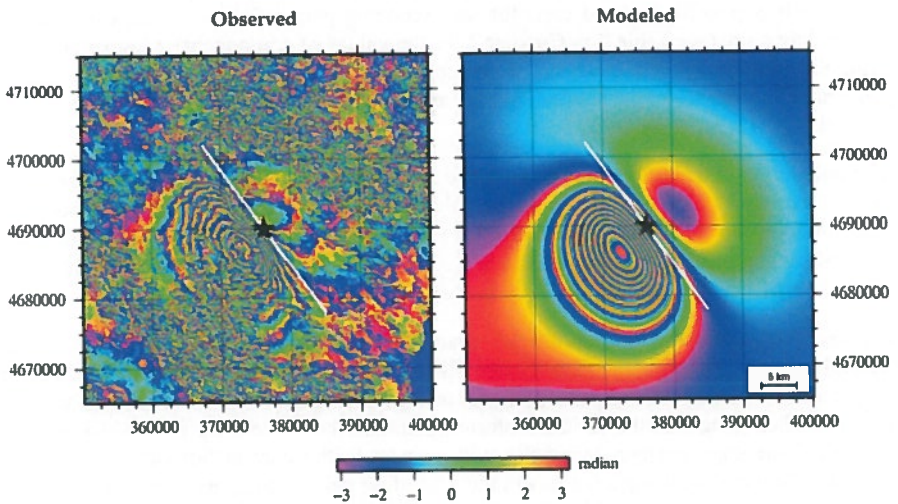


Figure 55: Observed and optimised-modelled interferograms for the descending pair from the NA inversion

The inversion procedure makes use at both stages of weighting matrices for each geodetic data set which are a-priori covariance matrices and show the confidence for each measurement (Peyret et al., 2007). For the InSAR data set, corresponding coherence estimation which is mainly effective for removing insignificant pixels, was used and pixels with the corresponding coherence values of lower than 17%, were rejected.

The NA algorithm was run with two tuning parameters: strike and dip, in order to examine the model space in an analysable way, while limiting computational cost. The models were optimized by minimizing RMSE misfit and maximizing correlation between the observed and predicted interferograms. The RMSE misfit and correlation were computed independently for every model, using R statistical software (R, 2009).

The observed and the optimised-modelled interferograms, are illustrated in Figures 54 and 55, for the ascending and the descending pairs, respectively. In these figures, the white line strikes the assumed fault trace and the star sign shows position of the mid-fault point.

The ascending model (Figure 54) shows eight fringes on the foot-wall, but no fringe on the hanging-wall, equivalent to the observed ascending interferogram. On the other hand, the descending model (Figure 55) shows nine fringes on the hanging-wall and less than one complete fringe on the foot-wall, also strongly compatible with the observed descending interferogram.

While fringes on the hanging-wall of the descending model are correspondent to elongation in the satellite LOS direction, the fringe on the foot-wall is considered as a shortening in the satellite LOS direction. The big red spot on the foot-wall of the ascending model, might be due to aggregation of low coherence pixels, which were masked before inversion modelling.

The pattern of fringes for the ascending model is shortened in south-west direction (roughly perpendicular to the fault trace), while it is extended in this direction for the descending model. This might be due to west-east component of the satellite LOS direction projected on the earth surface, which is positive (toward east) for the ascending pair and negative (toward west) for the descending pairs (see Table 3 in Chapter 2 for the values of component). Figures 56 and 57, illustrate the geometrical interpretation of this concept. In Figure 56, the signs \otimes and \odot show perpendicular trajectories of the satellite to the paper plane, in ascending and descending passes, respectively.

The geometrical parameters of the causative fault and the corresponding RMSE as well as the correlation values for each model and the values obtained from seismological methods from different sources, are summarized in Table 24. In this table, X_c , Y_c and Z_c show coordinates of the fault plane centroid for InSAR models and coordinates of the hypo-centre point for INGV, USGS and GCMT, in the UTM coordinate system.

Figures 58 and 59 show residual interferograms for the ascending and the descending pairs, respectively. The ascending pair has a smaller RMSE misfit and greater correlation values, and in comparison to the descending pair, fits better to the observed model. However, this has led to some unmodelled fringes in the residual interferogram for the descending pair, which might be due to lateral rheology changes (specially with respect to the current post-seismic relaxation movement). The residual fringes are less in the ascending pair, in comparison to the descending pair, which is in agreement with RMSE misfit values. The phase residues are mostly distributed in a zone of 15 km wide and 25 km length around the fault trace.

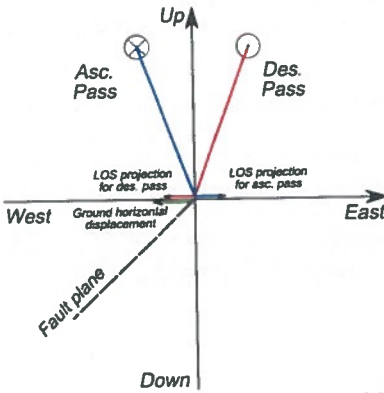


Figure 56: Projection of satellite LOS on the ground surface (side view)

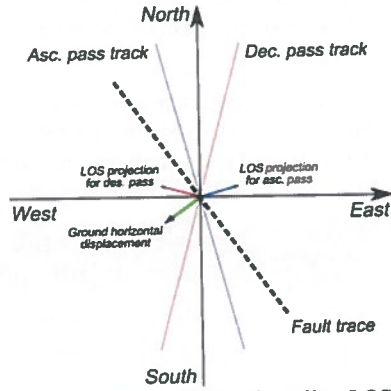


Figure 57: Projection of satellite LOS on the ground surface (top view)

In the uniform slip NA solution, the causative fault strikes 144° along north-west to south-east direction and dips 54° toward the south-west. The fault has a significant overall normal dip slip with a small component on the strike direction.

Walters et al., 2009, have studied the April 6th, L'Aquila earthquake using InSAR, GPS observations and body-wave seismology to determine the independent source parameters of the causative fault. They have jointly inverted InSAR data set for uniform slip on a rectangular fault plane in Okada elastic half space, using a Powell optimization algorithm to find the best-fitting combination of the fault parameters.

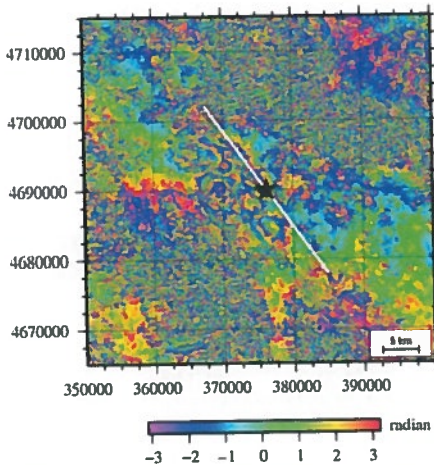


Figure 58: Residual interferogram for the ascending model from NA inversion

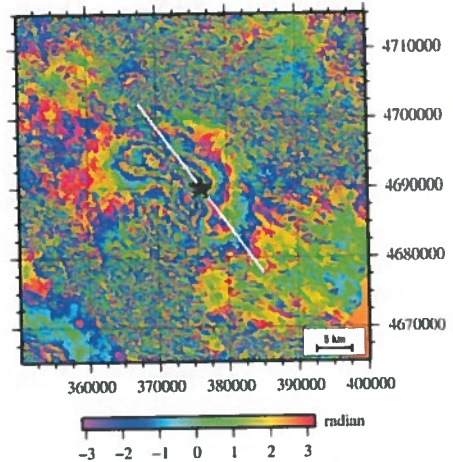


Figure 59: Residual interferogram for the descending model from NA inversion

Values found in this research are similar to values found by Walters et al., 2009, presented in Table 25. These two sets of source parameters are only discrepant in slip and length of the fault for descending pairs.

Geometrical parameters values from seismological methods support the InSAR models, but there is a big difference between the InSAR solutions and the seismological solutions. While the InSAR models (from this research and the study of Walters et al., 2009) show strike of 144° for the fault, the seismological models suggest the fault plane strikes between 120° and 147°.

Source parameter	InSAR Asc. pair	InSAR Des. pair	INGV QRCMT ¹	USGS CMT ²	GCMT ³
Strike (°)	144	144	147	122	120
Dip (°)	54	54	43	53	54
Rake (°)	-93.49	-85.43	-88	-112	-113
Strike slip ⁴ (m)	-0.05	0.08			
Dip slip ⁵ (m)	-0.82	-1.00			
Length (km)	11.565	11.390			
Depth (km)	7.978	7.976	8.8	10	8.8
X_c (km)	371.485	371.468	361.564	374.760	362.410
Y_c (km)	4687.343	4686.699	4686.673	4732.745	4687.767
Z_c (km)	-7.361	-7.901			
RMSE (cm)	1.63	2.41			
Correlation (%)	90.53	86.49			

Table 24: Source parameters for the Paganica fault from InSAR inversion and seismological methods

Figure 60 shows focal mechanisms for the main shock from the InSAR models of this study, study of Walters et al., 2009, and also seismological methods, as well as focal mechanisms for the two main after-shocks from INGV-S4 Project website.

Source parameter	Asc. pair	Des. pair	GPS	Body wave
Strike (°)	144	144	134	126
Dip (°)	54	54	49	52
Rake (°)	-105	-105	-100	-104

- 1 INGV-S4 Project website
- 2 USGS Earthquake Hazards Program website
- 3 GCMT website
- 4 Overall strike slip on the fault plane
- 5 Overall dip slip on the fault plane

slip(m)	-0.66	-0.40	-0.72	
Length (km)	12.2	19	11.1	12
Depth (km)				
X_c (km)	372.220	372.220	374.004	360.762
Y_c (km)	4687.915	4687.915	4690.882	4687.800
Z_c (km)	-7.3	-7.0	-6.7	-4
RMSE (cm)	1.0	1.2		

Table 25: Source parameters for the Paganica fault (Walters et al., 2009)

This figure shows that the epicentres reported from seismological methods are quite dispersed, while all epicentres resulted from the InSAR models are close together. Particularly, the epicentre reported by USGS CMT falls quite outside of the border of this map (not shown in Figure 60).

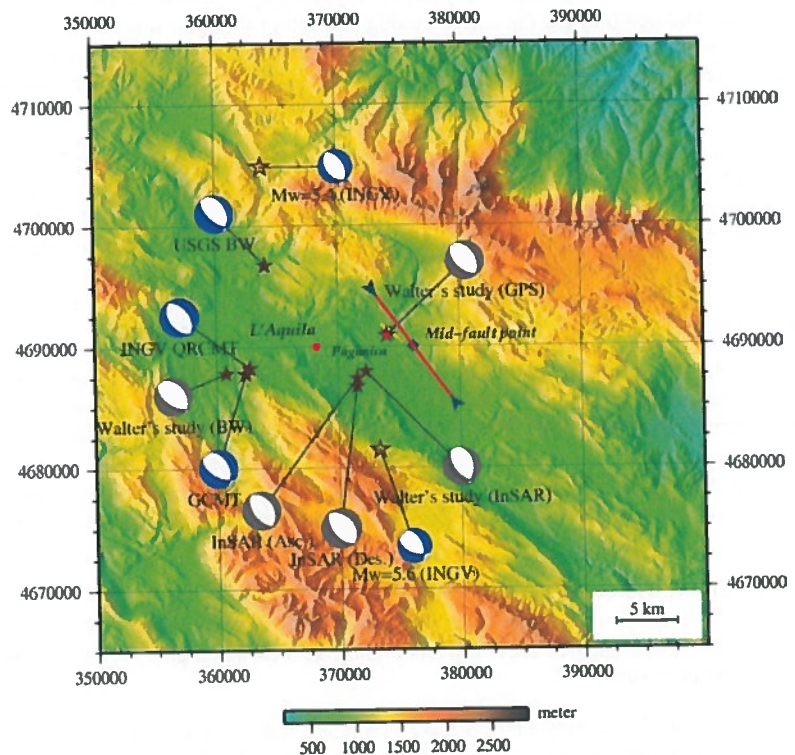


Figure 60: Focal mechanisms and geomorphology of the Paganica fault and the surrounding area

Furthermore, a geomorphological interpretation was done using one LANDSAT 5 TM scene acquired on August 10th, 2009 (scene ID: LT51900312009222MOR00) and ASTER GDEM (see §4.1.2.1) illuminated from west, shown in Figure 60. The approximate trace of the Paganica fault discontinuities, which was derived from the satellite image and shown by a sequence of yellow dots on the figure, gives an average strike of 141°, strongly supporting the inferred strike from the InSAR models. The two large blue arrowheads mark the ends of the predicted fault. The predicted fault projected on the surface (shown by the red line), coincides with the trace of the fault; while it passes from high topography in the north-west, it crosses lower topography further to the south-east.

5.3.2 Linear least square inversion

The same two coseismic unwrapped interferograms of the ENVISAT ASAR data set (§5.1.1 for details), were inverted using the standard weighted linear least square (LS) inversion method (Peyret et al., 2007) for finding distribution of the variable slip on an array of rectangular patches on the fault plane.

To construct the rectangular patches, a grid of nodes was created first, using the geometrical parameters found from the NA inversion model for the geometry of the fault (Table 24), including coordinates of start and end points, dip angle, depth along dip, number of nodes along dip and along strike, and depth of the fault. Even though length of the fault was known from results of the NA inversion, coordinates of the start and the end points of the fault were chosen sufficiently far (30 km in this case) to give enough freedom to the rectangular patches of the fault plane to shake.

Input images of the model were prepared in the same way as it was explained for the NA inversion (§ 5.3.1) with this difference that pixels with corresponding coherence values of lower than 15% were rejected on the hanging-wall area to retain significant pixels. Furthermore, as the major ground deformation is distributed mostly over the hanging-wall, the unwrapped interferograms were completely masked in the foot-wall area of the causative fault (north-east of the fault trace), and the hanging-wall zone was evenly sub-sampled to 400 m spatial resolution to reduce the computational cost.

Eventually, the LS inversion code was run with different values for smoothness and weights for the InSAR data set. Smoothness is defined as the L2 norm of the Laplacian of the slip model. Different smoothness constraints were tested on slip distribution. Decreasing the smoothness parameter leads to solutions with higher geodetic momentum and lower RMSE value (Peyret et al., 2008b). The RMSE misfit between the sub-sampled observed and the modelled unwrapped interferograms, were estimated independently for every model using R statistical software (R, 2009).

Figures 61 and 62 show the observed, optimised-modelled and residual interferograms resulted from the LS inversion method, respectively for the ascending and the descending pairs. In these figures, small white patches show low coherent pixels (lower than 15%) which had been masked before the inversion.

The ascending and descending models have predicted eight and nine fringes, respectively, which is quite in agreement with number of observed fringes (§5.1.1). Some artefacts are seen in both modelled interferograms, mainly located in the north-west of the fringe systems and partially in the centre. Residual interferograms in the north-west might be due to atmospheric arte-

facts, and residual in the centre are assigned to lateral rheology changes with respect to post-seismic relaxation, explained in §5.1.1.

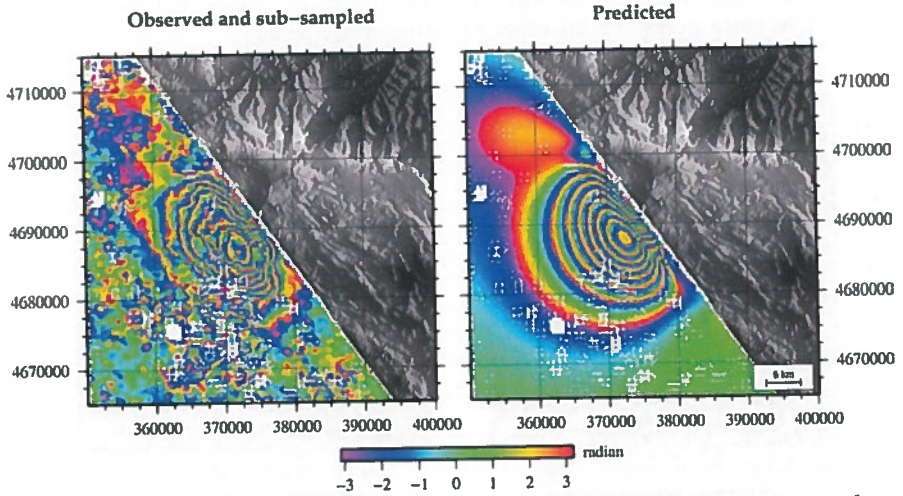


Figure 61: Observed, optimised-modelled and residual interferograms for the ascending pair from the LS inversion

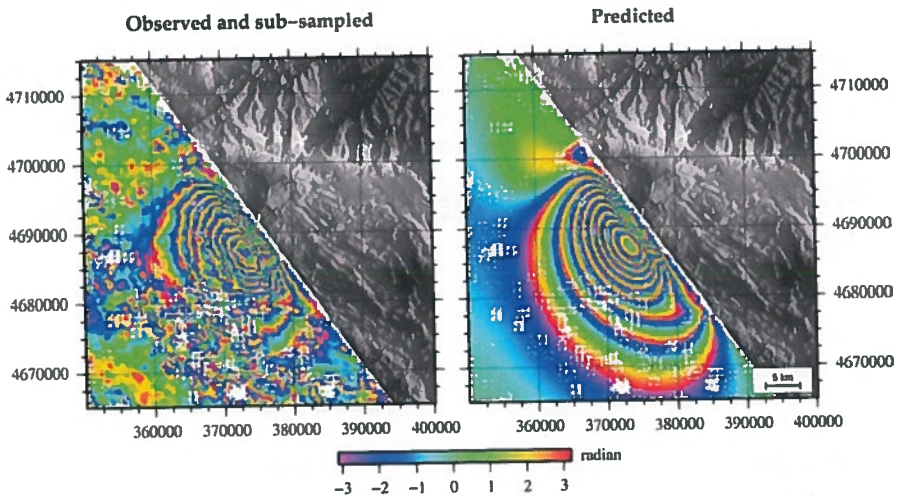


Figure 62: Observed, optimised-modelled and residual interferograms for the descending pair from the LS inversion

The obtained parameters of the LS inversion for the optimised model are summarized in Table 26, and residual interferograms for the ascending and the descending pairs are shown in Figures 63 and 64, respectively. In comparison to results of the NA inversion, the fit to the ob-

served data has improved significantly (the predicted interferograms fit to the observed data better) and the overall RMSE misfit was reduced from 1.63 cm for the ascending and from 2.41 cm for the descending pairs to 0.54 cm and 0.58 cm, respectively. Therefore, less unmodelled fringes are seen in the residual interferograms. This RMSE values provides a reasonable estimates of the noise level which are expected for the interferograms.

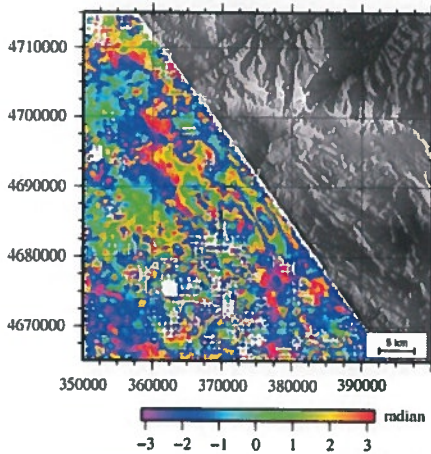


Figure 63: Residual interferogram for the ascending model from LS inversion

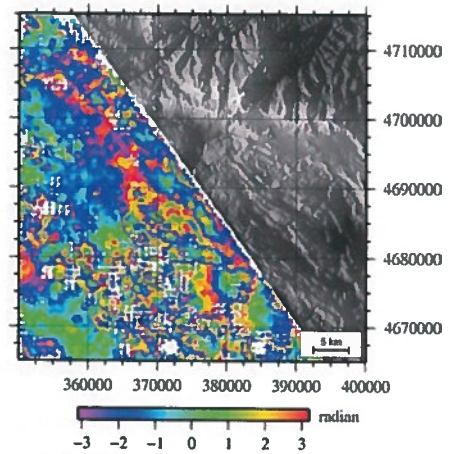


Figure 64: Residual interferogram for the descending model from LS inversion

Figures 65 and 66 show distribution of dip slip on the fault plane resulted from inverting the ascending and the descending pair, respectively. On these figures, the blue star represents the hypo-centre obtained from the corresponding NA inversion which is quite near to the point with maximum dip slip, and strongly supports the results of the LS inversion modelling.

Source parameter	Ascending pair	Descending pair
Max dip slip (m)	1.11	1.26
M_w	6.32	6.49
$M_0 (\times 10^{18} Nm)$	3.80	6.84
V_c^1 (km)	19	19
Z_c^1 (km)	8.25	9.75
RMSE (cm)	0.54	0.58
Correlation (%)	97	97

Table 26: LS inversion model parameters for the Paganica fault

- Coordinates of the hypo-centre on the fault plane (the origin is upper left corner, and in this case north-west of the fault plane)

Dip slip distribution on the fault plane was projected on the horizontal surface, and the trace of the fault was delineated by the red line, shown in Figure 67. This figure shows that the model predicts a small rupture (about 10 cm) along a 2~3 km of the fault trace (between the two blue brackets). This rupture has been reported by field observations of GEER, 2009, EMERGEO Team, 2009, and Walters et al., 2009. In the later study, a rupture of ~10 cm along a 3 km section of the fault, has been observed and mapped which agrees with this prediction.

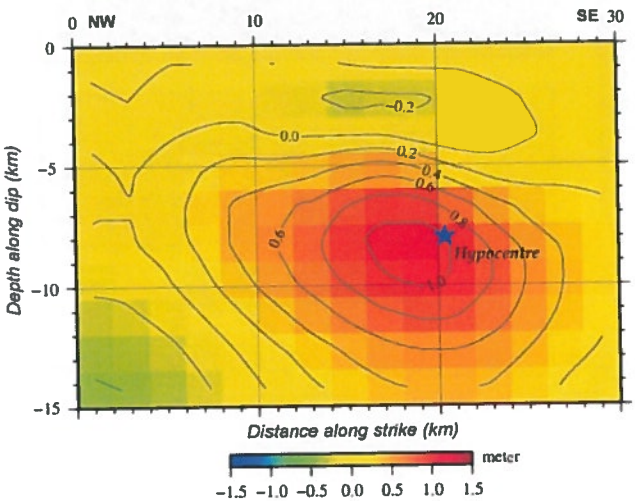


Figure 65: Distribution of dip slip along the fault plan resulted from the ascending pair

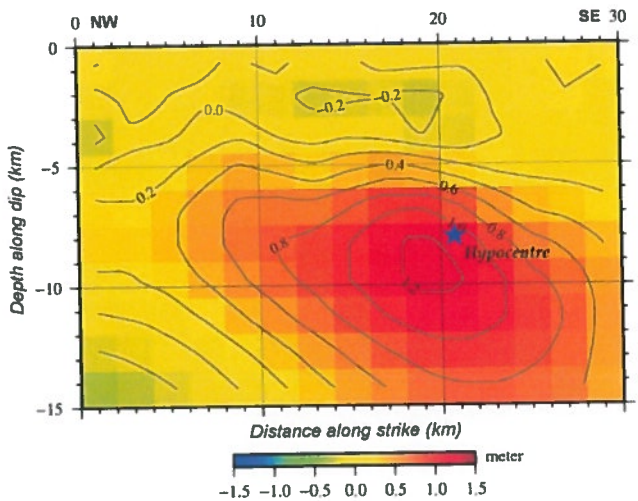


Figure 66: Distribution of dip slip along the fault plan resulted from the descending pair

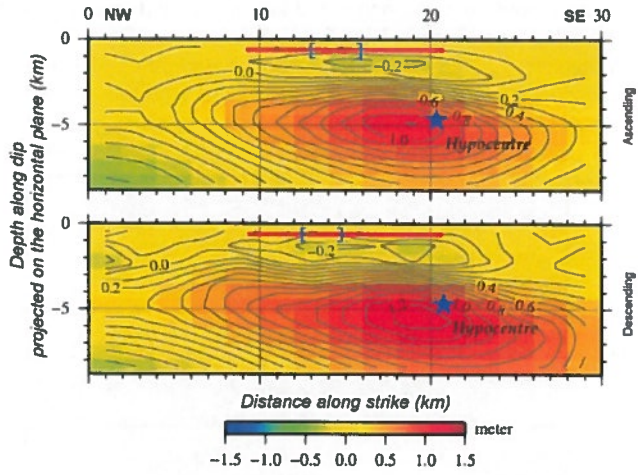


Figure 67: Distribution of dip slip projected on the horizontal plane

Chapter 6

Third Avocatore: I have an earthquake in me!
Ben Jonson, Volpone

6 Discussion

The employed methods and data sets expressed good capabilities to discover different aspects of a seismic event. This chapter makes use of the obtained results (presented in Chapter 5), and discusses about the capabilities of each technique and data set as well as other considerations and theories.

6.1 SAR interferometry

Comparison of interferograms obtained from the ENVISAT ASAR and COSMO-SkyMed data sets (Figures 18 and 19, and Figure 20 in Chapter 5, respectively), revealed that the coseismic surface deformation was initially concentrated to the northern part of the main event epicentre, and then was gradually extended to the south and south-east, during the post-seismic relaxation process.

According to D. Cheloni et al. (manuscript in preparation, 2009, from Walters et al., 2009), contribution of the post-seismic deformation in the interval of the ENVISAT ASAR coseismic interferograms, including the two main after-shocks of April 7th and 9th, has been measured about 7% of the main shock moment release. This moment is equivalent to less than one fringe, and therefore, it can be inferred that this movement is not due to the after-shocks, specially when the after-shock of April 9th has occurred to the north of the main event epicentre. However, there was no GPS velocity field available that records the post-seismic deformation. This would help to determine the spatial signature of the post-seismic deformation, and hence, help to determine if it comes from a deep or superficial slip (Peyret, 2009, personal communication, December 17).

The similarity between the ENVISAT ASAR and the ALOS PALSAR interferograms, in comparison to the COSMO-SkyMed interferogram, indicates that the largest coseismic deformation occurred between April 9th and April 12th. This behaviour and the interaction among the multiple fault segments, provides an excellent opportunity to study interaction of segmented fault blocks during coseismic deformations.

As it was hypothesized in the other studies (e.g. Walters et al., 2009; Valensise, 2009 from GEER, 2009), the causative faults would have dislocated a portion of the crust without rupturing the ground surface. This is inferred from pattern of the fringe systems which do not suddenly close on the trace of the fault. Therefore, the transition between the foot-wall and the hanging-wall has been done smoothly and is not markable (see Figures 81 and 83 in Appendix A).

Bazzano and Pettino surface faults might be reactivated in the consequence of the April 6th earthquake (Valensise, 2009, from GEER, 2009). The later would have a dip of 70°, in accordance with the dip of other active faults in the L'Aquila area. The Paganica fault may root in a deeper fault with a lower dip angle, as it is suggested by focal mechanisms reported from seismological methods (see Table 7 in Chapter 3). This fault would have induced the main shock. An incidental concentration of seismic energy would have occurred on the Paganica fault, and the strong shaking would have caused a displacement greater than the experienced by the two other tectonic elements (Bazzano and Pettino faults), that were reactivated (GEER, 2009).

The difference between the extent of negative and positive displacements along the satellite LOS direction, would indicate the activation of a gravitational shaking mechanism, specially when the movement was occurred along a normal fault, while no significant uplift along the satellite LOS direction was observed on the foot-wall (Valensise, 2009, from GEER, 2009).

The activation or reactivation movement of Paganica, Pettino and Bazzano faults, confirms that these faults are active and capable. Among them, the Paganica fault had been given less importance relative to other nearby active faults, partly because it does not have geomorphological expression on the ground surface. This point highlights the existing problem in identification of the potentially dangerous seismogenic faults in this and similar tectonic regions.

6.2 Sub-pixel correlation technique

Regardless of the obtained result from applying SCT to the case of April 6th, 2009 earthquake in L'Aquila area, the technique is still powerful in principle for detection and measurement of horizontal displacements, if it is applied to images with appropriate (ground) pixel resolution with presence of an accurate DEM and other complementary data sets explained in Chapter 4.

To show this, same technique and software were applied on two pairs of ENVISAT ASAR data set for Bam earthquake of 2003, Iran, listed in Table 27, all acquired in imaging mode, IS2 and L0 processing level.

Pair no.	Orbit	Track	Acquisition date	Pass	B_{\perp} ¹	Height ambig. ²
1	10459	385	2004/02/29	Asc.	-541 m	17 m
	08956		2003/11/16			
2	10194	120	2004/02/11	Des.	2 m	3798 m
	09192		2003/12/03			

Table 27: ENVISAT image pairs for applying SCT on the Bam earthquake, Iran

Figures 68 and 69 show azimuth offsets of the ascending and the descending pairs, respectively. The ascending pair has relatively a long perpendicular baseline; however, due to arid climate of Bam area, quite noteworthy results were achieved. On these figures, big white patches show cities of Bam and Baravat (above and to the right side of the fault trace, respectively). They were highly decorrelated (mostly due to collapsed buildings and the debris) and therefore, were masked. The white stripes on both figures, are artefacts made by the SCT software.

1 Refined using the unwrapped phase and the topography.

2 Calculated from ancillary data files provided in header of images, using Equation 10 in Chapter 2.

This shows importance of choosing a proper data set for a specific purpose. For such a study, when horizontal displacements are estimated to be in order a few centimetres, SPOT 5, FORMOSAT-2, Quick Bird and WorldView-1 image data sets from optical category, and RADARSAT-2 (with 3 m spatial resolution; RADARSAT-2, 2008) and COSMO-SkyMed (with 1 m and 3 m spatial resolutions in 'Spotlight' and 'Stripmap' modes, respectively; COSMO-SkyMed, 2009) Radar image data sets from SAR category, are recommended.

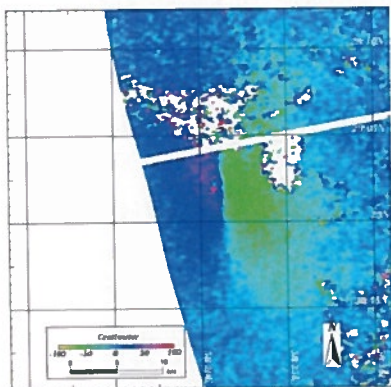


Figure 68: Azimuth offset from the ENVISAT ASAR ascending pair for Bam area

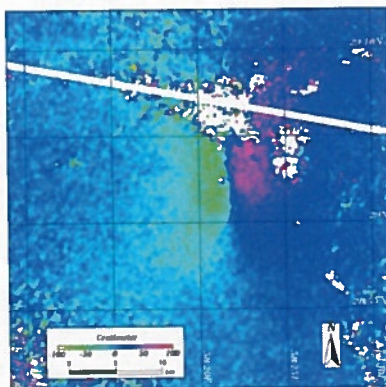


Figure 69: Azimuth offset from the ENVISAT ASAR descending pair for Bam area

On the contrary, horizontal displacements on the ground, may be larger than what has been observed. Indeed, only high gradients (such as fissures) are observed; but distributed ground deformations can not be detected (Peyret, 2009, personal communication, December 15).

6.3 Inversion problem

Slip distribution models of the coseismic movement (see Figures 65 and 66 in Chapter 5), showed a limited slip on the surface for the Paganica fault. This finding is supported by field observations of GEER, 2009, and Walters et al., 2009, at several places along the alignment of coseismic ground fractures, which have reported maximum displacement of 10-12 cm, in comparison to the calculated overall dip slip of ~ 1 m from the NA approach (see Table 24 in Chapter 5).

One major advantage of the NA approach is that it collects information for all the tested models. Then some statistical analysis can be performed in order to discuss about reliability of the estimated parameters (this was left as a recommendation; see §7.4.3).

Analysis of different observations and data sets, lead to two primary and apparently contradictory hypotheses about the tectonic structure of the April 6th earthquake. The first hypothesis is that the Paganica fault was seismogenic and capable to generate the main event. In other words, the slip and dislocation at depth were sufficiently high to touch the ground surface and make ground failures around the fault trace (Salvi et al., 2009; see Figures 65 and 66 in Chapter 5). This hypothesis would be reasonable, but not completely convincing when, first, there are evidences for low surface displacements by the observed (EMERGEIO Team, 2009; GEER, 2009; Blumetti et al., 2009) and predicted (see Figure 67 in Chapter 5) ground surface fractures,

and second, the area with maximum subsidence in the satellite LOS direction was located about 3-5 km far from the surface expression of the this fault to the south-west (Figure 70).

The second hypothesis implicates to existence of another low angle fault, which was displaced at depths of about 12 km to about 2-3 km (see Figure 66 in Chapter 5), and whose projection towards the surface is represented by the Bazzano fault (GEER, 2009). A passive remobilization would have caused the observed movement along this fault, like that of the Bazzano fault (Valensise, 2009, from GEER, 2009). The later fault intersects its plane at a depth of about 2-3 km (GEER, 2009) and is antithetic with respect to the Paganica fault, shown in Figure 70 (see also Figure 6 in Chapter 3; Figure 72 in Appendix A).

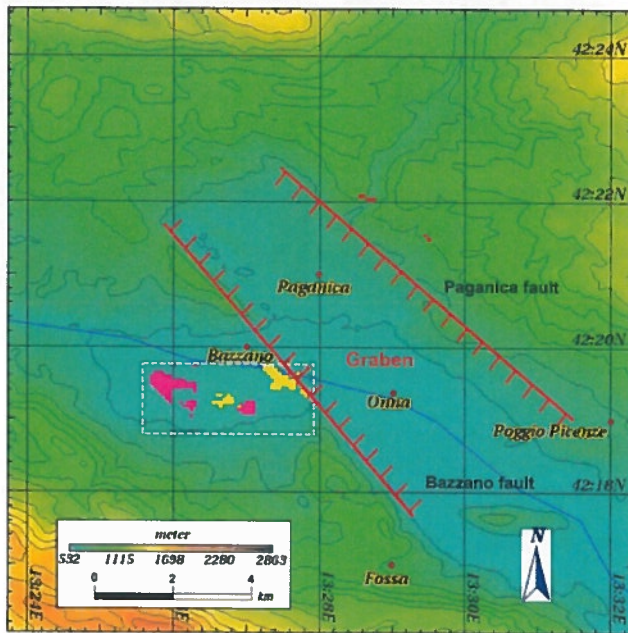


Figure 70: The Onna graben

Along with these two hypotheses, there are other important theories and considerations which are derived from literature and field observations and reports of EMERGEO Team, 2009, and GEER, 2009.

A graben has been made by the Paganica fault (dipping to south-west) and the Bazzano fault (dipping to north-east and antithetic to the Paganica fault), where the village of Onna is situated (Figure 70). Most probably, the seismic energy has been concentrated and trapped inside of the graben filled with Quaternary continental deposits (see Figure 71 in Appendix A), which are in strong velocity contrast with the rigid substrate composed of Meso-Cenozoic deposits (GEER, 2009). This area experienced maximum macro-seismic intensity of X MCS (see Figure 8 in Chapter 3).

The area with maximum subsidence in the satellite LOS direction derived from SAR interferometry (the white dashed-line box on the Figure 70), is located to the west of this graben.

Morphologically, the area is flat and has low elevation, with respect to the surrounding topography. Consequently, this area seems to represent the morphological expression of deeper tectonic movements, compared to those that were produced on the surface faults of Bazzano and Paganica.

The actual morphology of this depressed area, suggests that such vertical movements would have previously involved this plain, apparently without surface expressions of tectonic discontinuities.

Another possible explanation arises for the Onna graben, which is the result of a coupled movement between the Paganica and the Bazzano faults. Therefore, the mobilization of the Paganica fault would have not been seismogenically significant in which, this tectonic feature would have been involved only in processes of selective remobilization (Valensise, 2009, from GEER, 2009).

The Paganica fault would be rooted at such a depth that would render a possible and probable process of channelling incident seismic energy produced on another and deeper fault plane that would not have a surface expression (blind fault) (Valensise, 2009, from GEER, 2009), with a low dip angle like that is suggested by the focal mechanism of the April 6th earthquake (see Table 7 in Chapter 3). It might be also due to an old compressive thrust reactivated in the normal direction (GEER, 2009).

Chapter 7

If a man will begin with certainties, he shall ends in doubts;
but if he will be content to begin with doubts, he shall ends in certainties.
Francis Bacon, The Advancement of Learning

7 Conclusions and recommendations

The seismic sequence in the Abruzzi region in centre of Italy, which started in December 2008, culminated on April 6th, 2009, when an earthquake of M_w 6.3 struck the medieval city of L'Aquila (the capital of Abruzzi province) and the surrounding towns and villages at 01:32 (UTC). The earthquake caused serious damage to the buildings and historical heritage of the city, and caused hundreds of casualties and left thousands of people homeless.

Since the last major earthquake in 1980 in Popoli (about 39 km to the south-east of L'Aquila city), the L'Aquila basin and its active faults system have not been studied with advanced geodetic methods. The ground surface deformation caused by this earthquake, and the geometrical and source parameters of the causative fault in the L'Aquila area, were studied in this research and it was attempted to give a clear view of the geodetic, geological and geophysical changes in the study area, which were made by the earthquake.

An interdisciplinary method was proposed to cover different aspects of the event. While SAR interferometry, was used to reveal the ground displacement in the satellite LOS direction, a sub-pixel correlation technique was employed to detect the surface horizontal displacements, to achieve a more comprehensive result. Furthermore, an Inversion problem was applied to the deformation models obtained from SAR interferometry, to find the source parameters of the causative fault and the dislocation at depth.

Different data sets were acquired for this study to use the different methods. For InSAR, while ERS-1/2 SAR data sets were not suitable, ENVISAT ASAR and ALOS PALSAR data sets were processed. To apply the SCT, two completely different data sets of SAR and optical images, namely ENVISAT ASAR and ASTER, were used. The Inversion problem was done using the obtained deformation models of ENVISAT ASAR data set, from SAR interferometry.

The results of each section which were presented in Chapter 5 and discussed in Chapter 6, are summarized here to achieve the objectives of the research. The research questions formulated in Chapter 1, are also answered in the light of the results and conclusions, in order to meet the objectives. Following this, limitations of methods and data sets are discussed, and the chapter will be ended by recommendations for similar case studies and delineating the future directions.

7.1 Overall results

Results of this study are stated here as a whole, and exact numerical values are presented in § 7.2 .

7.1.1 Results from SAR interferometry

An elongation in the satellite LOS direction (considered as subsidence and dip-ward motion) on the hanging-wall of the north-west to south-east striking normal fault, dipping to south-west, was observed by SAR interferometry. A shortening in the satellite LOS direction was also measured on the foot-wall of the fault, considered as uplift in the satellite LOS direction, from the ENVISAT ASAR data set. The deformation was originated from north of the epicentre and propagated to the south and south-east, after April 9th.

The maximum subsidence of 28.1 cm along the satellite LOS direction was measured from the descending pair of the ENVISAT ASAR interferogram, to the north-west of the village of Onna, located about 7 km to the south-east of L'Aquila city.

The cross sections perpendicular to the fault trace, showed that the gradient of deformation mostly occurred in the graben between Paganica and Bazzano faults (see Figure 6 in Chapter 3 for cross section and Figure 70 in Chapter 6 for map of the Onna graben).

Results from interferometry, as well as other results from seismology and remote sensing observations, gave adequate evidence to suggest that most probably the earthquake was caused by reactivation of the Paganica fault (see §6.3 for discussion).

7.1.2 Results from sub-pixel correlation technique

While InSAR revealed a significant deformation in the satellite LOS direction, the results obtained from applying SCT on both SAR and optical image data sets did not show significant horizontal displacements. This is due to either not sufficiently fine (ground) resolution of the used data sets for detection of small and distributed horizontal displacements, or is due to insignificance of the induced horizontal displacements by the earthquake (see §6.2 for discussion).

This result was anticipated prior to the study, due to normal geometry of the causative fault (which has been reported from seismological methods). Other studies which have been done using GPS observations confirm this result.

7.1.3 Results from Inversion problem

Geometrical parameters of the causative fault were found using the neighbourhood algorithm, whereas the distribution of slip over the fault plane was determined by the linear weighted least square inversion.

Inversion by the NA approach could model most of the fringe systems. The residual interferograms are assigned to lateral rheology changes during the post-seismic relaxation time. The NA showed the causative fault strikes from north-west to south-east direction and dips toward the south-west. The fault has a significant overall normal dip slip, but just a small slip component on strike direction. The predicted fault projected on the ground surface, coincides with the trace of the fault. It passes from high topography in the north-west and lower topography further to the south-east.

The fringe systems are modelled better (i.e. lower RMSE misfit and higher correlation) by the LS inversion. The point with maximum dip slip found by this method, is spatially very close to the centroid of fault plane found by the NA. The LS inversion predicts a small rupture along the 2~3 km of the fault trace.

While the results from InSAR models (whether from this research or from other studies), were spatially and numerically consistent, the results from seismological methods are quite dif-

ferent and dispersed in terms of magnitude and location, however still supporting the results from InSAR models.

7.2 Answer to research questions

At the start of this study, several research questions and hypotheses were proposed, which are answered here to cover the research objectives.

Question: How much is the maximum displacement in the satellite line of sight (LOS) direction? and how is the the distribution and pattern of the deformation?

Answer: The different image data sets in different satellite passes give significant but slightly different answers. The measured deformation values in the satellite LOS direction are summarized in Table 29.

Data set	Pass	Subsidence (cm)	Uplift (cm)
ENVISAT ASAR	Asc.	26.1	1.3
	Des.	28.1	5.5
ALOS PALSAR ¹	Asc.	25.6	Not measured
	Asc.	25.1	Not measured

Table 28: Summary of measured subsidence and uplift along the satellite LOS direction

A one lobe pattern on the hanging-wall is seen on both the ENVISAT ASAR and the ALOS PALSAR interferograms, with 25 km length, 15 km width and 300 km² area, roughly. The descending ENVISAT ASAR interferogram shows less than one complete fringe on the foot-wall. Fringe systems on the hanging-wall and foot-wall are asymmetric.

Question: What are the geometrical parameters (length, depth, strike, dip and slip) of the causative fault?

Answer: Depending on the ascending or descending models, solutions are slightly different. The geometrical parameters of the causative fault found from the NA inversion, are summarized in Table 28.

Model	Strike (°)	Dip (°)	Slip (m)	Length (km)	Depth (km)
Asc. InSAR	144	54	- 0.82	11.565	7.978
Des. InSAR	144	54	- 1.00	11.390	7.976

Table 29: Geometrical parameters of the causative fault derived from the NA approach

Question: How is the slip distribution pattern and dislocation model of the causative fault at depth?

Answer: Based on the corresponding ascending or descending models, slightly different numerical values were found. Figures 65 and 66 in Chapter 5 show spatial distribution of dip slip over the fault plane for the ascending and descending models, respectively.

1 Values are after applying the enhanced Lee filter.

Model	Max. dip slip (m)	M_w	M_0 (Nm)	V_c (km)	Z_c (km)
Asc. InSAR	1.11	6.32	3.8×10^{18}	19	8.25
Des. InSAR	1.26	6.49	6.84×10^{18}	19	9.75

Table 30: Source parameters of the causative fault derived from the LS inversion

Question: How much are the results from different interferometric data sets, in agreement? Which aspect of a seismic event can be addressed better by a specific data set?

Answer: Referring to Table 29, while different image data sets give slightly different values, they are still strongly supportive and consistent. The differences are mainly due to sensitivity vector of the corresponding data set and the satellite pass, which can be justified by the Equation 12 in Chapter 2, with respect to different time span of the interferometric pairs and the post-seismic relaxation (see §5.1.1 for interpretation).

ENVISAT ASAR data set has higher incidence angle than ALOS PALSAR, and consequently is more sensitive to vertical displacement. In turn, sensitivity vector of ALOS PALSAR has a higher horizontal component in east-west direction which makes it more proper for revealing horizontal displacements. So, vertical displacement of faults is determined better by ENVISAT ASAR data set.

Pass direction of SAR satellites (ascending or descending) influences the results with respect to geometry of the causative fault and a proper pass should be selected with respect to the fault strike (see Figures 56 and 57 in Chapter 5, for the geometrical interpretation).

ALOS PALSAR has a longer wavelength and can penetrate more in the target objects, which makes it less sensitive to temporal variations. So, less decorrelation is seen in ALOS PALSAR interferograms. Therefore, when temporal variation is high on the ground surface, deformation can be measured better by the ALOS PALSAR data set.

As a result, each data set reveals one aspect of a seismic event better than others. Practically, influencing parameters should be compromised to choose the most proper data set.

Question: How strong is the SCT procedure to reveal horizontal surface displacements (specially for normal faults)?

Answer: In the case of L'Aquila earthquake, insignificant horizontal displacements in one hand and coarse (ground) resolution of the used image data sets on the other hand, led to an unsatisfactory answer. When ground horizontal displacements are small, image data sets with finer (ground) pixel resolution and more stable platforms should be employed (see Tables 14 and 15 in Chapter 4 for details; §6.2 for discussion).

7.3 Limitations

Even though the applied techniques are quite robust, they have their own limitations and weaknesses. Only those limitations which were faced in this research for each technique, are described here, but undoubtedly there might be other limitations.

7.3.1 Limitations on InSAR technique and data sets

For applying InSAR in this study, some limitations were encountered, which are listed as follows:

- Unavailability of both ascending and descending ALOS PALSAR image data set for all over the places (for instance, there is no descending ALOS PALSAR image for L'Aquila area).
- One dimensional measurement, which gives deformation projected on the satellite LOS direction.
- More sensitivity to vertical displacement, rather than to horizontal.
- Sensitivity to phase decorrelation, specifically near and on the rupture, where usually spacial decorrelation is too much.
- Remaining atmospheric phase delay unmodelled in final interferograms (the phase delay can bias the result).
- No unique solution for phase unwrapping (different algorithms with different initial values, give different results).

7.3.2 Limitations on SCT and data sets

The following limitations were encountered in this research by using the SAR data set:

- Not sufficient ground resolution of the available SAR data sets, compared to the occurred horizontal displacements, specially in range direction.
- Low sensitivity to horizontal displacements, specially in azimuth direction (due to imaging geometry).
- Highly affected by topography shadow, layover and foreshortening phenomena, specially in high mountains.
- Highly decorrelated by ground surface characteristics, such as soil moisture, vegetation cover and soil texture.

The following limitations were encountered in this research by using the optical data set:

- High sensitivity to temporal changes, e.g. due to change in vegetation coverage. Temporal changes of the ground surface, degrade quality of correlation between image pair scenes and usually lead to decorrelated patches and unrealistic results.
- Highly affected by other temporal variations of the ground surface, such as shadowing effects and snow.
- Highly affected by accuracy of the used DEM in high reliefs or rugged trains.
- Highly affected by instability of the platform attitude, whereas precise orbital files are not available same as for the SAR satellites (this leads to parallel stripes and undulation in the offsets).

7.3.3 Limitations on Inversion problem

For geodetic inversion problem modelling, the following limitations were encountered in this study:

- Lack of horizontal offsets to introduce to the inversion model (this could be an output from SCT analysis).

- Lack of vertical offset to introduce to the inversion model (this could be prepared if spirit levelling data set was available).
- Unavailability of proper SAR model which spans only the main shock (due to long temporal resolution of ENVISAT ASAR image data set. This could be managed, if COSMO-SkyMed satellite image data set was available).
- High computational cost.
- Lack of geological field work (due to financial limitation).

7.4 Recommendations

As this study was done in a short period of time and financial constraint, more opportunities are possible, if it could be repeated in a longer period, with less limitation on data provision. Some recommendations are presented here to improve quality of this research (whether for this or other similar case studies).

7.4.1 Recommendations on InSAR

The following items are recommended for SAR interferometry:

- To use most accurate orbital parameters and instrumental files for eliminating the orbital signature from interferograms, even though they are published within a couple of weeks after image acquisition date (imprecise orbit files are recommended just for preliminary results).
- To use shortest possible temporal baseline (to avoid temporal changes on the ground surface) or choosing images from same dates of consecutive years.
- To choose SAR image pairs in both ascending and descending passes, even though choosing a proper pass is possible with respect to geometry of the causative fault and Equation 12 in Chapter 2.
- To use a precise and accurate DEM for the area to achieve the best possible results, because the orthorectification and re-sampling steps are highly sensitive to the used DEM. Errors in DEM can bias the estimated displacements.

The following points are recommended for the future work, using InSAR technique in terms of choosing the proper SAR data set:

- To use ENVISAT ASAR data set for studying normal or thrust fault systems, when the vertical displacement is dominant.
- To use ALOS PALSAR data set for studying strike slip fault systems, when the major displacements are horizontal.
- To use ALOS PALSAR data set, when the study area is prone to temporal variations.
- To use ground truth data sets observed from terrestrial methods, such as spirit levelling measurements, in order to validation of results.
- To derive the three dimensional model of deformation which is possible using at least three independent interferograms with independent look directions. This item is particularly possible for April 6th L'Aquila earthquake (due to availability of huge number of ENVISAT ASAR images). The vertical component of the deformation model should be validated using spirit levelling data set.
- To improve quality of interferograms using different image pairs from different time sluts and spans, when interferograms are partially decorrelated (e.g. by stacking methods).

- To use a better vegetation index (sensitive to change in biomass) rather than NDVI (which is sensitive to amount of biomass or chlorophyll) for justification of low coherent areas in interferograms.
- To use precipitation and meteorological data sets, for justification of low coherent patches and biased interferograms.

7.4.2 Recommendations on SCT

The following items are generally recommend for sub-pixel correlation technique:

- To choose image pairs with minimum possible B/H ratio (to avoid stereoscopic effect).
- To use a precise and accurate DEM of the area to achieve the best possible results, because the orthorectification and re-sampling steps are sensitive to the used DEM. Errors in DEM can bias the estimated displacements.
- To use ground reference data sets observed from other methods, such as GNSS measurements, in order to introduce to the model and validation of results.

The following items are specifically recommended for using a SAR image data set in SCT:

- To use both phase and amplitude of SAR images.
- To use ENVISAT ASAR data set for faulting systems with smaller horizontal displacements (because of the finer azimuth resolution).
- To use ALOS PALSAR data set for faulting systems in the area with high temporal variations (because of the longer wavelength).
- To use ALOS PALSAR data set for faulting systems when horizontal displacements are dominantly in east-west direction.

The following items are specifically recommended for using an optical image data set in SCT:

- To use optical image data set specially for bare lands or areas with low vegetation coverage.
- To use an optical image data set with sufficient spatial resolution, specially when the causative fault has normal or thrust geometry or when the seismic event has a magnitude of lower than 7.0.

7.4.3 Recommendations on Inversion problem

The following items are recommend for Inversion problem:

- To investigate and to observe the post-seismic effects of the earthquake in the field.
- To use different geodetic data sets, such as GNSS, spirit levelling and horizontal offsets (when they are available).
- To invert all data sets together which might lead to a more steady solution.
- To perform statistical analysis on the results of NA Inversion in order to discuss about reliability of the estimated parameters.

7.5 Future directions

Seismic catastrophic hazards, such as earthquakes, happen frequently and cause many causalities every year, exacting heavy damage on human civilizations. Detection, measurement, moni-

oring and (hopefully in the future) prediction of these inevitable phenomena can help to protect human life and assets.

Although the seismic event of April 6th, 2009 in L'Aquila, Italy, was studied by three different techniques and four different data sets, it is still only the first chapters of the story. Since this study was done in a short period of time with financial and data provision constraints, some suggestions are offered here for future work on longer series with fewer limitations, so this study may serve human societies in the near future.

A study such as this, can be enhanced with better data sets, such as optical images with finer pixel resolution, for sub-pixel correlation technique, and should be supported by terrestrial geodetic data sets, such as spirit levelling data set, for validation of results.

The next portion of this study which needs attention is the calculation of stress changes and this should be followed by strain modelling techniques for determining strain accumulation in the nearby faulting systems. It can then be judged about this important fact that whether the faulting system has been brought closer to, or taken further away from failure, by the occurred seismic activity.

This study can be developed and adapted to measure a ground surface deformation caused by other sources than earthquakes, such as landslides, ground subsidence (due to mining, water pumping, extraction of oil and gas, and so on), coastal sedimentation, sand dunes migration and volcanic activities.

8 Appendices

8.1 Appendix A- Figures

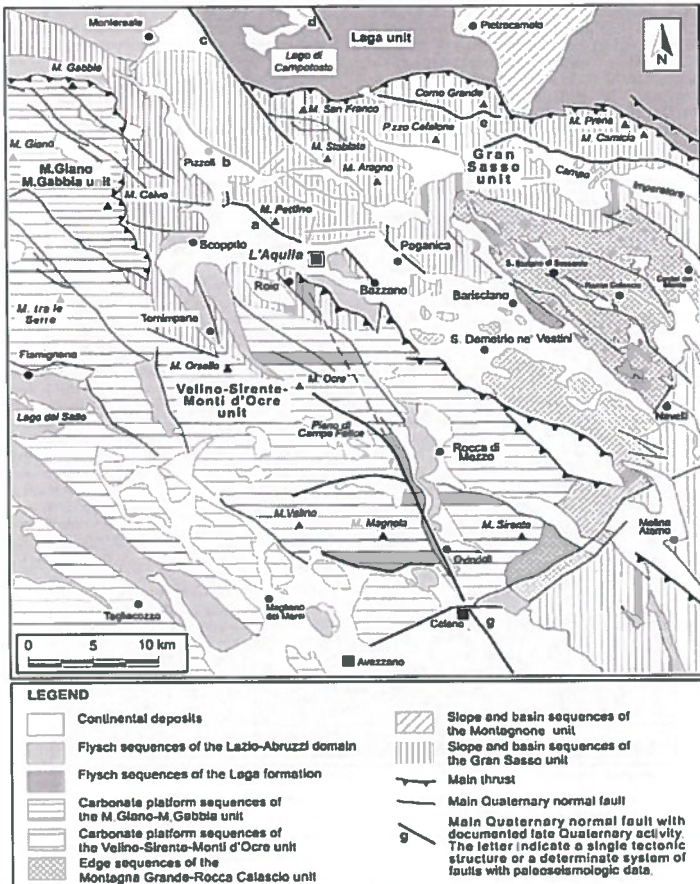


Figure 71: Geological-structural map of the central Apennines (Blumetti et al., 2009)



Figure 72: Active faults of the L'Aquila area (INGV website)

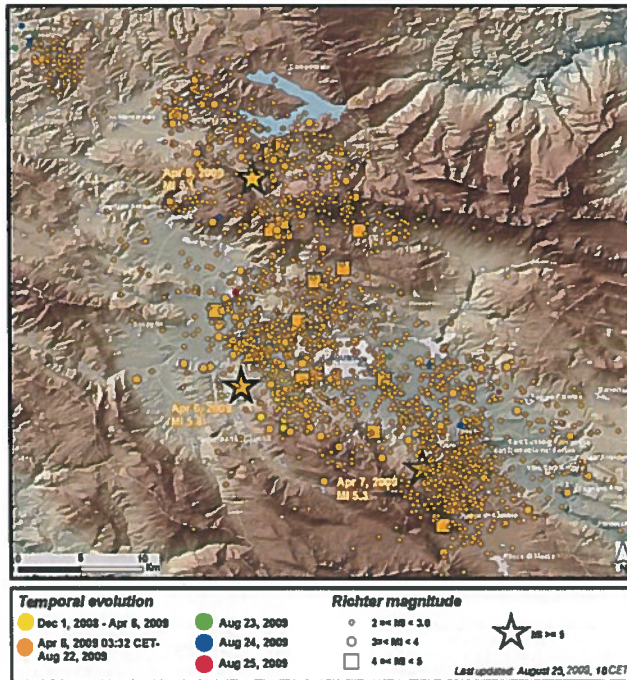


Figure 73: Seismic sequence in L'Aquila area (INGV website)

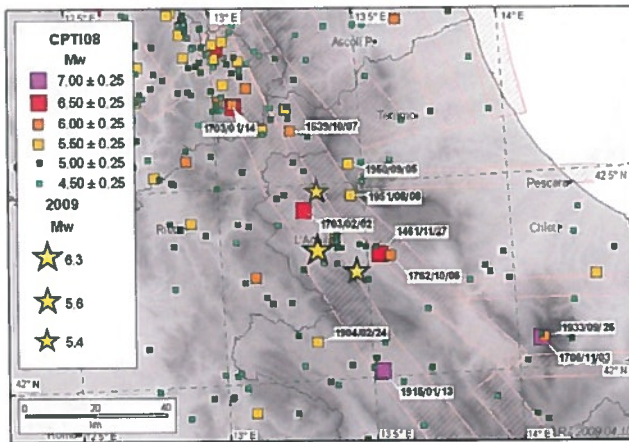


Figure 74: Historical seismicity of the central Apennines near L'Aquila (Rovida et al., 2009)

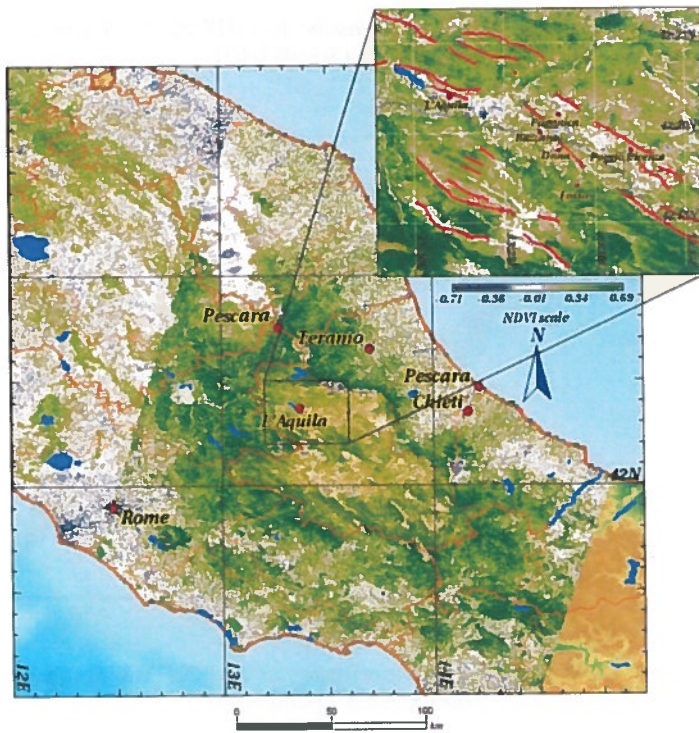


Figure 75: The NDVI map for the centre of Italy

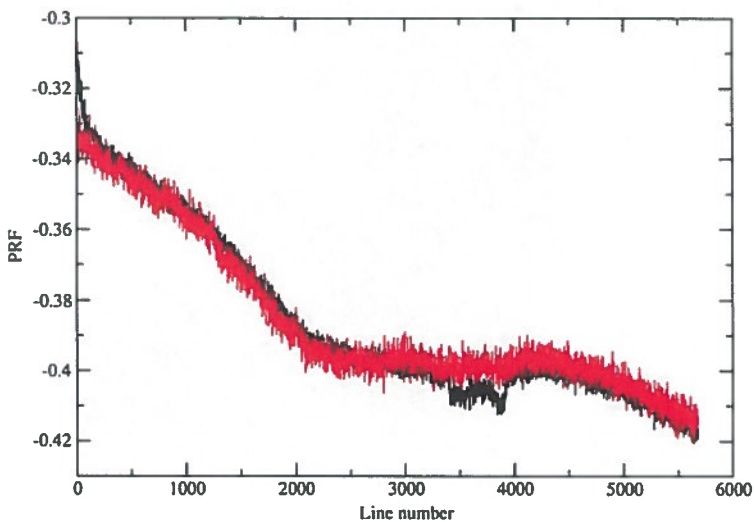


Figure 76: Azimuth spectrum overlap for the ENVISAT ASAR ascending pair (2009/04/15-2009/03/11)

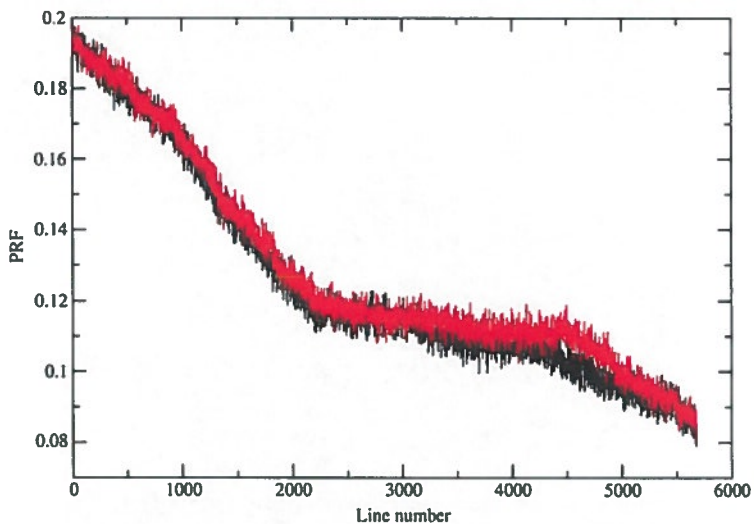


Figure 77: Azimuth spectrum overlap for the ENVISAT ASAR descending pair (2009/04/12-2009/02/01)

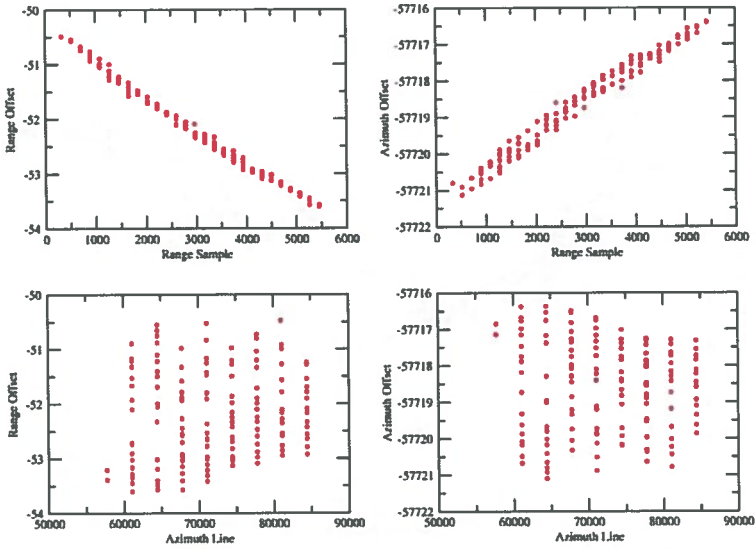


Figure 78: Range and azimuth offsets versus range and azimuth samples for the ENVISAT ASAR ascending pair (2009/04/15-2009/03/11)

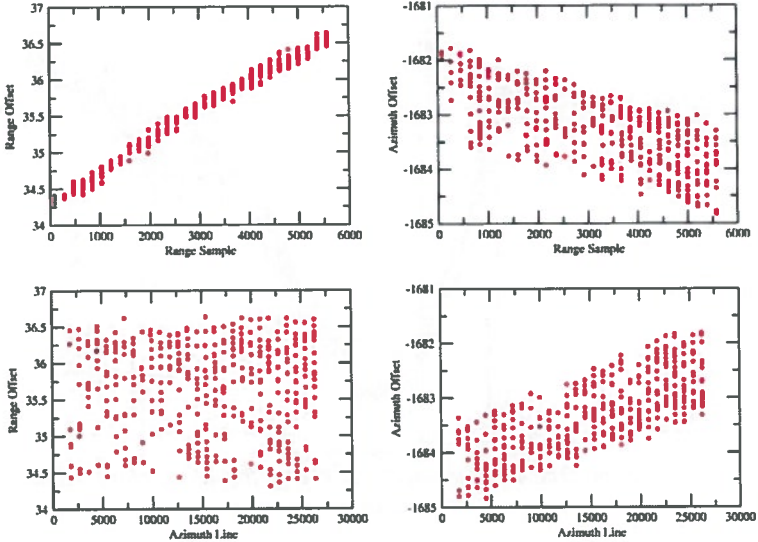


Figure 79: Range and azimuth offsets versus range and azimuth samples for the ENVISAT ASAR descending pair (2009/04/12-2009/02/01)

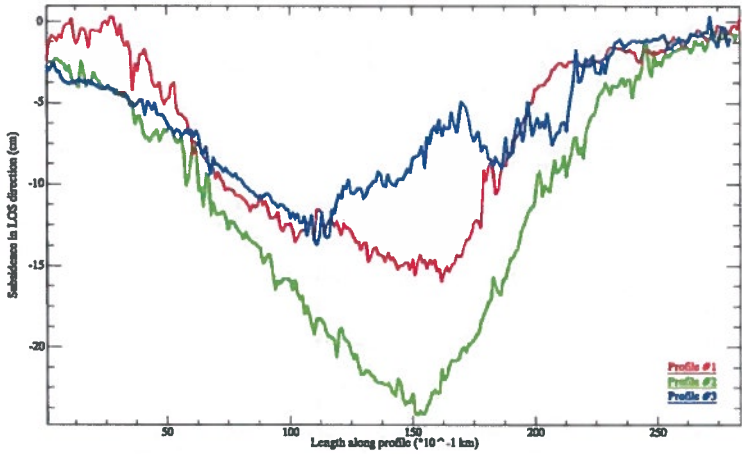


Figure 80: Displacement in the satellite LOS direction along profiles from ENVISAT ASAR ascending pair

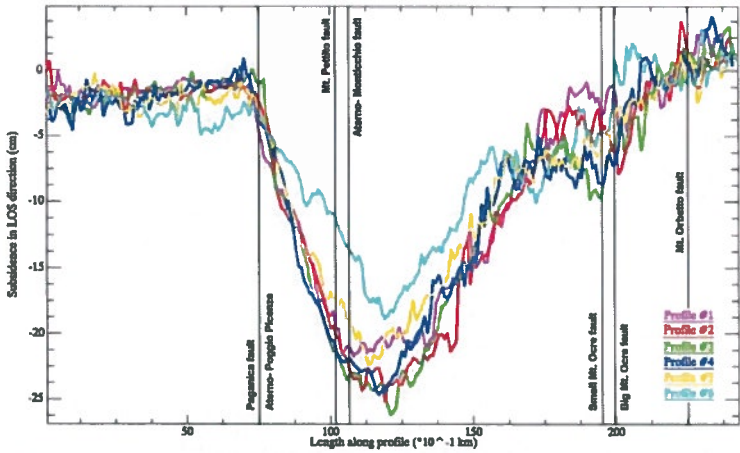


Figure 81: Displacement in the satellite LOS direction along cross sections from ENVISAT ASAR ascending pair

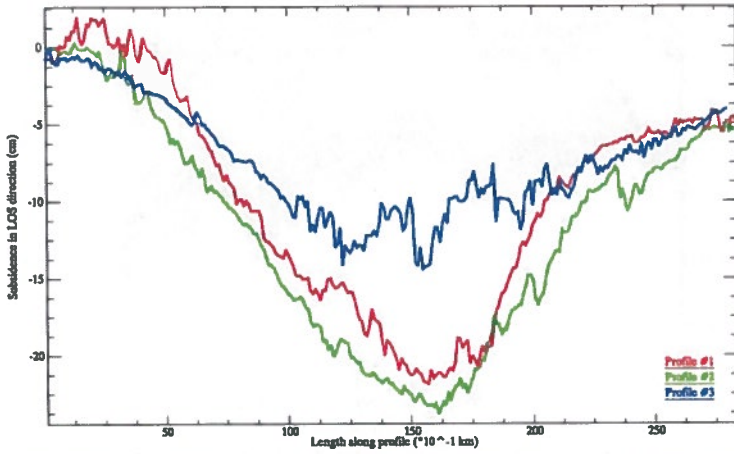


Figure 82: Displacement in the satellite LOS direction along profiles from ENVISAT ASAR descending pair

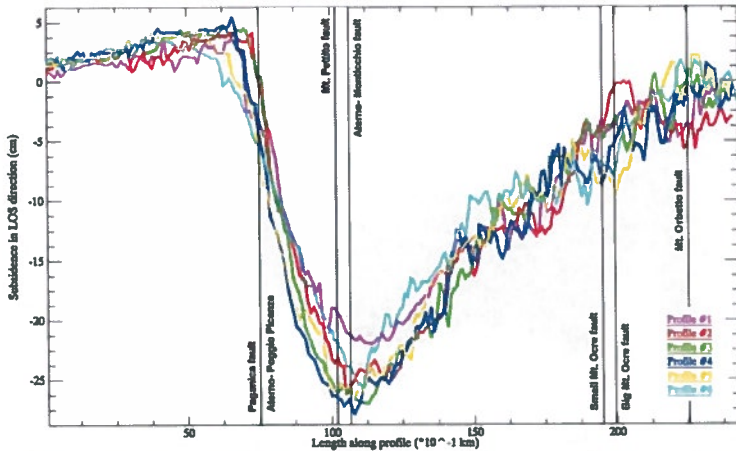


Figure 83: Displacement in the satellite LOS direction along cross sections from ENVISAT ASAR descending pair

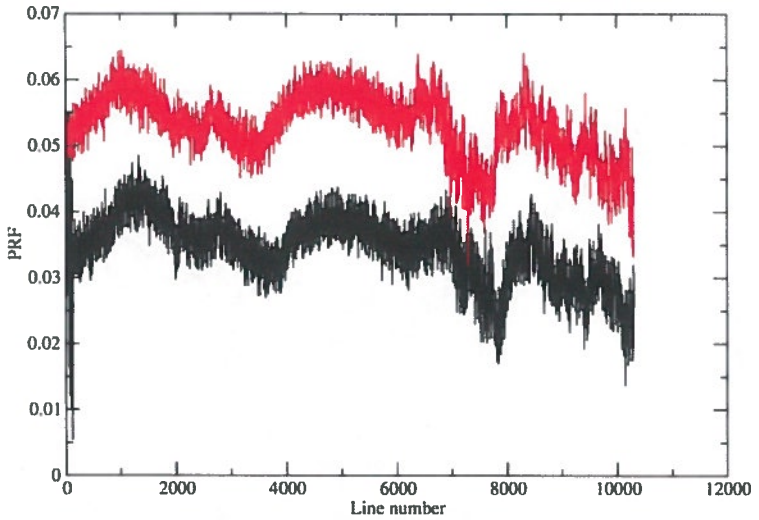


Figure 84: Azimuth spectrum overlap for the first ALOS PALSAR interferometric pair (2009/05/21-2008/07/03)

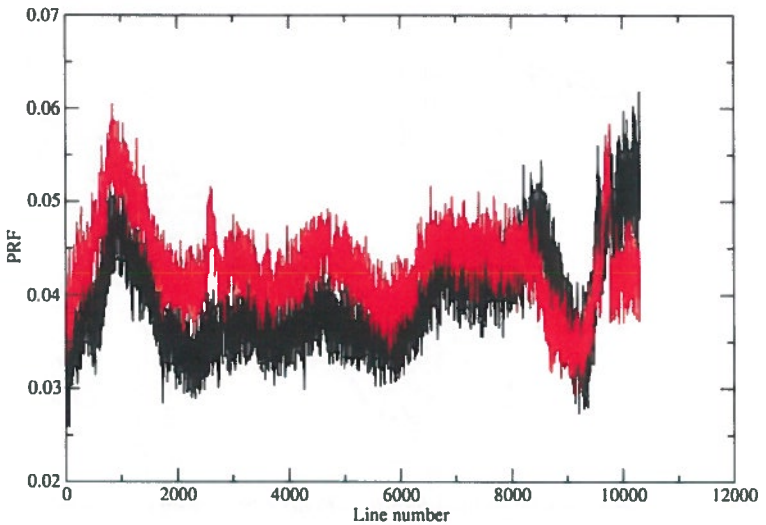


Figure 85: Azimuth spectrum overlap for the second ALOS PALSAR interferometric pair (2009/04/22-2008/07/20)

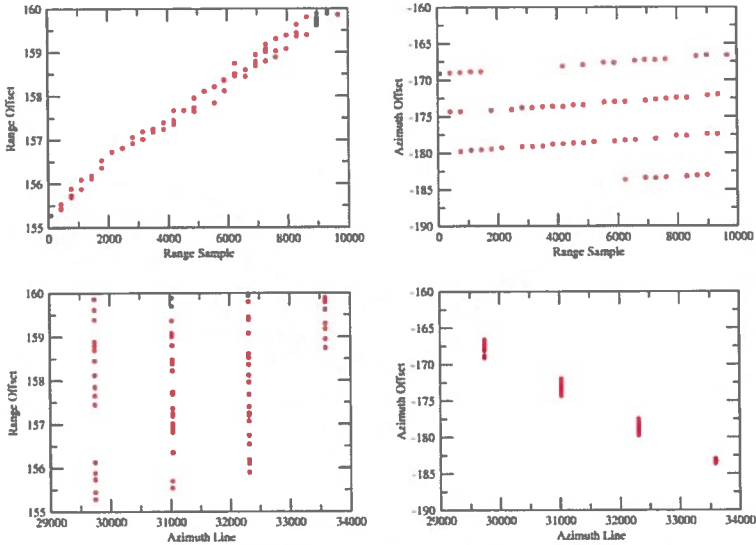


Figure 86: Range and azimuth offsets versus range and azimuth samples for the first ALOS PALSAR interferometric pair (2009/05/21-2008/07/03)

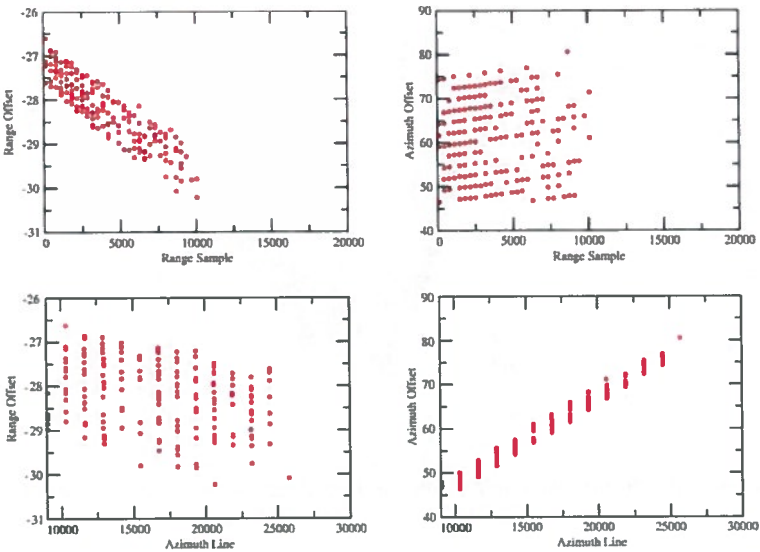


Figure 87: Range and azimuth offsets versus range and azimuth samples for the second ALOS PALSAR interferometric pair (2009/04/22-2008/07/20)

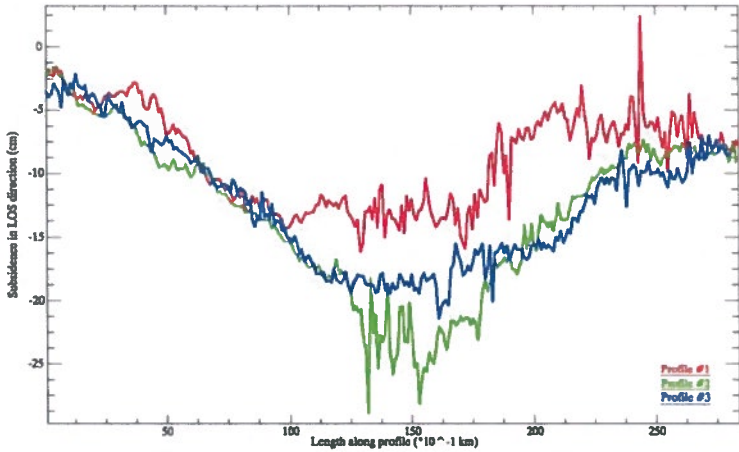


Figure 88: Displacement in the satellite LOS direction along profiles for the first ALOS PALSAR pair (2009/05/21-2008/07/03)

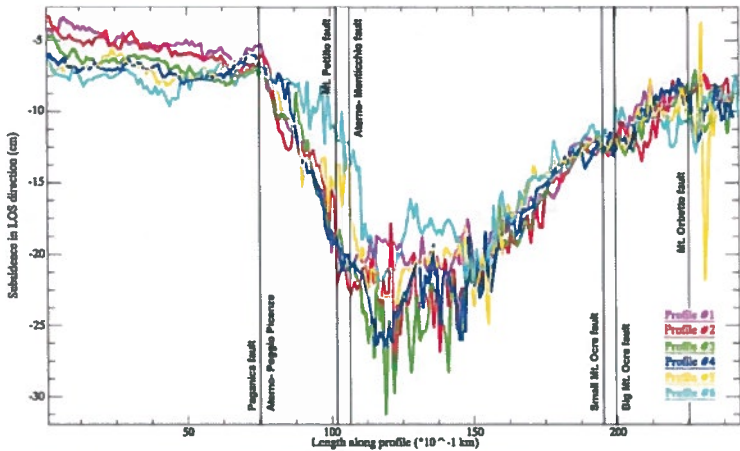


Figure 89: Displacement in the satellite LOS direction along cross sections for the first ALOS PALSAR pair (2009/05/21-2008/07/03)

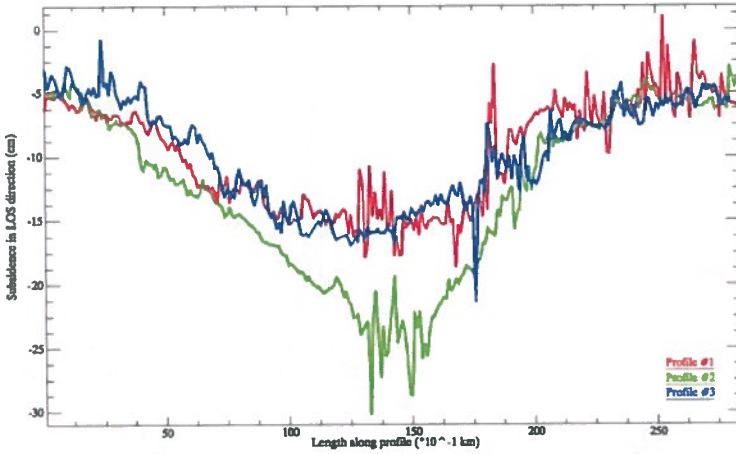


Figure 90: Displacement in the satellite LOS direction along profiles for the second ALOS PALSAR pair (2009/04/22-2008/07/20)

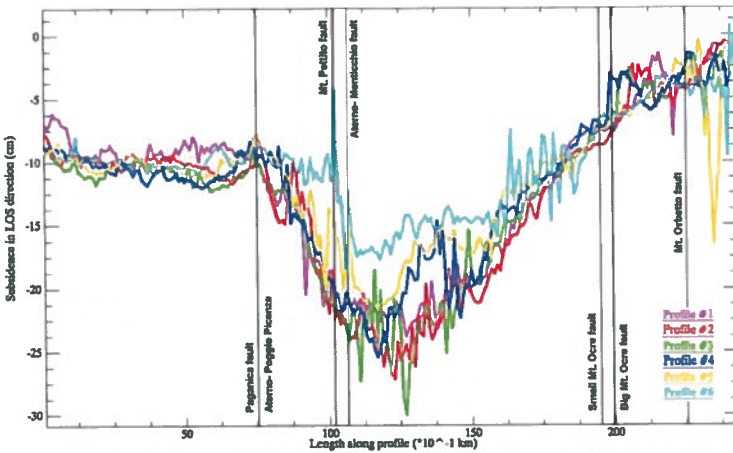


Figure 91: Displacement in the satellite LOS direction along cross sections for the second ALOS PALSAR pair (2009/04/22-2008/07/20)

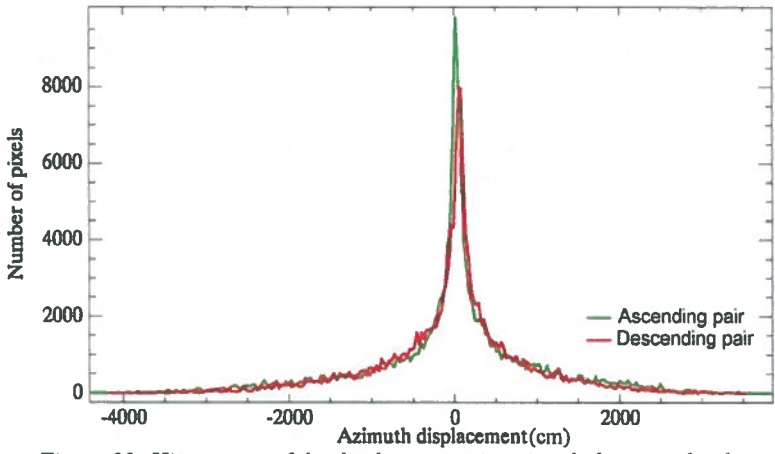


Figure 92: Histograms of the displacements in azimuth direction for the ENVISAT ASAR pairs

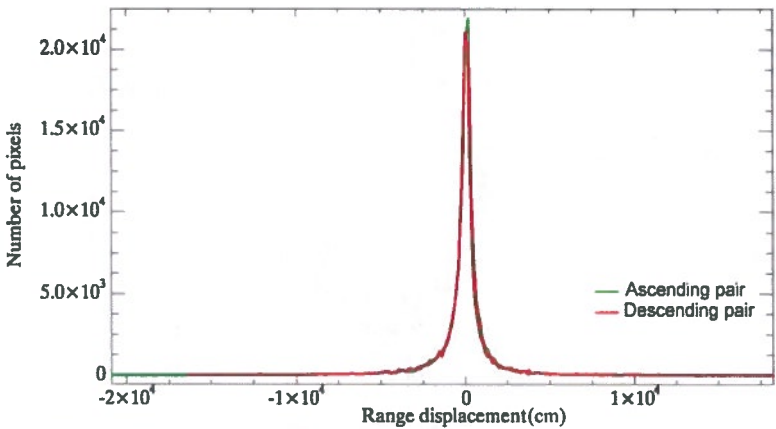


Figure 93: Histograms of the displacements in range direction for the ENVISAT ASAR pairs

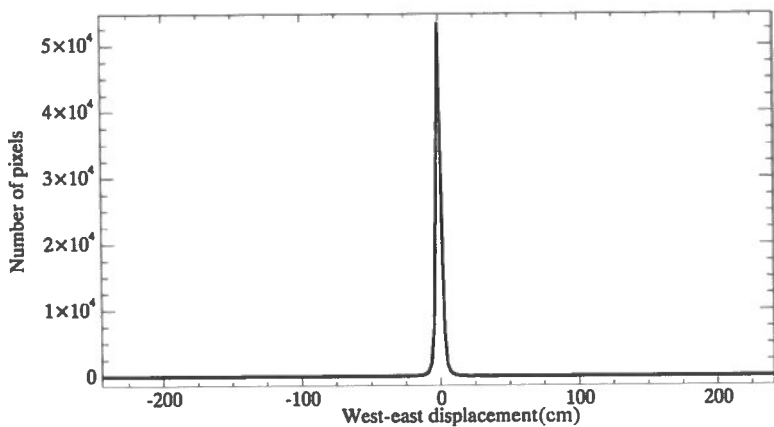


Figure 94: Histogram of the west-east offset for the second ASTER pair

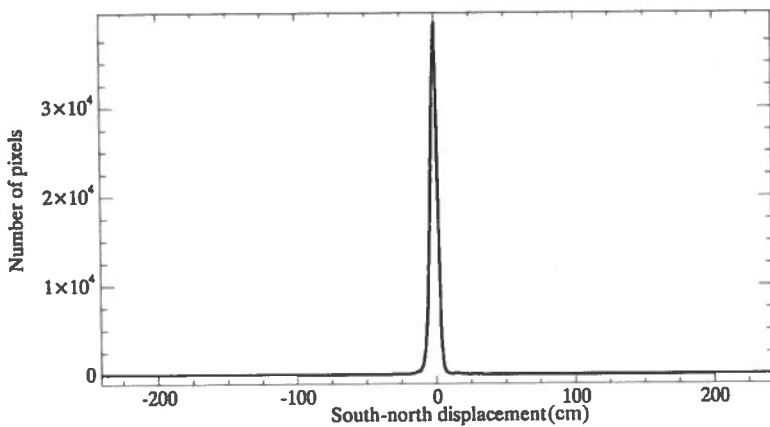


Figure 95: Histogram of the south-north offset for the second ASTER pair

8.2 Appendix B- Tables

Date	Time (UTC)	Lat. (N)	Long. (E)	Depth (km)	Magnitude
2009/04/05	20:48:56.40	42.36	13.37	2	M_L 4.0
2009/04/06	01:32:41.40	42.38	13.32	2	M_w 6.3
2009/04/06	02:27:48.20	42.37	13.23	2	m_b 4.3
2009/04/06	02:37:05.30	42.41	13.32	2	M_w 5.1
2009/04/06	03:56:48.10	42.38	13.34	10	m_b 4.5
2009/04/06	07:17:16.10	42.47	13.40	30	m_b 4.4
2009/04/06	16:38:10.70	42.38	13.32	2	M_w 4.4
2009/04/06	23:15:37.70	42.48	13.41	2	M_w 5.1
2009/04/07	09:26:30.70	42.31	13.35	10	M_w 5.0
2009/04/07	17:47:38.30	42.30	13.40	13 (fixed)	M_w 5.6
2009/04/07	21:34:30.90	42.34	13.37	2	m_b 4.5
2009/04/08	04:27:42.50	42.30	13.43	2	M_L 4.0
2009/04/08	22:56:51.00	42.55	13.34	2	M_w 4.1
2009/04/09	00:53:00.60	42.53	13.39	2	M_w 5.4
2009/04/09	03:14:52.70	42.35	13.46	2	m_b 4.3
2009/04/09	04:32:46.00	42.45	13.39	2	m_b 4.3
2009/04/09	04:43:12.30	42.52	13.34	10 (fixed)	M_L 4.0
2009/04/09	19:38:17.40	42.52	13.35	2	M_w 5.2
2009/04/10	03:22:23.60	42.49	13.42	2	m_b 4.0
2009/04/13	21:14:25.70	42.55	13.34	2	M_w 5.1
2009/04/15	20:17:28.90	42.55	13.23	10 (fixed)	M_L 4.0
2009/04/15	22:53:08.70	42.54	13.28	2	M_L 4.0

Table 31: Earthquake sequence for L'Aquila area since April 5th, 2009 till April 20th, 2009 with magnitude greater than 4.0 (EMSC, 2009)

Name	Version	Application
COSI-corr	2009	Sub-pixel correlator for optical images
EOLi	6.2.4	SAR image selection at interferometric condition
ENVI	4.6	General image processing and analysis
geodinv_na	Prototype	NA inversion code
GMT	4.4.0	Generic mapping tools

GRASS	6.4.0	Geo-spatial Information System software
inverseokada_SAR	Prototype	LS inversion code
Matlab	7.8.0.347	High level scientific programming language
pixelTrack	Prototype	Sub-pixel correlator for SAR and optical images
R	2.9.1	Geo-statistical software
ROI_PAC	3.0	SAR interferometry
SNAPHU	1.4.2	Phase unwrapping algorithm for InSAR

Table 32: List of applications and codes used in this research

Date 1	Date 2	Baseline (m)	Doppler Difference	Track	Pass
2009/04/12	2003/06/08	-248	NA	79	Des.
	2003/11/30	-67	NA		
	2003/11/30	-66	NA		
2009/04/15	1999/10/19	-188	-3320	129	Asc.
	1998/05/13	-186	NA		
	2004/10/13	-158	NA		
	2004/10/13	-156	NA		
	2008/06/04	-129	-2646		
	2008/07/09	295	-4254		
2009/04/28	1999/06/14	-187	896	308	Des.
	1999/06/15	-154	NA		
	2004/06/15	196	NA		
	2008/04/08	-233	902		
	2008/11/04	-115	1675		
2009/05/20	2008/01/16	145	-1468	129	Asc.
2009/06/02	2008/06/17	139	-2758	308	Des.
	2008/06/17	139	-2762		
	2008/09/30	157	1855		
	2008/05/13	165	-2448		
	2008/07/22	185	-742		
	2008/08/26	269	-1274		

Table 33: ERS-1/2 interferometric image pairs

Tile ID	Class 0	Class 1	Ratio
N43E12	550	12966651	0.00%
N43E13	42174	12952027	0.33%
N42E12	2183	12965018	0.02%
N42E13	32855	12934346	0.25%
N42E14	15142	12952059	0.12%
N41E12	2788	12964413	0.02%
N41E13	2429	12964772	0.02%
N41E12	453	12966748	0.00%

Table 34: ASTER GDEM quality assessment

Characteristics	VNIR	SWIR	TIR
Spectral range (μm)	Band 1: 0.52–0.60	Band 4: 1.600–1.700	Band 10: 8.125–8.475
	Band 2: 0.63–0.69	Band 5: 2.145–2.185	Band 11: 8.475–8.825
	Band 3: 0.76–0.86	Band 6: 2.185–2.225	Band 12: 8.925–9.275
	Band 3: 0.76–0.86	Band 7: 2.235–2.285	Band 13: 10.25–10.95
		Band 8: 2.295–2.365	Band 14: 10.95–11.65
	Band 9: 2.360–2.430		
Pixel size (m)	15	30	90

Table 35: ASTER spectral bands and spatial resolutions (ASTER, 2004)

1 st pair (2009/04/15-2009/03/11)				2 nd pair (2009/04/12-2009/02/01)			
Profile	Fringes	Profile	Fringes	Profile	Fringes	Profile	Fringes
1	9	4	8	1	9	4	9
2	8	5	8	2	9	5	9
3	8	6	6	3	10	6	4

Table 36: Number of fringes in different directions for ENVISAT ASAR interferometric pairs

Station	Lat. (°N)	Long. (°E)	ΔE (mm)	$\pm E$ (mm)	ΔN (mm)	$\pm N$ (mm)
AQUI	42.3682	13.3502	9.0	2.1	-42.4	2.1
CADO	42.2926	13.4826	-82.2	3.2	63.6	3.2
CPAG	42.5012	13.2884	1.6	3.9	-1.7	3.8
INGP	42.3825	13.3156	5.5	2.1	-23.9	2.1
INFN	42.4208	13.5158	47.1	2.6	52.2	2.6
ROIO	52.3268	13.3859	8.4	3.2	-8.0	3.1
SELL	42.3691	13.1797	-11.4	3.7	-3.8	3.7
SMCO	42.3927	13.2708	0.4	3.2	-11.6	3.2

Table 37: Coseismic horizontal displacements at L'Aquila near fixed GPS stations (Anzidei et al., 2009)

8.3 Appendix C- Websites

The following websites have been mentioned in the text and are listed here as a reference.

ASAR Auxiliary Data Files: http://earth.esa.int/services/auxiliary_data/asar/
CGIAR consortium: <http://srtm.csi.cgiar.org/>
CROSS: <https://cross.restec.or.jp/>
DEOS: <http://www.deos.tudelft.nl/ers/precorbs/orbits/>
EOLi: <http://earth.esa.int/EOLi/EOLi.html>
ERSDAC: <http://www.ersdac.or.jp/eng/index.E.html>
ESA virtual archive: <http://laquila-earthquake.esa.int/>
GCMT: <http://www.globalcmt.org/>
GEER: http://research.eerc.berkeley.edu/projects/GEER/Post_EQ_Reports.html
GLOVIZ: <http://glovis.usgs.gov/>
INGV: <http://www.ingv.it/>
INGV-S4 Project: <http://earthquake.rm.ingv.it/index.php>
ISPRA: <http://www.isprambiente.it/site/en-gb/>
LP DAAC: <https://lpdaac.usgs.gov/>
QUEST: <http://www.mi.ingv.it/eq/090406/quest.html>
ROI_PAC: <http://www.roipac.org/>
SNAPHU: http://www-star.stanford.edu/sar_group/snaphu/
USGS: <http://www.usgs.gov/>
USGS Earthquake Hazards Program: <http://earthquake.usgs.gov/>
WIST: <https://wist.echo.nasa.gov/~wist/api/imswelcome/> or <https://wist.echo.nasa.gov/api/>

9 References

- Adrian, R. J., 1991. Particle-imaging techniques for experimental fluid mechanics. *Annual Review of Fluid Mechanics*, 23(1), pp. 261-304.
- ALOS, 1997. *About ALOS*. JAXA EORC, [Online] Available at: http://www.eorc.jaxa.jp/ALOS/en/about/about_index.htm (accessed: Aug 19, 2009).
- Amato, A., Azzara, R., Chiarabba, C., Cimini, G. B., Cocco, M., Di Bona, M., Margheriti, L., Mazza, S., Mele, F., Selvaggi, G. and others, 1998. The 1997 Umbria-Marche, Italy, earthquake sequence: a first look at the main shocks and after-shocks. *Geophysical Research Letters*, 25(15), pp. 2861-2864.
- Anzidei, M., Boschi, E., Cannelli, V., Devoti, R., Esposito, A., Galvani, A., Melini, D., Pietrantonio, G., Riguzzi, F., Sepe, V. and Serpelloni, E., 2009. Coseismic deformation of the destructive April 6, 2009 L'Aquila earthquake (central Italy) from GPS data. *Geophysical Research Letters*, 36(17), pp. L17307.
- Archuleta, R. J., 1984. A faulting model for the 1979 Imperial Valley earthquake. *Journal of Geophysical Research*, 89(B6), pp. 4559-4586.
- ASTER G-DEM, 2007. *ASTER Global Digital Elevation Model (ASTER GDEM)*. G-DEM project, [Online] Available at: <http://www.ersdac.or.jp/GDEM/E/index.html> (accessed: September 1, 2009).
- ASTER, 2004. *ASTER: Advanced Spaceborne Thermal Emission and Reflection Radiometer*. NASA Jet Propulsion Laboratory, California Institute of Technology, [Online] Available at: <http://asterweb.jpl.nasa.gov/index.asp> (accessed: September 15, 2009).
- Avouac, J. P., Ayoub, F., Leprince, S., Konca, O. and Helmberger, D. V., 2006. The 2005, Mw 7.6 Kashmir earthquake: sub-pixel correlation of ASTER images and seismic waveforms analysis. *Earth and Planetary Science Letters*, 249(3-4), pp. 514-528.
- Ayoub, F., Leprince, S. and Keene, L., 2009. *User's guide to COSI-Corr: Co-registration of Optically Sensed Images and Correlation*. California Institute of Technology, [Online] Available at: http://www.tectonics.caltech.edu/slip_history/spot_coseis/pdf_files/cosi-corr_guide.pdf (accessed: September 26, 2009).
- Bamler, R. and P. Hartl, 1998. Synthetic aperture radar interferometry. *Inverse Problems*, 14(4), pp. 1-54.
- Bamler, R. and Just, D., 1993. Phase statistics and decorrelation in SAR interferograms. In Proceedings of International Geoscience and Remote Sensing Symposium (IGARSS).
- BBC World News, 2009a. *Powerful Italian quake kills many*. British Broadcasting Corporation (BBC), [Online] Available at: <http://news.bbc.co.uk/2/hi/europe/7984867.stm> (accessed: June 18, 2009).
- BBC World News, 2009b. *After-shock hits Italy quake zone*. British Broadcasting Corporation (BBC), [Online] Available at: <http://news.bbc.co.uk/2/hi/europe/7988832.stm> (accessed: June 18, 2009).
- Berry, P. A. M., Garlick, J. D. and Smith, R. G., 2006. Near-global validation of the SRTM DEM using satellite radar altimetry. *Remote Sensing of Environment*, 106(1), pp. 17-27.
- Berthier, E., Vadon, H., Baratoux, D., Arnaud, Y., Vincent, C., Feigl, K. L., Remy, F. and B. Legresy, 2005. Surface motion of mountain glaciers derived from satellite optical imagery. *Remote Sensing of Environment*, 95(1), pp. 14-28.
- Bing, P., Hui-min, X., Bo-qin, X. and D. Fu-long, 2006. Performance of sub-pixel registration algorithms in digital image correlation. *Measurement Science and Technology*, 17(6), pp. 1615-1621.
- Blumetti, A. M., Comerci, V., Di Manna, P., Guerrieri, L. and Vittori, E., 2009. *Geological effects induced by the L'Aquila earthquake (6 April 2009, $M_l = 5.8$) on the natural environment*. ISPRA- Dipartimento Difesa del Suolo- Servizio Geologico d'Italia, [Online] Available at: www.apat.gov.it/site/_files/Inqua/2009_abruzzo_earthquake_report.pdf (accessed: September 12, 2009).

- Boncio, P., Lavecchia, G. and B. Pace, 2004. Defining a model of 3D seismogenic sources for seismic hazard assessment applications: the case of central Apennines (Italy). *Journal of Seismology*, 8(3), pp. 407-425.
- Brown, L. G., 1992. A survey of image registration techniques. *ACM computing surveys (CSUR)*, 24(4), pp. 325-376.
- Bryant, N., Zobrist, A. and T. Logan, 2003. Automatic co-registration of space-based sensors for precision change detection and analysis. In Proceedings of IEEE International Geoscience and Remote Sensing Symposium, IGARSS '03.
- Buckley, S., 2000. *ROI_PAC Documentation: Repeat Orbit Interferometry Package*. Abridged version of Chapter 3 of the PhD thesis, [Online] Available at: http://www.geo.cornell.edu/eas/PeoplePlaces/Faculty/matt/ROI_PAC_doc.pdf (accessed: September 26, 2009).
- Burgmann, R. Rosen, P. A. and Fielding, E. J., 2000. Synthetic aperture radar interferometry to measure earth's surface topography and its deformation. *Annual Review of Earth and Planetary Sciences*, 28(1), pp. 169-209.
- Cavinato, G. P. and Celles, P. G., 1999. Extensional basins in the tectonically bimodal central Apennines fold-thrust belt, Italy: response to corner flow above a subducting slab in retrograde motion. *Geology*, 27(10), pp. 955-958.
- Chen, D. and Brutsaert, W., 1998. Satellite-sensed distribution and spatial patterns of vegetation parameters over a Tallgrass Prairie. *Journal of the Atmospheric Sciences*, 55(2), pp. 1225-1238.
- Chen, C. W. and Zebker, H. A., 2002. Phase unwrapping for large SAR interferograms: statistical segmentation and generalized network models. *IEEE Transactions on Geoscience and Remote Sensing*, 40(8), pp. 1709-1719.
- COSI-Corr, 2004. *COSI-Corr: Measuring ground deformation from optical satellite and aerial images*. Tectonics Observatory, California Institute of Technology, [Online] Available at: http://www.tectonics.caltech.edu/slip_history/spot_coseis/index.html (accessed: September 16, 2009).
- COSMO-SkyMed, 2009. *About COSMO-SkyMed*. COSMO-SkyMed Web Site/CUGS, [Online] Available at: <http://www.cosmo-skymed.it/en/index.htm> (accessed: December 28, 2009).
- Crippen, R. E. and Blom, R. G., 1991. Measurement of sub-resolution terrain displacements using SPOT panchromatic imagery. In Proceedings of International Geoscience and Remote Sensing Symposium, 1991. IGARSS '91 (Remote Sensing: Global Monitoring for Earth Management).
- D'Addezio, G., Cinti, F. R. and D. Pantosti, 1995. A large unknown historical earthquake in the Abruzzi region (central Italy): combination of geological and historical data. In *Annali di Geofisica*.
- DBMI04, 2009. *Database Macrosismico Italiano 2004*. INGV, [Online] Available at: <http://emidius.mi.ingv.it/DBMI04/> (accessed: August 27, 2009).
- Delacourt, C., Allemand, P., Casson, B. and H. Vadon, 2004. Velocity field of the "La Clapière" landslide measured by the correlation of aerial and Quick Bird satellite images. *Geophysical Research Letter*, 31(15), pp. L15619.
- Devoti R., Riguzzi F., Cuffaro M. and C. Doglioni, 2008. New GPS constraints on the kinematics of the Apennines subduction. *Earth and Planetary Science Letters*, 273(1-2), pp. 163-174.
- Doglioni, C., 1990. The global tectonic pattern. *Journal of Geodynamics*, 12(1), pp. 21-38.
- Doglioni, C., 1991. A proposal for the kinematic modelling of W-dipping subductions: possible applications to the Tyrrhenian-Apennines system. *Terra Nova*, 3(4), pp. 423-434.
- Dominguez, S., Avouac, J. P. and Michel, R., 2006. Horizontal coseismic deformation of the

- 1999 Chi-Chi earthquake measured from SPOT satellite images: implications for the seismic cycle along the western foot-hills of central Taiwan. *Journal of Geophysical Research*, 108(B2), pp. 2083.
- Dowding, S. Kuuskivi, T. and Li, X., 2004. Void fill of SRTM elevation data: principles, processes and performance. *ASPRS Images to Decision: Remote Sensing Foundation for GIS Applications*, 12(), pp. 16.
- Du, Y., Aydin, A. and Segall, P., 1992. Comparison of various inversion techniques as applied to the determination of a geophysical deformation model for the 1983 Borah Peak earthquake. *Bulletin of the Seismological Society of America*, 82(4), pp. 1840.
- Duchossois, G. and Martin, P., 1995. ERS-1 and ERS-2 tandem operations. *ESA Bulletin*, 83(), pp. .
- EMERGEO Team, 2009. *Rilievi geologici di terreno effettuati nell'area epicentrale della sequenza sismica dell'Aquilano del 6 aprile 2009*. EMERGEO Working Group, [Online] Available at: <http://portale.ingv.it/real-time-monitoring/emergeo/> (accessed: August 25, 2009).
- EMSC, 2009. *Search for earthquakes*. European-Mediterranean Seismological Centre products, [Online] Available at: <http://www.emsc-csem.org/index.php?page=current&sub=filter> (accessed: June 18, 2009).
- ENVISAT Auxiliary Data, 2009. *Auxiliary Data*. ESA Earthnet Online, [Online] Available at: <http://envisat.esa.int/category/index.cfm?fcategoryid=38> (accessed: September 2, 2009).
- ENVISAT, 2009. *ENVISAT*. ESA Earthnet online, [Online] Available at: <http://envisat.esa.int/> (accessed: August 29, 2009).
- ERS, 2009. *ERS*. ESA Earthnet online, [Online] Available at: <http://earth.esa.int/ers/> (accessed: August 28, 2009).
- Farr, T. G., Rosen, P. A., Caro, E., Crippen, R., Duren, R., Hensley, S., Kobrick, M., Paller, M., Rodriguez, E., Roth, L. and others, 2007. The shuttle radar topography mission. *Reviews of Geophysics*, 45(2), pp. RG2004.
- Ferretti, A., Prati, C. and Rocca, F., 2000. Measuring subsidence with SAR interferometry applications of the permanent scatterers technique. In *Proceedings of workshop on Advanced Techniques for the Assessment of Natural Hazards in Mountain Areas*, Innsbruck, Austria.
- Ferretti, A., Monti-Guarnieri, A., Prati, C., Rocca, F. and Massonnet, D., 2007. *InSAR Principles: Guidelines for SAR interferometry processing and interpretation*. 1st Ed., The Netherlands: ESA Publications.
- Fialko, Y., Simons, M. and Agnew, D., 2001. The complete 3D surface displacement field in the epicentral area of the 1999 Mw 7.1 Hector Mine earthquake, California, from space geodetic observations. *Geophysical Research Letters*, 28(16), pp. 3063-3066.
- Fielding, E., 2008a. *ROI_PAC Internals: under the hood*. Jet Propulsion Laboratory, California Institute of Technology, [Online] Available at: <http://cws.unavco.org:8080/cws/learn/uscs/2009/2009insar/Fielding-InSARpresentation-2009.pdf> (accessed: September 26, 2009).
- Fielding, E., 2008b. *ALOS PALSAR ROI_PAC Wiki*, [Online] Available at: http://www.roipac.org/ALOS_PALSAR (accessed: November 29, 2009).
- Franceschetti, G. and Lanari, R., 1999. *Synthetic Aperture Radar Processing*. 1st Ed., Boca Raton, Florida, USA: CRC Press.
- Funning, G. J., Parsons, B., Wright, T. J., Jackson, J. A., and E. J. Fielding, 2005. Surface displacements and source parameters of the 2003 Bam (Iran) earthquake from ENVISAT advanced synthetic aperture radar imagery. *Journal of Geophysical Research*, 110(), pp. B09406.
- Galadini, F. and Galli, P., 2000. Active tectonics in the central Apennines (Italy): input data for seismic hazard assessment. *Natural Hazards*, 22(3), pp. 225-268.

- Galadini, F. and Messina, P., 2001. Plio-Quaternary changes of the normal fault architecture in the central Apennines (Italy). *Geodinamica Acta*, 14(6), pp. 321-344.
- GEER, 2009. *Preliminary report on the seismological and geotechnical aspects of the April 6, 2009, L'Aquila Earthquake in central Italy*. Geo-engineering Extreme Events Reconnaissance (GEER), [Online] Available at: http://www.geerassociation.org/GEER_Post%20EQ%20Reports/Italy_2009/Cover_Italy2009.html (accessed: August 25, 2009).
- Ghisetti, F. and Vezzani, L., 2000. Normal faulting, transcrustal permeability and seismogenesis in the Apennines (Italy). *Tectonophysics*, 348(1-3), pp. 155-168.
- Giuliani, R., Anzidei, M., Bonci, L., Calcaterra, S., D'Agostino, N., Mattone, M., Pietrantonio, G., Riguzzi, F. and G. Selvaggi, 2007. Coseismic displacements associated to the Molise (Southern Italy) earthquake sequence of October-November 2002 inferred from GPS measurements. *Tectonophysics*, 432(1-4), pp. 21-35.
- Goldhirsh, J. and Rowland, J. R., 1982. A tutorial assessment of atmospheric height uncertainties for high-precision satellite altimeter missions to monitor ocean currents. *IEEE Transactions on Geoscience and Remote Sensing*, GE-20(4), pp. 418-434.
- Goldstein, R. M. and Werner, C. L., 1998. Radar interferogram filtering for geophysical applications. *Geophysical Research Letters*, 25(21), pp. 4035-4038.
- Goldstein, R. M. and H. A. Zebker, 1987. Interferometric radar measurement of ocean surface currents. *Nature*, 328(), pp. 707-709.
- Goldstein, R. M., Zebker, H. A. and Werner, C. L., 1988. Satellite radar interferometry: two-dimensional phase unwrapping. *Radio Science*, 23(4), pp. 713-720.
- Goldstein, R. M., Engelhardt, H., Kamb, B. and Frolich, R. M., 1993. Satellite radar interferometry for monitoring ice sheet motion: Application to an Antarctic ice stream. *Science*, 262(5139), pp. 1525-1530.
- Graham, L. C., 1974. Synthetic interferometer radar for topographic mapping. *Proceedings of the IEEE*, 62(6), pp. 763-768.
- Gray, A. L., Mattar, K. E., Vachon, P. W., Bindschadler, R., Jezek, K. C., Forster, R. and Crawford, J. P., 1998. InSAR results from the RADARSAT Antarctic mapping mission data: estimation of glacier motion using a simple registration procedure. In Proceedings of IEEE International Geoscience and Remote Sensing Symposium, IGARSS '98.
- Griffiths, H., 1995. Interferometric synthetic aperture radar. *Electronics & Communications Engineering Journal*, 7(6), pp. 247-256.
- Gruppo di lavoro CPTI, 2004. *Catalogo Parametrico dei Terremoti Italiani, versione 2004 (CPTI04)*. INGV, Bologna, [Online] Available at: <http://emidius.mi.ingv.it/CPTI04/> (accessed: June 30, 2009).
- Hall, O., Falorni, G. and Bras, R. L., 2005. Characterization and quantification of data voids in the Shuttle Radar Topography Mission data. *IEEE Geoscience and Remote Sensing Letters*, 2(2), pp. 177-181.
- Hao, B., Ma, C., Zhang, G. and Kang, L., 2008. Analyzing decorrelation of multi-temporal SAR data on InSAR. In Congress on Image and Signal Processing, CISP'08.
- Hooper, A., Zebker, H., Segall, P. and Kampes, B., 2004. A new method for measuring deformation on volcanoes and other natural terrains using InSAR persistent scatterers. *Geophysical Research Letter*, 31(23), pp. L23611.
- Italy Earthquake, 2009. *Italy Earthquake, April 2009*. ESA, Earth Observation, Earth Watching, [Online] Available at: http://earth.esa.int/ew/earthquakes/Italy_April09/Italy_April09.htm (accessed: September 1, 2009).
- Jonsson, S., Zebker, H., Segall, P. and Amelung, F., 2002. Fault slip distribution of the 1999 Mw 7.1 Hector Mine, California, earthquake, estimated from satellite radar and GPS measurements. *Bulletin of the Seismological Society of America*, 92(4), pp. 1377-1389.

- Julea, A., Vasile, G., Petillot, I., Trouvé, E., Nicolas, J. M., Gay, M. and Bolon, P., 2006. Simulation of SAR images and radar coding of georeferenced information for temperate glacier monitoring. In Proceedings of Optimization of Electrical and Electronic Equipments, OPTIM'06, Brasov, Romania.
- L'Aquila, 2009a. *L'Aquila*. Britannica online Encyclopedia, [Online] Available at: <http://www.britannica.com/EBchecked/topic/330435/LAquila> (accessed: June 21, 2009).
- L'Aquila, 2009b. *L'Aquila*. Wikipedia, The Free Encyclopedia, [Online] Available at: <http://en.wikipedia.org/w/index.php?title=L%27Aquila&oldid=297391687> (accessed: June 19, 2009).
- LANDSAT DFCB, 2009. *LANDSAT 7 ETM+ Level 1 Data Format Control Book*. USGS, [Online] Available at: http://landsat.usgs.gov/documents/LS_DFCB_04.pdf (accessed: September 26, 2009).
- Larson, K. M., P. Bodin and J. Gomborg, 2003. Using 1-Hz GPS data to measure deformations caused by the Denali fault earthquake. *American Association for the Advancement of Science*, 300(5624), pp. 1421-1424.
- Lee, J. -S., 1980. Digital Image enhancement and noise filtering by use of local statistics. *IEEE Transactions on Pattern Analysis and Machine Intelligence*, PAMI-2(2), pp. 165-168.
- Leprince, S., S. Barbot, F. Ayoub and J. P. Avouac, 2007a. Automatic and precise orthorectification, coregistration and sub-pixel correlation of satellite images, application to ground deformation measurements. *IEEE Transactions on Geoscience and Remote Sensing*, 45(6), pp. 1529-1557.
- Leprince, S., F. Ayoub, Y. Klinger and J. P. Avouac, 2007b. Co-registration of Optically Sensed Images and Correlation (COSI-Corr): an operational methodology for ground deformation measurements. *IEEE International Geoscience and Remote Sensing Symposium (IGARSS 2007)*, 45(6), pp. 1943-1946.
- Leprince, S., 2008. *Interpreting correlation results*. The COSI-Corr project discussion group, [Online] Available at: <http://www.tectonics.caltech.edu/forum/viewtopic.php?id=60> (accessed: December 3, 2009).
- Li, Z. and Kafatos, M., 2000. Interannual variability of vegetation in the United States and its relation to El Nino/Southern Oscillation. *Remote Sensing of Environment*, 71(3), pp. 239-247.
- Lopes, A., Touzi, R. and Nezry, E., 1990. Adaptive speckle filters and scene heterogeneity. *IEEE Transactions on Geoscience and Remote Sensing*, 28(6), pp. 992-1000.
- Lopez-Martinez, C. and Pottier, E., 2005. Topography independent InSAR coherence estimation in a multi-resolution scheme. In Proceedings of IEEE International Geoscience and Remote Sensing Symposium, IGARSS '05.
- Madsen, S. N. and Zebker, H. A., 1998. *Imaging radar interferometry, chapter 6 in Henderson, F. M. and A. J. Lewis, Principles and applications of imaging radar, Manual of Remote Sensing, vol. 2*. 3rd Ed., New York, USA: John Wiley & Sons.
- Massonnet, D. and Feigl, K. L., 1998. Radar interferometry and its application to changes in the Earth's surface. *Reviews of Geophysics*, 36(4), pp. 441-500.
- Massonnet, D., Rossi, M., Carmona, C., Adragna, F., Peltzer, G., Feigl, K. and T. Rabaute, 1993. The displacement field of the Landers earthquake mapped by radar interferometry. *Nature*, 364(), pp. 138 - 142.
- Mediaset, 2009. *Terremoto, 294 i morti accertati*. RTI S.p.A. Interactive Media, [Online] Available at: <http://www.tgcom.mediaset.it/cronaca/articoli/articolo446725.shtml> (accessed: June 18, 2009).
- Meng, D., Ambikairajah, E. and Ge, L., 2006. A new filtering technique for interferometric phase images. In Proceedings of the third International Symposium on Future Intelligent Earth Observation Satellites.

- Michel, R., Avouac, J. and J. Taboury, 1999. Measuring ground displacements from SAR amplitude images: application to the Landers earthquake. *Geophysical Research Letters*, 26(7), pp. 875-878.
- Miranda, N., Rosich, B., Santella, C. and Grion, M., 2004. Review of the impact of ERS-2 piloting modes on the SAR Doppler stability. In Proceedings of FRINGE 2003 Workshop, Frascati, Italy.
- Moroni, M. and Cenedese, A., 2005. Comparison among feature tracking and more consolidated velocimetry image analysis techniques in a fully developed turbulent channel flow. *Measurement Science and Technology*, 16(11), pp. 2307-2322.
- Nishimura, T., Imakiire, T., Yarai, H., Ozawa, T., Murakami, M. and Kaidzu, M., 2003. A preliminary fault model of the 2003 July 26, M6.4 northern Miyagi earthquake, north-eastern Japan, estimated from joint inversion of GPS, levelling, and InSAR data. *Earth, Planets and Space*, 55(12), pp. 751-757.
- Nunnari, G., Puglisi, G. and Guglielmino, F., 2005. Inversion of SAR data in active volcanic areas by optimization techniques. *Nonlinear Processes in Geophysics*, 12(6), pp. 863-870.
- Okada, Y., 1985. Surface deformation due to shear and tensile faults in a half-space. *Bulletin of the Seismological Society of America*, 75(4), pp. 1135-1154.
- Pathier, E., B. Fruneau, B. Deffontaines, J. Angelier, Ch.-P. Chang, Sh.-B. Yu and Ch.-T. Lee, 2003. Coseismic displacements of the foot-wall of the Chelungpu fault caused by the 1999, Taiwan, Chi-Chi earthquake from InSAR and GPS data. *Earth and Planetary Science Letters*, 212(1-2), pp. 73-88.
- Pedersen, R., Jonsson, S., Arnadóttir, T., Sigmundsson, F. and Feigl, K. L., 2003. Fault slip distribution of two June 2000 Mw 6.5 earthquakes in South Iceland estimated from joint inversion of InSAR and GPS measurements. *Earth and Planetary Science Letters*, 213(3-4), pp. 487-502.
- Peyret, M., J. Chéry, Y. Djamour, A. Avallone, F. Sarti, P. Briole and M. Sarpoulaki, 2007. The source motion of 2003 Bam (Iran) earthquake constrained by satellite and ground-based geodetic data. *Geophysical Journal International*, 169(3), pp. 849-865.
- Peyret, M., Y. Djamour, M. Rizza, J.-F. Ritz, J.-E. Hurtrez, M. A. Goudarzi, H. Nankali, J. Chéry, K. Le Dortz and F. Uri, 2008a. Monitoring of the large slow Kahrod landslide in Alborz mountain range (Iran) by GPS and SAR interferometry. *Engineering Geology*, 100(3-4), pp. 131-141.
- Peyret, M., F. Rolandone, S. Dominguez, Y. Djamour and B. Meyer, 2008b. Source model for the Mw 6.1, 31 March 2006, Chalan-Chulan Earthquake (Iran) from InSAR. *Terra Nova*, 20(2), pp. 126-133.
- Peyret, M., 2009. email, December 15 <peyret@gm.univ-montp2.fr> .
- Peyret, M., 2009. email, December 17 <peyret@gm.univ-montp2.fr> .
- Peyret, M., 2009. email, September 7 <peyret@gm.univ-montp2.fr> .
- Peyret, M., 2009. email, September 8 <peyret@gm.univ-montp2.fr> .
- Pritchard, M. E. and Simons, M., 2004. An InSAR-based survey of volcanic deformation in the southern Andes. *Geophysical Research Letters*, 31(35), pp. L15610.
- Pritchard, M., 2009. *Offset Tracking*. ROI_PAC Wiki, [Online] Available at: http://www.roipac.org/Offset_Tracking (accessed: November 13, 2009).
- QUEST, 2009. *Report on the effects of the Aquilano earthquake of 6 April 2009*. INGV MI-QUEST, [Online] Available at: http://www.mi.ingv.it/eq/090406/quest_eng.html (accessed: August 27, 2009).
- Quincey, D. J., Richardson, S. D., Luckman, A., Lucas, R. M., Reynolds, J. M., Hambrey, M. J. and N. F. Glasser, 2007. Early recognition of glacial lake hazards in the Himalaya using remote sensing data sets. *Global and Planetary Change*, 56(1-2), pp. 137-152.

- R, 2009.*R: A Language and Environment for Statistical Computing*. R development core team: R Foundation for statistical computing, [Online] Available at: <http://www.r-project.org> (accessed: November 10, 2009).
- RADARSAT-2, 2008.*About RADARSAT-2: features and benefits*. MacDonald, Dettwiler and Associates Ltd., [Online] Available at: http://www.radarsat2.info/about/features_benefits.asp (accessed: December 24, 2009).
- Rees, W. G., 2000. Technical note: Simple masks for shadowing and highlighting in SAR images. *International Journal of Remote Sensing*, 21(11), pp. 2145-2152.
- Reigber, C., Xia, Y., Kaufmann, H., Massmann, F. H., Timmen, L., Bodechtel, J. and Frei, M., 1997. Impact of precise orbits on SAR interferometry. In Proceedings of the 'Fringe 96' workshop on ERS SAR interferometry.
- Reigber, A., Erten, E., Guillaso, S., Hellwich, O., 2007. IDIOT: A free and easy-to-use software tool for DInSAR analysis. In Proceedings of ENVISAT Symposium, Montreux, Switzerland, 23-27 April 2007.
- Reuter, H. I., Nelson, A. and Jarvis, A., 2007. An evaluation of void filling interpolation methods for SRTM data. *International Journal of Geographic Information Science*, 21(9), pp. 983-1008.
- Rosen, P. A., Hensley, S., Zebker, H. A., Webb, F. H. and Fielding, E. J., 1996. Surface deformation and coherence measurement of Kilauea Volcano, Hawaii, from SIR-C radar interferometry. *Journal of geophysical research*, 101(E10), pp. 23109-23152.
- Rosen, P. A., Hensley, S., Joughin, I. R., Li, F. K., Madsen, S. N., Rodriguez, E., Goldstein, R. M., 2000. Synthetic aperture radar interferometry. *Proceedings of the IEEE*, 88(3), pp. 333-382.
- Rosen, P. A., Hensley, S., Peltzer, G. and Simons, M., 2004. Updated repeat orbit interferometry package released. *EOS Transactions- American Geophysical Union*, 85(5), pp. 47.
- Rosich, B., D. Esteban, G. Emiliani, P. Meadows, B. Schattler and R. Viggiano, 2000. ERS-2 Mono-Gyro piloting: impact on ERS-2 SAR data quality and applications performance. *ERS-2 mono-gyro piloting*, 1(1), pp. .
- Rovida, A., Castelli, V., Camassi, R. and Stucchi, M., 2009. *Terremoti storici nell'area colpita dagli eventi sismici dell'aprile 2009*. INGV Report, [Online] Available at: <http://www.mi.ingv.it/eq/090406/storia.html> (accessed: August 28, 2009).
- Salvi, S., 2009. *Measurement and modelling of coseismic deformation during the L'Aquila earthquake, Preliminary results*. INGV, [Online] Available at: http://portale.ingv.it/primo-piano-1/news-archive/2009-news/april-6-earthquake/sar-preliminary-results/view?set_language=en (accessed: December 9, 2009).
- Sambridge, M., 1999a. Geophysical inversion with a neighbourhood algorithm-I. Searching a parameter space. *Geophysical Journal International*, 138(2), pp. 479-494.
- Sambridge, M., 1999b. Geophysical inversion with a neighbourhood algorithm-II. Appraising the ensemble. *Geophysical Journal International*, 138(3), pp. 727-746.
- Samsonov, S. and Tiampo, K., 2006. Analytical optimization of a DInSAR and GPS data set for derivation of three-dimensional surface motion. *IEEE Geoscience and Remote Sensing Letters*, 3(1), pp. 107-111.
- Sandwell, D. and Wei, M., 2006. *ALOS Interferometry*. Satellite Geodesy at the Scripps Institution of Oceanography, University of California San Diego, [Online] Available at: <http://topex.ucsd.edu/alos/> (accessed: September 2, 2009).
- Sarti, F., Briole, P. and Pirri, M., 2006. Coseismic fault rupture detection and slip measurement by ASAR precise correlation using coherence maximization: application to a north-south blind fault in the vicinity of Bam (Iran). *IEEE Geoscience and Remote Sensing Letters*, 3(2), pp. 187-191.

- Scambos, T. A., Dutkiewicz, M. J., Wilson, J. C. and Bindschadler, R. A., 1992. Application of image cross-correlation to the measurement of glacier velocity using satellite image data. *Remote Sensing of Environment*, 42(3), pp. 177-186.
- Schaum, A. and McHugh, M., 1991. Analytic methods of image registration: displacement estimation and resampling. *Storming Media*, (), pp. .
- Segall, P. and Davis, J. L., 1997. GPS applications for geodynamics and earthquake studies. *Annual Review of Earth and Planetary Sciences*, 25(1), pp. 301-336.
- Smith, L. C., 2002. Emerging applications of Interferometric Synthetic Aperture Radar (InSAR) in geomorphology and hydrology. *Annals of the Association of American Geographers*, 92(3), pp. 385-398.
- SNAPHU Online Help, 2003. *Snaphu*. Snaphu Official Website, [Online] Available at: http://www-star.stanford.edu/sar_group/snaphu/snaphu_man1.html (accessed: September 3, 2009).
- SRTM, 2009. *Shuttle Radar Topography Mission*. Jet Propulsion Laboratory, California Institute of Technology, [Online] Available at: <http://www2.jpl.nasa.gov/srtm/> (accessed: November 22, 2009).
- Strang, G. and Nguyen, T., 1997. *Wavelets and filter banks*. Revised Ed., Massachusetts, USA: Wellesley Cambridge Press.
- Strozzi, T., Wegmuller, U., Tosi, L., Bitelli, G. and Spreckels, V., 2001. Land subsidence monitoring with differential SAR interferometry. *Photogrammetric engineering and remote sensing*, 67(11), pp. 1261-1270.
- Tarantola, A., 2005. *Inverse Problem Theory and Methods for Model Parameter Estimation*. 1st Ed., Philadelphia, USA: Society of Industrial and Applied Mathematics (SIAM).
- Townshend, J. R. G., Justice, C. O., Gurney, C. and J. McManus, 1992. The impact of misregistration on change detection. *IEEE Transactions on Geoscience and Remote Sensing*, 30(5), pp. 1054-1060.
- USGS, 2009a. *Earthquake Hazards Program*. U.S. Geological Survey, [Online] Available at: <http://earthquake.usgs.gov/eqcenter/eqinthenews/2009/us2009fcaf/> (accessed: June 18, 2009).
- USGS, 2009b. *Shuttle Radar Topography Mission (SRTM)-Finished*. USGS, [Online] Available at: <http://eros.usgs.gov/products/elevation/srtmbil.php> (accessed: September 1, 2009).
- Valensise, G., 2009. Alcune considerazioni sulla sismotettonica del terremoto del 6 aprile. *INGV Report*.
- van Dam, T. M. and Wahr, J. M., 1987. Displacements of the earth's surface due to atmospheric loading: effects of gravity and baseline measurements. *Journal of Geophysical Research*, 92(B2), pp. 1281-1286.
- van Puymbroeck, N., Michel, R., Binet, R., Avouac, J. P. and Taboury, J., 2000. Measuring earthquakes from optical satellite images. *Applied Optics*, 39(20), pp. 3486-3494.
- Walters, R. J., J. R. Elliott, N. D'Agostino, P. C. England, I. Hunstad, J. A. Jackson, B. Parsons, R. J. Phillips and G. Roberts, 2009. The 2009 L'Aquila earthquake (central Italy): a source mechanism and implications for seismic hazard. *Geophysical Research Letters*, 36(17), pp. L17312.
- Wikipedia, 2009. *Inverse problem*. Wikipedia, the free encyclopedia, [Online] Available at: http://en.wikipedia.org/wiki/Inverse_problem (accessed: October 19, 2009).
- Wright, T., E. Fielding and B. Parsons, 2001. Triggered slip: observations of the 17 August 1999 Izmit (Turkey) earthquake using radar interferometry. *Geophysical Research Letters*, 28(6), pp. 1079-1082.
- Yu, Q., Fu, S., Mayer, H., Liu, X., Yang, X. and Lei, Z., 2006. Generation of speckle-reduced phase images from three complex parts for synthetic aperture radar interferometry. *Applied*

- Physics Letters*, 88(11), pp. 114106.
- Zebker H. A. and Goldstein, R. M., 1986. Topography mapping from interferometric SAR observations. *Journal of Geophysics Research*, 91(B5), pp. 4993-4999.
- Zebker, H., Rosen, P. A., Goldstein, R. M., Gabriel, A. and Werner, C. L., 1994. On the derivation of coseismic displacement fields using differential radar interferometry: the Landers earthquake. *Journal of Geophysical Research*, 99(B10), pp. 19617-19634.
- Zebker, H. A. and Villasenor, J., 1992. Decorrelation in interferometric radar echoes. *IEEE Transactions on Geoscience and Remote Sensing*, 30(5), pp. 950-959.
- Zhong, L., Wicks, C., Power, J., Dzurisin, D., Thatcher, W. and Masterlark, T., 2002. Interferometric synthetic aperture radar studies of Alaska volcanoes. In Proceedings of IEEE International Geoscience and Remote Sensing Symposium, IGARSS '02.

